Scanning Multi-Gate and Scanning Quantum Dot Microscopy

Inauguraldissertation
zur
Erlangung der Würde eines Doktors der Philosophie
vorgelegt der
Philosophisch-Naturwissenschaftlichen Fakultät
der Universität Basel

von

Luca Forrer

2026

Genehmigt von der Philosophisch-Naturwissenschaftlichen Fakultät
auf Antrag von

Erstbetreuer: Prof. Dr. Martino Poggio
Zweitbetreuer: Prof. Dr. Dominik Zumbühl
Externer Experte: Prof. Dr. Peter H. Grutter

Basel, den 18. November 2025

Prof. Dr. Heiko Schuldt
Dekan

Abstract

A cryogenic scanning probe platform is developed that combines the spatial versatility of non-contact atomic force microscopy (AFM) with quantum dot (QD) charge sensitivity. Two complementary tip architectures are realized: a multi-gate lever with five independently addressable electrodes patterned on the tip plateau and a nanowire QD (NWQD) lever, in which an InAs/InP QD is integrated at the cantilever apex. To the best of our knowledge, this is the first implementation of a NWQD on a non-contact AFM lever. The work is enabled by two advances: a floating-PMMA transfer process for placement of nanostructures on cantilever tips, and a dedicated probe design optimized for fragile samples, featuring shielded piezo lines and a robust grounding scheme to suppress voltage spikes.

Proof-of-concept experiments at 4.2 K establish the distinct capabilities of both sensors. With the multi-gate lever, constant-z transport maps on InAs nanowires (NWs) exhibit gate-defined conductance modulations. Positioned above an InAs/InP QD, a tip gate functions as a mobile plunger and yields concentric equipotential rings, position-dependent lever arms, and full Coulomb diamonds. With the NWQD lever, Coulomb oscillations and diamonds verify device functionality. The extracted intrinsic white-noise limit is $\sim 10^{-5}\,\mathrm{e}/\sqrt{\mathrm{Hz}}$, whereas DC readout is 1/f-limited to $\sim 10^{-3}\,\mathrm{e}/\sqrt{\mathrm{Hz}}$. A reversed-plunger geometry quantifies gate-referred sensitivity as a function of tip-sample spacing, and constant-z scans converted using a calibrated Coulomb line shape yield electrostatic maps in qualitative agreement with simulations.

These results establish a practical foundation for scanning-based local gating (multi-gate lever) and tip-based charge sensing (NWQD lever) within commercial AFM hardware.

Table of Contents

Acronyms

Symbols

2DEG Two-Dimensional Electron Gas.

A

ACE Acetone.
ADC Analog-to-Digital Converter.
AFM Atomic Force Microscopy.
ALD Atomic Layer Deposition.
Amp Amplifier.
Ar Argon.
ASD Amplitude Spectral Density.
ATEC Advanced Tip at the End of the Cantilever.

B

BNC Bayonet Neill-Concelman.

C

CF ConFlat.
CNT Carbon Nanotube.
CVD Chemical Vapor Deposition.

D

D/C Directional Coupler.
DAC Digital-to-Analog Converter.
DI Deionized.
DMM Digital Multimeter.

E

EBL Electron-Beam Lithography.

F

FET Field Effect Transistor.
FG Forming Gas.
FIB Focused Ion Beam.
FPGA Field Programmable Gate Array.
FWHM Full Width at Half Maximum.

I

I/V converter Current-to-Voltage converter.
IBE Ion Beam Etching.
IF Intermediate Frequency.
IPA Isopropanol.

K

KPFM Kelvin Probe Force Microscopy.

L

LN_2 Liquid Nitrogen.
LHe Liquid Helium.

N

NC Non-Contact.
NV Nitrogen-Vacancy.
NW Nanowire.
NWQD Nanowire Quantum Dot.

P

PCB Printed Circuit Board.

PID Proportional-Integral-Derivative.
PLC Power Line Cycle.
PLL Phase-Locked Loop.
PMMA Polymethylmethacrylate.
PSD Power Spectral Density.
PVD Physical Vapor Deposition.

Q

QD Quantum Dot.
QPC Quantum Point Contact.

R

RF Radio Frequency.
RIE Reactive-Ion Etching.
RMSE Root-Mean-Square Error.
ROI Region Of Interest.
RT Room Temperature.

S

SCM Scanning Capacitance Microscopy.
SEM Scanning Electron Microscopy.
SET Single-Electron Transistor.
SGM Scanning Gate Microscopy.
SNR Signal-to-Noise Ratio.
STM Scanning Tunneling Microscopy.

T

TMA Trimethylaluminum.

List of Figures

List of Tables

Chapter 1

Introduction

Many of the most significant insights have come from improvements in imaging. From the first optical microscopes to modern electron and scanning probe microscopes, each advance in imaging technology has opened new research directions and revealed new physics. Among these techniques, the atomic force microscope (AFM), introduced in 1986 as an extension of the scanning tunneling microscope [1], has provided an extraordinarily versatile tool to investigate surfaces and nanoscale interactions with high sensitivity and resolution [2, 3]. In AFM, the interaction between a sharp tip and the sample surface is transduced into measurable deflections or changes in the cantilever's dynamics. The tip is raster-scanned across the sample to create high-resolution images. Since its invention, AFM has become a platform adaptable to an impressive range of modalities. Tip functionalization has extended AFM to probe mechanical, electrical, magnetic, and chemical properties, establishing it as one of the most flexible and widely applied tools in nanoscale science. [2, 3]

In parallel with the development of scanning probe methods, the field of quantum science has emerged as a central theme in condensed matter physics. A major long-term motivation has been the realization of scalable quantum computation. [4, 5] This effort has driven the exploration of new quantum materials and devices, as well as the development of techniques capable of detecting and manipulating quantum states with high precision. Among the most successful concepts that have emerged are semiconductor quantum dots (QDs). These nanoscale structures confine electrons or holes in all three spatial dimensions, resulting in discrete energy levels and sharp transport resonances. QDs have proven to be exceptionally sensitive charge sensors, capable of detecting fractions of the elementary charge at sub-micron distances. [6] Such sensors are routinely integrated on the same substrate as the system under study, e.g., in semiconductor spin-qubit architectures, where they provide the essential functionality of reading out quantum states. [7, 8]

The combination of scanning probe microscopy with QD-based sensing offers a powerful new route to investigate nanoscale electronic phenomena. By integrating a QD charge sensor onto a scanning probe cantilever, it becomes possible to hover above the surface and measure local electrostatic potentials or charge fluctuations with high spatial resolution. [9] This approach builds on concepts pioneered by scanning single-electron transistors (SETs), which have been successfully used to image local electronic density in systems such as graphene and oxide interfaces. [10, 11] More recently, QDs defined in carbon nanotubes (CNTs) have been employed in scanning probes, enabling the study of phenomena such as Wigner crystallization and hydrodynamic electron flow. [12–14] However, these approaches often rely on delicate in situ preparation of nanotubes, limiting their versatility and widespread adoption. In contrast, the use of semiconductor nanowires (NWs) as a platform

for hosting QDs provides a more flexible route, allowing for optimization of NW material, geometry, and placement. This preserves compatibility with a conventional AFM cantilever, thereby combining topographic imaging with ultrasensitive charge detection.

Nanowire quantum dots (NWQDs) possess several intrinsic advantages for scanning probe applications. Their one-dimensional geometry naturally provides strong confinement and requires only a few gate electrodes for electrostatic control. Their small dimensions allow them to be positioned close to a sample surface, where sensitivity to local fields is maximized.

The work presented in this thesis is devoted to the development and first demonstration of a scanning probe platform using a non-contact AFM lever combined with an NWQD sensor. The central aim is to integrate a QD onto the tip of an AFM cantilever and to realize a measurement setup capable of proof-of-principle experiments. Beyond this initial demonstration, an additional objective is to explore different device concepts by incorporating multiple gate electrodes directly onto the cantilever. Unlike single-gate probes previously reported, multi-gated cantilevers offer new functionalities. They enable tunable control over the local electrostatic environment of the QD sensor, allow active manipulation of the sample, and may even facilitate the induction of QDs within the sample itself by means of lever-based gating. This capability holds promise for experiments in which the sensor actively shapes the nanoscale electronic landscape.

This project seeks to merge the versatility of AFM with the exquisite charge sensitivity of NWQDs, aiming to establish a platform for local electronic imaging. By leveraging advances in NW growth and device integration, the scanning NWQD approach aspires to enable measurements with high spatial and temporal resolution. The results described here represent the first steps toward a versatile and robust technique for imaging the nanoscale electronic properties of quantum materials.

Chapter 2

Theoretical Background

This chapter provides the theoretical background relevant to the scanning probe platform and the experiments presented in this work. It is organized into the following sections:

- Section 2.1 introduces the basic concepts of quantum confinement, Coulomb blockade, and discrete charge states as the physical basis for single-electron charge detection.
- Section 2.2 explains how changes in the electrostatic environment modulate the conductance of a nearby charge sensor.
- Section 2.3 analyzes noise sources and discusses sensitivity limits of quantum dot sensors.
- Section 2.4 describes the principles of impedance matching and reflectometry for high-bandwidth charge readout.
- Section 2.5 covers the mechanical dynamics of cantilevers and their interaction with electrostatic forces.
- Section 2.6 reviews scanning probe techniques based on single-electron transistors and scanning gate microscopy.
- Section 2.7 compares quantum dot sensors to alternative platforms such as metallic single-electron transistors, quantum point contacts, field-effect transistors, and nitrogen-vacancy centers.

Together, these sections establish the theoretical framework for understanding the measurement methods, device operation, and data interpretation used throughout this thesis.

2.1 Quantum Dot Fundamentals

This section introduces the fundamental properties of QDs and SETs, including quantum confinement, charging energy, and Coulomb blockade, which are all key physical principles underlying the operation of QD charge sensors.

Semiconductor QDs are nanostructures that confine electrons in all three spatial dimensions, leading to discrete, atom-like energy levels. [15] Quantum confinement occurs when electrons are constrained to a domain comparable to their de Broglie wavelength. [16] This confinement can be achieved using combinations of suitable material properties and by applying electrostatic potentials. Depending on the size and shape of the nanostructure materials, the confinement of the electrons arising from the material properties is in zero, one, or two dimensions. [17] QDs can be realized within such structures in various ways, as described below. A 0D structure confines electrons in all three spatial directions (x, y, and z) as it is the case for self-assembled nanocrystals or epitaxially grown islands. [18] To realize such a structure as an experimentally accessible QD, it must be connected to the macroscopic world using source and drain contacts, while additional gate electrodes allow tuning of the electrostatic potential. In 1D structures, such as NWs, electrons are structurally strongly confined in the transverse directions, but only weakly confined along the longitudinal direction. A QD can be defined in such systems by inducing tunnel barriers. This is typically achieved either by locally fabricated gate electrodes, which, when voltage-biased, can deplete the electron density to create tunable barriers, or by Schottky tunnel barriers at the source and drain contacts. Another approach is to define tunnel barriers directly during NW growth by introducing segments of a material with a larger bandgap than the host NW, for example InP barriers in InAs NWs [19] or crystal-phase engineering using alternating crystal phase segments. [20] Such heterostructures create intrinsic tunnel barriers and enable the formation of QDs without the need for local tunnel barrier gates. Using the locally fabricated gates, however, provides the advantage that tunnel barrier height and QD potential can be tuned in situ. In the case of a 2D structure like a two-dimensional electron gas (2DEG), electrons are structurally confined in a plane. [21] Laterally, electrons can be confined using top-gate electrodes, making it a highly tunable platform. Whether additional electrostatic confinement is required depends on the structural confinement potential. [17]

Having introduced quantum confined structures, transport through QDs is now addressed. A QD becomes experimentally accessible when it is tunnel coupled to source and drain electrodes and its potential is tuned by a capacitively coupled gate. This three-terminal device configuration is known as an SET, enabling single-electron transport studies. [22] A schematic of an SET can be seen in Figure 2.1. This architecture is common to all the above-mentioned approaches.

Electrical transport through an SET exhibits two key properties. First, the strong electron-electron interactions on the dot lead to charging energy, the cost of changing the number of electrons by one. Second, the spatial confinement of charges resulting in discrete quantum energy levels. [23] These two effects combined lead to phenomena such as single-electron tunneling and Coulomb blockade, which are both central to QD devices. [17]

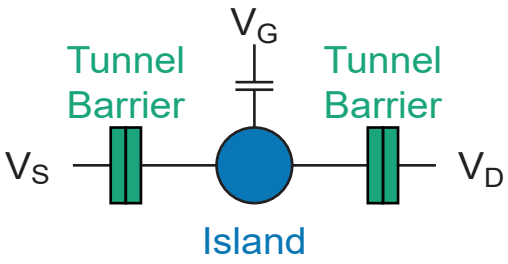

Figure 2.1: Schematic of a SET. The central island (blue) is tunnel-coupled to the source (S) and drain (D) via tunnel barriers (green). Voltages V_S and V_D are applied to the source and drain electrodes, respectively. The electrostatic potential of the island is controlled through a capacitively coupled gate electrode (G) held at voltage V_G.

To understand these effects, the energy cost associated with adding an electron to a QD is examined, by the concept of the charging energy, quantum level spacing, and electrochemical potential. This will help to understand the influence of gate voltages and source-drain bias on transport through the dot, leading to characteristic measurements of Coulomb peaks and Coulomb diamonds in stability diagrams. Consider a QD initially isolated from source and drain contacts, the dot then acts like an island for electrons with an integer number of electrons and therefore also a quantized number of charges. [22] When the dot is tunnel coupled to source and drain and a charge is added to the dot, Coulomb repulsion of individual electrons increases the electrostatic energy of the dot. [24] This charging energy (E_C) can be written as:

$$E_C = \frac{e^2}{2C_{dot}} \tag{2.1}$$

where C_{dot} is the total capacitance of the dot and e the elementary charge. The total capacitance of the dot is the sum of the capacitance to source (C_S), to drain (C_D), and to the gate electrodes (C_G).

$$C_{dot} = C_S + C_D + C_G \tag{2.2}$$

For the case that the thermal energy, given by k_BT (where k_B is the Boltzmann constant and T the temperature), is much smaller than E_C, conductance through

the dot is suppressed because the thermal fluctuations are too small to overcome the charging energy. [24] This is known as the Coulomb blockade of single-electron tunneling. In addition to the charging energy, strong spatial confinement results in discrete single particle energy levels rather than a continuum of states. The level spacing (ΔE) usually can be approximated by a particle in a box model, with m^* the effective electron mass, and L the size of the dot:

$$\Delta E \sim \frac{\hbar^2 \pi^2}{2m^* L^2} \tag{2.3}$$

From Equation 2.3 one can see that the smaller the dot, the larger the level spacing. [22] When adding a charge to the dot, not only must the charging energy be taken into account, but also the level spacing between the last occupied and the next available single particle state is important. Both of these two effects are included in the addition energy (E_{add}), which is the sum of the two energies:

$$E_{add} = \Delta E + E_C \tag{2.4}$$

If the next available level has an unoccupied spin state $\Delta E = 0$, then the addition energy equals E_C. [23]

At low temperatures, when only sequential tunneling processes are considered, transport occurs only when energy conservation is satisfied. [17] To describe transport through the QD, the electrochemical potential μ_N, which is the energy needed to add the N^{th} electron to the dot, is introduced. With $E(N)$ being the total energy of the dot with N electrons, one can write:

$$\mu_N = E(N) - E(N-1) \tag{2.5}$$

Electrons can only tunnel through the dot when the electrochemical potential μ_N lies within the bias window, meaning $\mu_S \geq \mu_N \geq \mu_D$ with μ_S and μ_D being the electrochemical potentials of source and drain (see Figure 2.2b). When there is no available level in the bias window, no current flows through the dot (Figure 2.2c). Then the QD is in the so-called Coulomb blockade. [17]

The dot's electrochemical potential can be shifted by applying a gate voltage (V_G), which tunes the energy levels relative to the reservoirs. In this context V_G is often referred to as plunger gate voltage. When the source-drain window is fixed and the gate voltage is swept, the device switches between Coulomb blockade and single-electron tunneling, resulting in periodic conductance peaks, known as Coulomb oscillations (Figure 2.2d). Mapping conductance as a function of gate voltage and source-drain bias results in so-called Coulomb diamonds (Figure 2.2e). [22]

Based on the Coulomb blockade and the single-electron tunneling effect, SETs can be used as highly sensitive charge detectors due to the strong influence of small

charge variations near the Coulomb island. [25–28] In the following section, a more detailed description of how an SET is used as an electrometer is given.

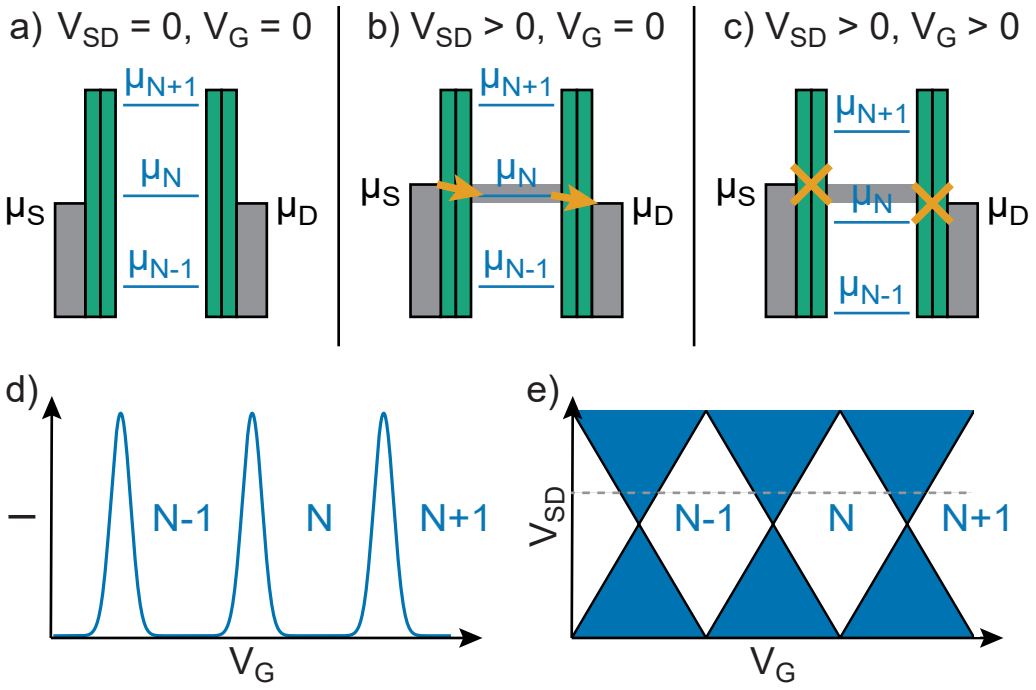

Figure 2.2: Schematic illustration of the alignment of the electrochemical potentials of the source (μ_S), drain (μ_D), and QD (μ_N). **a)** With no source-drain bias applied ($V_{SD} = 0$), μ_S and μ_D are at the same energy and no available dot state is aligned with them, transport is therefore not possible. **b)** Applying a finite source-drain voltage ($V_{SD} > 0$) creates a bias window, indicated by the gray region, between μ_S and μ_D. If a dot state lies within this window, electrons can tunnel from the source reservoir, through the first tunnel barrier (green), onto the dot, and subsequently through the second tunnel barrier to the drain. This results in a measurable conductance. **c)** If no dot state lies within the bias window, transport is suppressed and the dot is in the Coulomb blockade regime. The relative position of the dot levels with respect to μ_S can be tuned via a capacitively coupled gate, allowing transitions between blockade and conduction. **d)** Sweeping V_G at fixed V_{SD} shifts the dot levels in and out of the bias window, producing Coulomb oscillations in the conductance, as shown schematically. **e)** Sweeping V_{SD} against V_G yields the characteristic Coulomb diamond pattern, which can be viewed as a set of Coulomb oscillations at different bias values. The dashed line in e) marks the bias corresponding to the oscillations shown in d).

2.2 Charge-Sensing with a Quantum Dot

Following the introduction of SETs and QD fundamentals, this section shows the principle of charge sensing using a QD.

Due to the high sensitivity of QDs to their electrostatic environment, they are used as charge sensors in various experiments. [29–33] Small changes in the surrounding potential, such as movement or addition of single electrons, to a nearby system can change the conductance of the dot. This principle forms the basis for a highly sensitive electrometer, which is capable of detecting single-electron events in real time if positioned in close proximity to the sample. [27, 34, 35] In the following, the conventional use of on-chip QD charge sensors is discussed, followed by the concept of QDs integrated on mechanical cantilevers, providing a path toward scanning electrometers.

First, the functional mechanism of a QD configured as a charge sensor is addressed. As discussed in Section 2.1, when a QD is operated as an SET, the conductance shows sharp Coulomb peaks as a function of gate voltage (Figure 2.2d). Positioning the QD at the flank of such an oscillation maximizes its transconductance. In this regime, any external perturbation that shifts the QD's electrostatic potential will displace the Coulomb resonance in gate voltage, leading to a measurable change in the source-drain current. [27, 28] This operating principle allows for the detection of fractions of single charges in the vicinity of the QD. Implementing a dedicated QD charge sensor adjacent to the system under study has become an important technique for probing mesoscopic and quantum systems. Such sensors have been employed to study different systems such as single QDs [34, 35], double QDs [36], and spin qubits [37]. Capacitive coupling between the sensor and the sample ensures that changes in the local charge configuration induce a shift in the sensor's energy levels, which are detected as variations in its conductance. The use of such charge sensors shows single-electron sensitivity on sub-microsecond timescales, enabling high fidelity qubit readout and real time detection of electron tunneling. [37] Recent progress has pushed the limits of both speed and sensitivity in diverse device platforms. [38–40] All the above-mentioned charge sensors have in common that they are at a fixed position on the sample. To overcome that, charge sensors can be integrated onto the tips of mechanical cantilevers, creating a scanning probe, capable of detecting local charge variations. This combines the charge sensitivity of a QD with the spatial resolution and force sensitivity of scanning probe techniques. Before reviewing previous studies on scanning SETs in Section 2.6, first a look is taken at the performance factors of QD charge sensors, discuss radio frequency reflectometry as a technique for fast readout, and introduce the principles of AFM.

2.3 Noise Sources and Sensitivity Limits

After introducing the concept of charge sensing based on Coulomb blockade, this section discusses the key noise sources affecting charge detection and states the charge sensitivity limits of SET-based sensors.

SETs are among the most sensitive electrometers available, capable of detecting sub-single-electron charge variations in nearby systems. Nevertheless, their performance is limited by different factors. [41] In particular, noise sources that set the signal-to-noise ratio (SNR), the coupling strength to the system under investigation, and the intrinsic capacitance of the device are some of the key limitations. [41] The figure of merit for a charge sensor is the charge sensitivity δQ, expressed in units of $e/\sqrt{\text{Hz}}$. This sensitivity is defined as the smallest detectable charge variation per 1 Hz measurement bandwidth and can be expressed as:

$$\delta Q = \frac{\sqrt{S_I}}{|\frac{\partial I}{\partial Q}|} \tag{2.6}$$

with S_I the current noise spectral density (the noise power per unit bandwidth) and $\partial I/\partial Q$ the response of the current through the sensor QD to a variation in the charge on the sample that is being measured. [41]

The sensitivity of a QD charge sensor is fundamentally limited by several noise mechanisms. [41] These noise sources limit the smallest detectable charge signal and also impact the speed of measurements. One is shot noise, which originates from the discrete nature of charge carriers tunneling through barriers. Even at zero temperature, shot noise contributes to current fluctuations and is relevant in single-electron devices at low currents. [42] The theoretical limit set by shot noise of SETs is reported to be approximately $1 \times 10^{-6}\, e/\sqrt{\text{Hz}}$. [41, 43, 44] The corresponding spectral density is given by:

$$S_I^{shot} = 2eIF \tag{2.7}$$

with I the average device current and F the Fano factor [41], yielding:

$$\delta Q_{shot} = \frac{\sqrt{S_I^{shot}}}{|\frac{\partial I}{\partial Q}|} \tag{2.8}$$

Low-frequency (1/f) noise also plays an important role. It arises from time-dependent occupation of charge traps and defects in semiconductor interfaces and environment and it appears as slow, random fluctuations. [42] It can be expressed as:

$$S_I^{1/f} = A_I^2/f \tag{2.9}$$

where A_I^2 is the current noise amplitude and f the frequency. [45] The corresponding charge sensitivity is given by:

$$\delta Q_{1/f} = \frac{\sqrt{S_I^{1/f}}}{|\frac{\partial I}{\partial Q}|} \tag{2.10}$$

A fundamental limit on sensitivity is also set by the Johnson-Nyquist current noise, caused by the random thermal motion of electrons in resistive components. This white noise occurs at all frequencies and increases with higher temperatures. [42, 46] Johnson-Nyquist noise is described by:

$$S_I^{JN} = 4k_B T/R \tag{2.11}$$

with R being the effective resistance and T the temperature. [47, 48] The corresponding sensitivity is:

$$\delta Q_{JN} = \frac{\sqrt{S_I^{JN}}}{|\frac{\partial I}{\partial Q}|} \tag{2.12}$$

Beyond the thermal, shot, and 1/f terms, additional noise is introduced by the measurement chain, arising from the measurement electronics, such as preamplifier or radio frequency (RF) reflectometry circuits, which can mask small charge signals and thereby limit the effective sensor performance. In practice, this contribution is often comparable or larger than the intrinsic device noise. [42] In the present work, only the principal noise mechanisms are considered. A comprehensive accounting and modeling of all possible technical noise sources in the readout chain lies beyond the scope of this thesis.

Early implementations of SET sensors with RF reflectometry achieve sensitivities on the order of $10^{-5}\,\mathrm{e}/\sqrt{\mathrm{Hz}}$, enabling single-shot readout of spin qubits on sub-microsecond timescales. [6] Later Angus et al. [49] demonstrate a silicon based RF-SET with electrostatically tunable tunnel barriers, reaching sensitivities better than $10^{-5}\,\mathrm{e}/\sqrt{\mathrm{Hz}}$. More recently, Ahmed et al. [50] report a charge sensitivity of $1.3 \times 10^{-6}\,\mathrm{e}/\sqrt{\mathrm{Hz}}$ using a gate-based dispersive readout scheme, where the plunger gate of a QD is embedded in an RF resonator and charge transitions are detected as capacitance variations. [50]

Although both RF-SETs and gate-based sensors report sensitivities in the same units, their detection principles differ. In an RF-SET, induced charge on the island directly modulates the source-drain current, and sensitivity is defined by the ratio of current noise to the charge transconductance. In contrast, in gate-based dispersive sensing, a change in QD occupancy modifies the effective capacitance of the resonator, and sensitivity is defined from the measured RF phase shift.

Whether single-electron tunneling events can be resolved in real time depends on the interplay of sensitivity and bandwidth. Conventional DC measurements are usually too slow, due to the time resolution of milliseconds. This limitation originates from the RC time constant of the measurement circuit, which sets the maximum achievable bandwidth. In contrast, RF reflectometry (Section 2.4), overcomes the RC bandwidth limit by integrating the charge sensor in a resonant circuit, making detection at MHz frequencies possible, while maintaining high sensitivity. [41]

2.4 Radio-Frequency Reflectometry

While the previous section addresses the fundamental noise sources and sensitivity limits of charge sensors, this section provides a brief overview of RF reflectometry. RF reflectometry is a powerful technique which can enhance readout bandwidth and sensitivity in QD systems. Although RF reflectometry is widely used in static measurements of charge sensors and SETs, it is not implemented in the work presented here. Due to practical challenges such as signal routing, system integration, and impedance matching in combination with limited time, RF reflectometry readout has not yet been successfully realized in the setup used here.

Conventional low-frequency readout of QD charge sensors is limited by the effect of parasitic capacitance and high resistance, which together form a large RC time constant and restrict the measurement bandwidth. [51] RF reflectometry provides a way to increase the operational frequency closer to the intrinsic limit of the device set by the tunneling dynamics of the device, and thus operating above the 1/f noise and improving both charge sensitivity and measurement speed. [6, 41]

RF reflectometry is based on monitoring the reflection of a high-frequency signal applied to an LC matching network via a contact or gate lead to the charge sensor (see Figure 2.3). The matching circuit transforms the high device impedance to $50\,\Omega$, enabling efficient coupling to the transmission line. The reflected signal is highly sensitive to the impedance of the sensor, which strongly depends on the conductance of the QD. [6] Any change in nearby charges modifies the sensor conductance, thereby changing the reflection coefficient of the circuit. [37]

A typical setup can be seen in Figure 2.3, where a charge sensor is connected to a resonant tank circuit, consisting of an inductor L_C and a capacitor C_P. The resonant frequency f is given by:

$$f = \frac{1}{2\pi\sqrt{L_C C_P}} \tag{2.13}$$

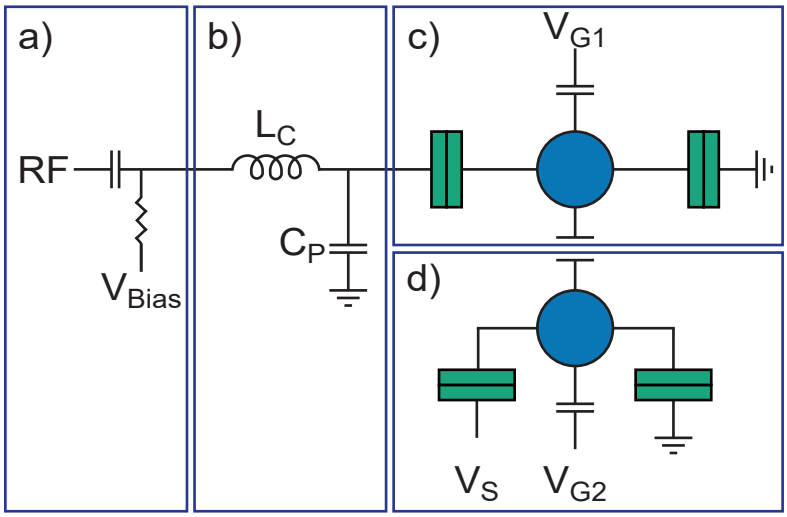

Figure 2.3: Schematic of an RF-QD/SET charge sensor capacitively coupled to a single QD. **a)** The RF carrier is applied via a coaxial line into a bias tee, which combines the RF excitation with a DC bias voltage (V_{Bias}). **b)** The signal passes through the LC matching network consisting of an inductor L_C and capacitor C_P, connected to one of the contact leads of the charge sensor. **c)** Charge sensing QD (blue) with source and drain tunnel barriers (green), coupled to an external gate electrode held at V_{G1}. **d)** Device under investigation, here represented by another QD, capacitively coupled to the charge sensor gate and controlled via V_S and V_{G2}. Adapted from [41].

A carrier signal at frequency f is applied to the circuit and the reflected signal is monitored using homodyne or heterodyne detection. In homodyne detection, the reflected signal is mixed with a local oscillator at the same frequency to extract the amplitude and phase. In heterodyne detection, the local oscillator frequency differs slightly from the carrier, producing an intermediate frequency (IF) signal that can be more easily amplified and processed. [41] When the impedance of the sensing dot is changed, the reflected signal is altered in phase and amplitude. [52] This reflected signal can be measured with a high signal-to-noise ratio. The key advantage of RF reflectometry is that readout can be performed at frequencies far beyond the typical RC cutoff of DC setups. Instead of the sensor's wiring capacitance and resistance limiting the bandwidth, in RF the bandwidth is determined by the quality factor Q of the resonator.

$$\text{Bandwidth} = \frac{f}{Q} \tag{2.14}$$

Bandwidths of 1 - 10 MHz have been achieved using suitable matching and low-loss components, enabling sub-microsecond charge detection. [37] This has been very

important for readout of spin and charge qubits in semiconductor QDs.

Schoelkopf et al. [6] are the first to implement RF reflectometry with SETs and achieved real-time detection of charge motion. Since then, RF readout has been used in various quantum devices, such as semiconductor QDs [52, 53], carbon nanotube devices [54], high-fidelity spin readout in silicon [37], and many others [37, 41]. Using RF reflectometry, charge sensitivities of about $10^{-5}\,\mathrm{e}/\sqrt{\mathrm{Hz}}$ [37, 41, 52] have been demonstrated. Compatible with compact integration, cryogenic operation, and multiplexing (addressing several charge sensors simultaneously using distinct RF frequencies), RF reflectometry is a powerful tool for QD sensors. [55]

Although RF reflectometry enables fast and sensitive charge detection and is widely used in static QD measurements, it has not yet been successfully employed in the measurements presented in this work.

2.5 AFM Mechanics and Electrostatics

The sensor used in this work incorporates two core elements: the AFM platform for the nanoscale spatial resolution and a sensor unit at the AFM tip. In this section the fundamental principle of AFM is introduced, which forms the mechanical and positional backbone of the scanning probe sensors used in this work. It begins by reviewing the operational principles, components, and modes of AFM.

AFM relies on a micro- or nanoscale cantilever that acts as a mechanical resonator. It can create topographical images with an out-of-plane sub-nanometer resolution over a range of micrometers. The out-of-plane resolution is mainly limited by the performance of the nanopositioning system and the system's vibration level, whereas the in-plane resolution is limited by the mode of operation and by the tip radius of the probe. [3] As schematically displayed in Figure 2.4, a conventional AFM consists of mainly three subsystems: the controller electronics, the nanopositioning system, and the cantilever probe.

The controller electronics are crucial for avoiding damage to the cantilever probe and the sample and to ensure good imaging performance. AFM control systems are usually built around a field-programmable gate array (FPGA), which handles the control routines and main digital logic. Signal conditioning circuits and driver electronics are usually implemented on custom printed circuit boards (PCBs) and serve as the analog front end to sensor and actuator interfaces. For advanced imaging, modes such as amplitude or frequency modulated dynamic AFM, additional signal processing components, e.g., phase-locked loops (PLLs) and lock-in amplifiers are needed within the controller. To enhance tracking performance during the imaging experiment, the gains of the proportional-integral-derivative (PID) controller must

be tuned by the user. [3, 56]

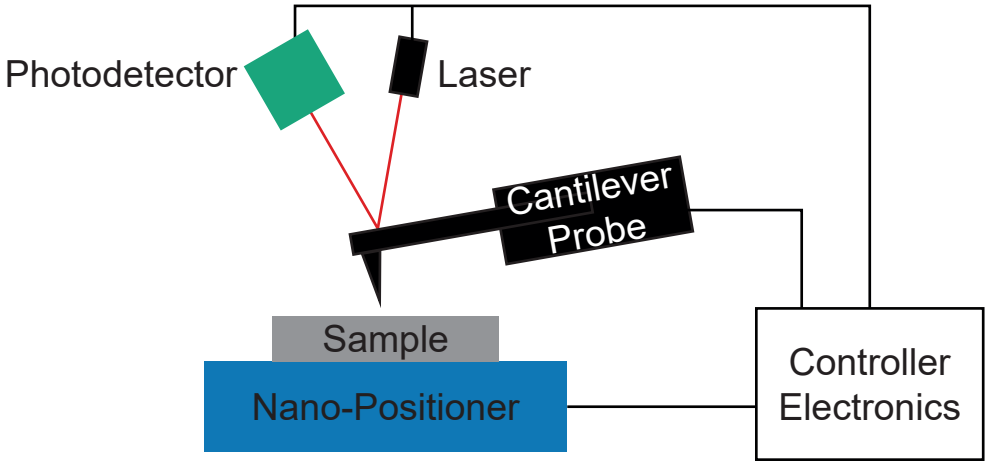

Figure 2.4: Schematic of a basic AFM setup employing optical beam-deflection detection. The three main subsystems are: the controller electronics, which interacts with all components, the nanopositioning system enables precise relative positioning of the sample with respect to the cantilever probe, and the cantilever probe with optical readout, where a laser beam is reflected onto a position-sensitive photodetector to measure cantilever deflection caused by tip-sample interactions.

To navigate and set the relative position between the probe tip and the sample surface, a nanopositioning system is needed. Depending on the mode of operation, the cantilever's deflection or oscillation is regulated by adjusting the distance between the sample surface and the probe tip. This relative motion can either be accomplished by scanning the cantilever tip relative to the sample or vice versa. [3]

A standard AFM probe is composed of a sharp tip mounted on a microcantilever attached to a base chip. Such probes are made using standard nanofabrication techniques from materials such as silicon nitride, silicon dioxide, or silicon. To track the deflection of the cantilever, a laser and a quadrant photodetector are used in most systems. This enables sub-nanometer sensitivity. Other sensing readout techniques include interferometry, piezoresistivity, piezoelectricity, and optomechanical sensing. [57] For dynamic operation, typically a piezo actuator is used to excite the cantilever at its resonance. Depending on the application, different actuation mechanisms are employed, including thermomechanical, electrostatic, photothermal, and electromagnetic methods. [57]

AFM imaging can be operated in different modes. The first AFM imaging mode invented was the contact mode. The tip raster-scans the sample and adjusts its

height to maintain a constant force on the sample. This leads to a topographic image of the sample. [58] In contact mode the tip is in constant contact with the surface, which leads to high lateral forces during scanning and reduces the AFM tip's lifetime. Dynamic mode imaging was developed to reduce both tip-sample force and friction. In the dynamic mode the cantilever is oscillated near its resonance frequency and the amplitude and the resonance frequency are used as a feedback parameter to adapt the tip height while scanning above the sample. In addition to these two primary AFM imaging modes, other dynamic imaging modes have been developed and applied. [58]

Electrostatic interactions between the sample surface and the cantilever tip are also relevant in AFM. Arising from capacitive coupling of the tip and the sample, these long-range forces depend on the distance of tip and sample and the potential difference. [59] In standard AFM imaging, electrostatic interaction can distort topographic measurements or can be mapped as it is done in Kelvin probe force microscopy (KPFM). [60] In charge sensing applications, the electrostatic interactions become the actual signal. Electrostatic forces on the tip are modulated by local variations in nearby charge distributions. These variations can be detected by the cantilever deflection in terms of frequency shifts or by how much energy is needed to keep the lever oscillating at a constant amplitude. [60]

Both the tip and the cantilever of the AFM probe can be modified for different applications. For example, the material and geometry of the tip can be optimized for a high-aspect ratio sample with a very sharp tip, or the cantilever can be coated with reflective gold to improve laser detection performance, or one particularly powerful extension of this concept is the integration of an SET at the tip of an AFM cantilever, enabling spatially resolved charge sensing.

2.6 Scanning SET and Scanning Gate Microscopy

This section provides an overview of prior implementations of scanning approaches based on SETs and scanning gate microscopy (SGM). It highlights the key implementations and the notable achievements to illustrate how these techniques have been employed. The aim is to place the work of this thesis in the context of earlier methods and to show what has been accomplished with such sensors so far.

As discussed in Section 2.2, SETs are highly sensitive charge detectors, which are capable of sensing sub-electron charge variations due to their Coulomb blockade characteristics. Integrating an SET into a scanning probe platform enables spatially resolved measurements of electrostatic potentials and charge distributions at the nanoscale. Two related but distinct approaches have emerged: scanning SET

microscopy, where an SET is raster-scanned across a sample to detect local charge distributions, and SGM, where a biased metallic tip is scanned over a nanostructure while the transport response is monitored. Both techniques provide insight into confinement, electrostatics, and charge transport in mesoscopic systems.

One of the first scanning SETs is realized by Yoo et al. [9]. An $Al/AlO_x/Al$ SET is fabricated at the tip of a quartz tuning fork to map the surface electric potential of a 2DEG in a $GaAs/Al_xGa_{1-x}As$ heterostructure. The SET is raster-scanned above the sample surface at cryogenic temperatures. This work demonstrates the feasibility of using an SET to image and measure local capacitance, band bending, contact potentials, and depleted regions at sub-micrometer length scales. Furthermore, SETs are successfully used to image the local electronic density in graphene [10] and the electrostatic potential, transparency, and Hall voltage in a quantum Hall state in a 2DEG of a GaAs/AlGaAs heterojunction. [61] In a later study, Su et al. report successful integration of an SET-based on silicon-on-insulator technology with an intrinsic charge sensitivity of 10^{-5}-$10^{-3}\,e/\sqrt{Hz}$ at liquid helium (LHe) temperature. [25] However, the study does not include spatially resolved measurements or experimental demonstration involving external samples. Further advances integrate SETs and QDs defined in carbon nanotubes (CNTs) on micromachined cantilevers to improve mechanical stability and spatial resolution. [62] Experiments with such devices enable simultaneous imaging of local voltage and current density in 2D conductors [12], imaging of oxide interfaces [11], hydrodynamic electron flows [13], and Wigner crystals [14].

Unlike SET-based scanning probes, which directly sense charge, SGM employs a biased tip as a movable gate to modulate the local electrostatic potential landscapes. As the tip is scanned across the sample, transport through a nearby nanostructure is monitored. This technique enables mapping the influence of changes in electrostatic potential with nanometer spatial resolution. One of the earliest scanning-gate implementations is demonstrated by Gurevich et al. [63] They add an additional electrode next to the tunneling tip of a cantilever and use it to perform single-electron tunneling spectroscopy on a gold cluster. Their results demonstrate the ability to study and modulate transport through nanostructures using a scanning gate. [63] Topinka et al. [64] use SGM to map branched electron flow from a quantum point contact (QPC) in a 2DEG, producing real-space images of electron trajectories. In a follow-up [65], they resolve interference fringes arising from coherent backscattering, thereby demonstrating the power of SGM to visualize quantum interference phenomena. The SGM tip behaves as a local gate and can therefore be used as a mobile gate to study Coulomb blockade in QDs. Woodside et al. [66] use a metallic tip to locally control the potential landscape on a carbon nanotube QD, revealing the location of individual dots within the nanotube. Similar

experiments are done by Bleszynski et al. [67], where they use a charged tip to image electron flow through an InAs NW. Complementary to SGM, AFM-based electrostatic force detection has imaged, spectroscopically characterized, and resolved excited states of few-electron quantum dots via frequency-shift and dissipation mapping [68, 69]. The above-mentioned work represents only a subset of the extensive work done using SGM to explore mesoscopic transport. Even these selected examples illustrate the flexibility of SGM in investigating quantum transport phenomena across different platforms. For a more comprehensive overview, the reader is referred to the review by Sellier et al. [70]. Another use of having single or multiple gates on the tip of an AFM cantilever is introduced by Shim et al. [71], where they propose to induce a QD on the material system with a separated probe chip, e.g., an AFM lever with gates. This leads to the possibility to characterize parameters which are important for semiconductor QD devices without fabricating such devices on the material. [71]

The development of scanning SET and SGM illustrates the versatility of using scanning probe setups. Both approaches have provided remarkable insights into nanoscale transport and charge distribution, although they are not without limitations. The scanning SET of Yoo et al. [9] lacks the integration with an AFM cantilever, limiting the scan stability and spatial resolution. The SET integrated on an AFM tip by Su et al. [25] was never shown to do actual scanning. Scanning SET using QDs defined in CNTs, which is used to publish remarkable work [11–14, 62], are not combined with dynamic mode of an AFM cantilever, making it difficult to use for samples with high-aspect-ratio structures. Scanning gate microscopy on the other hand provides only indirect information, depends strongly on the tip-induced perturbations, and published work includes only single gates on the tip of the cantilever. These constraints have prompted the exploration of other approaches. One of them is the integration of a QD embedded in a NW on the tip of a commercial non-contact (NC) AFM lever, combining the strength of established AFM scanning probe methods with the high charge sensitivity of a QD. Another approach explored is the integration of more than one electric gate at the tip of a NC-AFM lever. Compared to the work done in SGM, this provides the advantage of addressing multiple gates simultaneously and, as proposed by Shim et al. [71], can enable the non-destructive characterization of semiconductor wafers by locally inducing QDs in the material system of interest. Before elaborating about the approaches described, a broader comparison of available charge sensors and their advantages and limitations is undertaken, placing the method used in this work in perspective to other existing technologies.

2.7 Comparison to Other Charge Sensors

To motivate the choice of a semiconductor SET as the core element of the used scanning probe charge sensor, it is essential to compare it to other existing charge sensing techniques. These include superconducting SETs, metallic SETs, QPCs, field-effect-transistor (FET) sensors, and nitrogen-vacancy (NV) centers in diamond. Most of these approaches provide direct charge detection, relying on the influence of local charges on transport or optical properties. Additionally, other scanning probe techniques such as scanning capacitance microscopy (SCM) [72], scanning tunneling microscopy (STM) [73], and KPFM [74] give mapping information about carrier density, dielectric properties, surface potential, or electronic density. However, sub-electron sensitivity is in practice not achieved in a noninvasive, broadly applicable scanning mode, and therefore are not considered viable candidates for realizing a scanning charge sensor.

In the present application, a suitable charge sensor must fulfill three criteria: (I) it must offer excellent charge sensitivity, ideally in the range of $10^{-5}\,\mathrm{e}/\sqrt{\mathrm{Hz}}$ or better, (II) it must operate at temperatures attainable within the used liquid helium setup ($\sim$4.2 K), and (III) it must be possible to integrate it onto the tip of an AFM cantilever. Table 2.1 summarizes representative sensitivities, readout methods, and operating temperatures for the main sensor classes, which are then discussed in turn. The following comparison describes the operational principles, reports representative charge sensitivities, and highlights the limitations of each approach considered for the scanning charge sensor.

Sensor Type	**Readout**	**Charge Sensitivity**	**Temp.**	**Ref**
Semiconductor SET	RF	$<10\times10^{-6}\,\mathrm{e}/\sqrt{\mathrm{Hz}}$	100 mK	[49]
Superconducting SET	RF	$0.9\times10^{-6}\,\mathrm{e}/\sqrt{\mathrm{Hz}}$	40 mK	[75]
Metallic SET	RF	$1.9\times10^{-6}\,\mathrm{e}/\sqrt{\mathrm{Hz}}$	4.2 K	[75]
QPC	RF	$2\times10^{-4}\,\mathrm{e}/\sqrt{\mathrm{Hz}}$	60 mK	[52]
FET	DC	$4\times10^{-5}\,\mathrm{e}/\sqrt{\mathrm{Hz}}$	25 K	[76]
FET	DC	$6\times10^{-5}\,\mathrm{e}/\sqrt{\mathrm{Hz}}$	198 K	[76]
FET	DC	$0.2\,\mathrm{e}/\sqrt{\mathrm{Hz}}$	300 K	[77]
NV Center	Optical	$5.3\,\mathrm{e}/\sqrt{\mathrm{Hz}}$	300 K	[78]

Table 2.1: Representative charge sensitivities for different charge sensors, with corresponding readout methods, operating temperatures, and references.

As described in Section 2.1 and 2.2 an SET consists of an island tunnel coupled to source and drain contacts and capacitively coupled to a gate (see Figure 2.1).

Semiconductor SETs have been realized in various material platforms, including 2DEG, semiconductor NWs, carbon nanotubes, and other low-dimensional systems. One of the best reported charge sensitivity in semiconductors is below $10 \times 10^{-6}\,\mathrm{e}/\sqrt{\mathrm{Hz}}$ [49] using RF readoutBarthel et al. [79] compare the charge sensitivity of an SET defined in a $GaAs/Al_{0.3}Ga_{0.7}As$ heterostructure with the charge sensitivity of a QPC defined in the same material. They find a 30 times higher charge sensitivity and three times better SNR for the SET compared to the QPC. [79] Despite high charge sensitivity and compatibility with the scanning probe integration, semiconductor SETs also have their challenges. Semiconductor SETs require cryogenic temperature to show Coulomb blockade although depending on the confinement it does not require millikelvin temperatures. The devices are highly sensitive to fabrication variation and couple to nearby charge noise sources, which affects the stability of the device. Nonetheless, in the context of building a charge sensor to be used in the scanning probe setup, these trade-offs are outweighed by the benefits of nanoscale resolution and direct charge detection.

There have been superconducting SETs, which are coupled to an RF readout setup and report charge sensitivity close to the shot noise limit of $0.9 \times 10^{-6}\,\mathrm{e}/\sqrt{\mathrm{Hz}}$. [75, 80] The requirement for millikelvin temperatures makes them unsuitable for use in the setup presented in Chapter 3.

Then, there are metallic SETs, which can for example be fabricated with a two-angle evaporation of aluminum on SiO_2 and in situ oxidation, resulting in thin tunnel barriers between the island and source/drain contacts. Such devices can be ultrasensitive and can also be combined with RF, which was done by Brenning et al. [75], where they report a charge sensitivity at 4.2 K of $1.9 \times 10^{-6} e/\sqrt{\mathrm{Hz}}$. Compared to the semiconductor SET the charge sensitivity is similar. Although fabrication on a quartz tuning fork is demonstrated [9], integration onto standard AFM cantilever would differ.Additionally, most metallic SETs, such as the one shown by Yoo et al. [9], operate at temperatures in the millikelvin region.

A QPC is a narrow constriction, usually in a 2DEG, which passes electrons one by one, leading to conductance quantization in steps of $2e^2/h$. Such QPCs can be used to read out electronic occupation in nearby, capacitively coupled systems. [34] For such devices, most commonly a substrate hosting a 2DEG and electrical gates to tune the channel are needed. One of the best reported charge sensitivities of a QPC is measured using RF. Cassidy et al. [52] estimate a sensitivity of about $2 \times 10^{-4}\,\mathrm{e}/\sqrt{\mathrm{Hz}}$ with a bandwidth exceeding 20 MHz. In comparison with SETs, QPCs are less noisy, offering the potential to reach the quantum limit of detection. This is because SETs rely on single-electron tunneling events which induce higher detector noise to the system. [81] At this point QPCs offer moderate charge sensitivity compared to SETs, and most QPC devices are made in 2DEGs

which would be challenging to integrate on the tip of an AFM cantilever.

FETs can also function as charge sensors, in which current flowing between two terminals is modulated by an electrical field. Using NW FETs as a charge sensor, Salfi et al. [76] report a charge sensitivity of $4 \times 10^{-5}\,\mathrm{e}/\sqrt{\mathrm{Hz}}$ at 25 K. A FET is even fabricated on the apex of a silicon-on-insulator chip and used in combination with a tuning fork scanning technique to image electric potential profiles and topography of samples at room temperature showing a charge sensitivity of $0.2\,\mathrm{e}/\sqrt{\mathrm{Hz}}$. [77] FET-based sensors are not as sensitive to charge as SETs and FETs also require stronger capacitive coupling to measure a modulation in current. While the reported FET charge sensitivity of $4 \times 10^{-5}\,\mathrm{e}/\sqrt{\mathrm{Hz}}$ [76] is close to the one of SETs the need for stronger capacitively coupling would mean that scanning has to be done closer to the sample, which increases the risk of damaging the sensor, therefore, FET approaches are not pursued.

NV centers are electric-field sensors but can also be used as charge sensors. An NV center is a defect in the crystal lattice of diamond, where a nitrogen atom is placed adjacent to a carbon vacancy. The spin of single defect centers in diamond is used to sense electric-field-dependent shifts (Stark shift) in energy levels. [82] In the work done by Barson et al. they report a near single-charge sensitivity of $5.3\,\mathrm{e}/\sqrt{\mathrm{Hz}}$ at ambient temperatures. [78] A fundamental difference to the other above-mentioned sensors is that NV centers are read out optically. As charge sensitivities of NV centers are several orders of magnitude worse than those of semiconductor SETs, and considering the indirect detection of charge via electric fields, NV centers were not considered a suitable candidate.

Beyond NV centers, other optically read out quantum devices have been integrated into scanning probes for electric-field mapping. Cadeddu et al. [83] demonstrate in situ electric field sensing using a single self-assembled InAs QD mounted at the apex of a tapered optical fiber probe. The QD's excitonic transition is monitored optically, and shifts in the resonance energy due to the Stark effect provide a measure of the electrostatic field. While this approach showed that nanoscale electric field imaging is not restricted to transport readout schemes such as SETs, the reported sensitivity is orders of magnitude lower than that of state-of-the-art transport sensors, and the need for optical access makes integration into the scanning probe impractical. While both, the Cadeddu et al. [83] QD probe and NV center sensors are sensitive to local electric fields, neither measures charge sensitivity directly. In case of Cadeddu et al. [83] they report electric field sensitivity of $1.4 \times 10^{6}\,(\mathrm{V/m})/\sqrt{\mathrm{Hz}}$. Converting this to a charge sensitivity would require assuming a specific tip-sample capacitance and geometry, which is not provided in the work and would introduce significant uncertainty. Similarly, in the NV center study by Barson et al. [78], the charge sensitivity is not measured directly but

derived from the electric field sensitivity using a simplified model of the AFM tip as conducting sphere of radius 25 nm. Only the Barson et al. [78] value is included in the Table 2.1, since the authors explicitly perform this conversion, whereas including the Cadeddu et al. [83] result would require additional calculations not presented in their paper.

In summary, there exist various approaches for charge detection, including superconducting SETs, metallic SETs, QPC, FETs, and NV centers, whereas semiconductor SETs offer the most favorable combination of high charge sensitivity, compatibility with the used scanning probe setup (see Chapter 3), and integrability.

Chapter 3

Experimental Setup

This chapter presents a description of the experimental platform developed for cryogenic scanning probe measurements with integrated electrical transport capabilities. It is structured as follows:

- Section 3.1 introduces the cryostat, detailing the cooling system, base temperature performance, and vibration isolation strategies.
- Section 3.2 describes the scanning probe insert, including the mechanical structure, electrical cabling, thermal anchoring, integrated RC filters, and radio frequency reflectometry compatible wiring infrastructure.
- Section 3.3 focuses on the scanning probe head, covering the cantilever mount, optical path for interferometric detection, and sample positioning unit.
- Section 3.4 outlines the external instrumentation, including the optical readout system, piezo driver electronics, digital-to-analog converter and current amplifiers, as well as grounding strategies.
- Section 3.5 explains the measurement routine and image acquisition, detailing the software control, data acquisition flow, and typical measurement sequence.

Together, these sections provide a detailed understanding of the setup used to perform the experiments presented in this work.

3.1 Cryostat

To perform high-sensitivity scanning probe measurements at cryogenic temperatures, a reliable and well-shielded low-temperature environment is essential. The experiments are conducted in a liquid helium bath cryostat equipped with a superconducting magnet. This chapter describes the design and operational principles of the cryostat, highlighting its thermal architecture and vibration isolation, both of which are critical for stable low-noise scanning probe measurements.

The basis of the scanning probe setup is a liquid nitrogen-shielded liquid helium bath cryostat made by Cryomagnetics, Inc. It consists of an inner LHe bath to cool the sample space and the superconducting magnet. The superconducting magnet can apply a magnetic field up to 8 T in z-direction. The helium bath is surrounded by an inner vacuum shield, to minimize thermal conduction. Next, there is a liquid nitrogen (LN_2) bath in order to intercept the heat coming from outside to reach the helium bath. Surrounding the entire cryostat is an additional vacuum shell, which provides an extra layer of thermal insulation. A helium recovery line connected to the liquid helium bath feeds back the evaporated helium to the in-house helium liquefier. The system needs to be refilled regularly with LHe and LN_2, and can typically be kept cold for about one week without refilling. The level of the LHe and LN_2 can be read via a liquid cryogen monitor[1]. The cryostat is mounted on a rigid metal support frame, which itself sits on four passive, air-pressurized air-damped vibration-isolation legs[2].

3.2 Scanning-Probe Insert

The cryostat described above provides the cryogenic environment required for the experiments. Mounted inside the cryostat, the custom-built scanning probe insert forms the core of the experimental system. It integrates all key components required for scanning probe measurements: the cantilever and its optical detection path, sample and lens positioning systems, signal wiring, thermal anchoring stages, and the sample holder. The insert is engineered for low-temperature scanning probe measurements. Particular attention is given to wiring, grounding, and shielding to ensure that delicate sensors and samples are protected from electrical noise and voltage spikes throughout cooldown and operation.

[1] LM-510 Liquid Cryogen Monitor, Cryomagnetics, Inc.
[2] S-2000A Stabilizer, Newport

3.2.1 Mechanical Structure

To ensure mechanical stability, thermal anchoring, and compatibility with high-vacuum cryogenic environment, the insert is constructed around an architecture that spans from room temperature (RT) to the base temperature of the cryostat. Its design accommodates all required interfaces for electrical, optical, and mechanical connections while providing a rigid framework for mounting and supporting the scanning probe components. The following describes the structural layout and key elements enabling thermalization, vacuum access, and integration of the probe head. Starting with the rigid support tube which serves as the mechanical backbone of the insert.

The support tube is made of stainless steel, chosen for its mechanical stability, low thermal conductivity, non-magnetic nature, and vacuum compatibility. The support tube also has five concentric radiation shields, which are mounted around the support tube to reduce radiative heat load onto the cryogenic components (see Figure 3.1).

At the top of the insert tube, six ConFlat (CF) flanges provide vacuum-tight electrical, optical, and pumping access to the insert. One flange is equipped with a coaxial feedthrough[3] for four individual coaxial high-frequency lines. An optical fiber feedthrough[4] enables interferometric readout of the cantilever. Two CF flanges host 32-pin electrical feedthroughs[5] one is used for controlling all the piezos of the system. The other is used to connect to the sample and sensor. The fifth flange is equipped with a valve[6] and connects the vacuum pump[7] to the system and the sixth flange is used for a pressure relief valve[8], for safety reasons.

At the bottom of the support tube there is a copper cold base welded to it (see Figure 3.1). This cold base is in direct thermal contact with the surrounding LHe and serves as the primary thermal anchor point for all the components requiring base temperature. Mounted onto this copper plate is a removable stainless steel can. The can is secured mechanically using titanium screws and sealed with indium[9] to ensure vacuum compatibility and is pumped via the steel tube. This allows for repeated opening and closing at RT, making it possible to mount and dismount sensor and sample, plus giving the possibility to adapt components mounted below the cold base.

[3]Double ended 50 Ohm matched impedance SMA connector IFDCG042013, Kurt J. Lesker
[4]Singlemode SM1310 FC/APC Pro, Vacom
[5]MPC2 single-ended pin contacts, Vacom
[6]Stainless Steel Gate Valves 11120-0154, High Vacuum Valves
[7]TPS-compact Turbo Pumping System, Agilent
[8]6 PSI Pressure Relief Valve, Accu-Glass Products, Inc.
[9]Indium (99.99%) wire 1.6 mm diameter, CMR-Direct

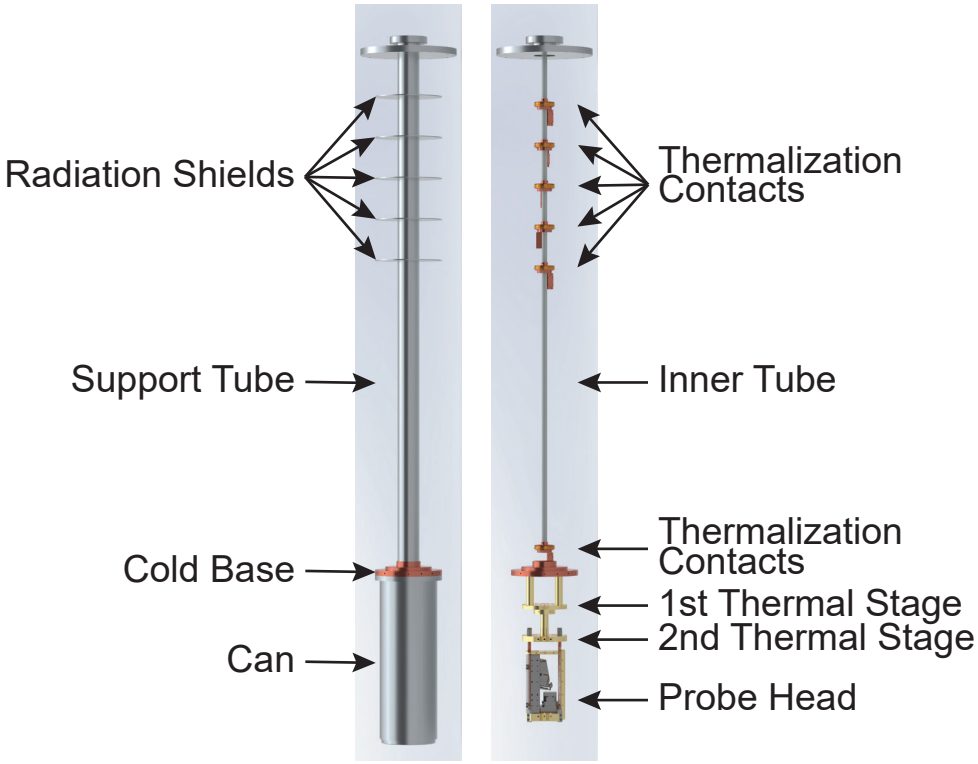

Figure 3.1: Rendered images of the probe insert. **Left:** Probe with the supporting tube and can in place. The supporting tube carries multiple radiation shields, while the cold base at the bottom provides thermal contact to the liquid helium bath and serves as the mounting point for the can. **Right:** Probe with the supporting tube and can removed, revealing the inner tube extending from RT to 4.2 K. Along its length, thermalization contacts are used to thermally anchor the cables. At the bottom, two thermal stages are mounted to the cold base. The second thermal stage supports the probe head, which is suspended via springs and contains the microscope assembly.

Inside the can, mounted directly to the cold base, is the first gold-plated thermal stage. Below the first stage sits the second stage, from which the scanning probe head is suspended via four copper beryllium springs for vibrational isolation. The head houses the cantilever with the integrated sensor, the optical lens for interferometric readout, the sample, and all the piezoelectric elements for positioning and actuation.

Enclosed in the support tube is a secondary tube made of fiberglass, which has poor thermal conductivity and thereby reduces heat transfer. The single-mode fiber is routed through this inner tube down the probe. Outside the tube there are six spring-loaded copper thermalization contacts, where five of them are positioned at the same vertical locations as the concentric radiation shields. The sixth thermalization contact is at the bottom of the support tube and is connected via copper braid to the cold base plate. The thermalization contacts are for stepwise thermal anchoring for the wires ensuring progressive heat sinking from RT to LHe temperature.

To ensure reliable electrical operation within the insert, a carefully designed cabling scheme is implemented. It accommodates high-voltage piezo control, low-noise signal acquisition, and thermal anchoring, while preserving ground isolation between the high-voltage piezo lines and the low-noise measurement lines.

3.2.2 Cabling

A modular and thermally-considered cabling design is developed to interface the scanning probe components with external instrumentation. Two 32-pin vacuum feedthroughs provide access to separately routed wire bundles for piezo control and signal acquisition. Each bundle is tailored in terms of wire materials, shielding, and grounding to match its electrical function and thermal requirements. The layout minimizes electromagnetic interference, ground loops, and thermal load while maintaining compatibility with cryogenic conditions.

Inside the insert, four separate wire bundles run down the steel tube: one for the Attocube piezo control lines, one for the cantilever actuator piezo, and two additional bundles carrying all remaining lines. Since the piezo bundles are connected to a dedicated feedthrough, their grounds are electrically isolated from the two remaining bundles. Each wire bundle is equipped with dedicated shielding appropriate to its function. The two wire bundles carrying the remaining lines share identical shielding configurations, while the others differ.

Shielding, spatial separation, and ground decoupling within the system are implemented because voltage pulses with amplitudes of up to 65 V at frequencies of 300 Hz to control the Attocube piezo steppers have to be applied. Prior to implementing shielding, spatial separation, and ground decoupling voltage spikes of several volts are observed on all lines during piezo operation. Such high noise on the lines destroys all the delicate sensors and samples.

At both ends of the probe, the wire terminations are prepared in the same manner: the insulation at the wire ends is carefully removed using a razor blade, and the

conductors are soldered[10] to connector contacts and the joints are encapsulated with cryogenic Teflon shrinking tubes[11] to ensure electrical insulation despite the dense arrangement of pins and potential cable movement during assembly and cooldown. At the top of the probe, the wires are soldered to male D-sub connector contacts[12], whereas at the bottom they are soldered to female receptacle pins[13]. The use of leaded solder is chosen for its superior mechanical reliability at cryogenic temperatures, while the detachable pin system facilitates reconfiguration without resoldering.

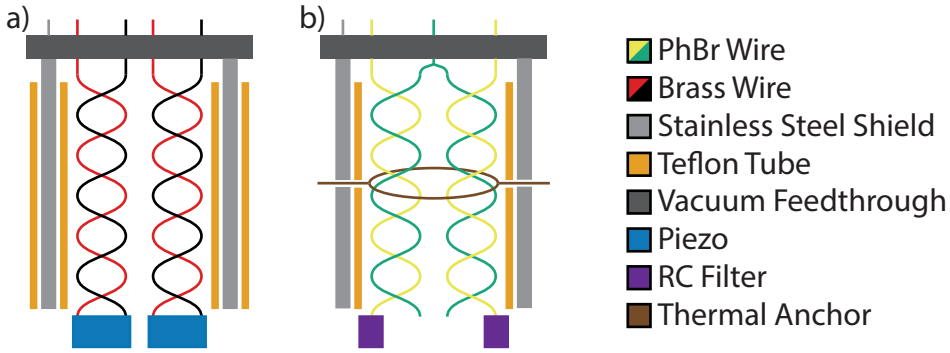

Figure 3.2: Schematic of the wiring bundles for the piezos a) and the sample/sensor lines b). **a)** The piezo bundle consists of twisted pair brass wires enclosed in an inner Teflon tube (orange), a stainless steel shield (gray), and an outer Teflon tube (orange). This arrangement provides both electromagnetic shielding and isolation between the piezo bundle ground and the probe ground. Each wire is individually connected to separate pins of the top feedthrough, with the shield grounded via a dedicated pin. At the bottom end, the wires are directly connected to the piezos. **b)** The sample/sensor wiring uses twisted pair phosphor bronze wires, enclosed in a Teflon tube (orange) and a stainless steel shield (gray) without an outer Teflon layer. Each twisted pair has one wire as signal and the other as wire to ground. These wires are thermally anchored along the probe length. The signal lines are routed such that all grounds remain floating at the bottom and are tied together only at the top to a single feedthrough pin. At the second gold-plated thermal stage of the probe, the signal wires are connected to RC filters going afterward to the sample/sensor.

[10]Leaded No-Clean Wire Solder Sn63Pb37, Kester
[11]Teflon Cryogenic heatshrink tubes, CMR-Direct
[12]D-Sub Conn Contacts 66504-4, TE Connectivity
[13]65020 Receptacle with a solder cup, Preci-Dip

For the actuator piezo, twisted pair brass wire[14] is used. Twisting minimizes electromagnetic pickup and cross-talk. Brass is not as thermally conducting as, for example copper but still electrically conducts well enough to drive the actuator piezo. The actuator piezo bundle is surrounded by a Teflon tube[15], which serves as a mechanical guide to constrain its path within the probe. No metallic shielding is employed here, as only voltages in the range of 10 mV are applied to those lines. For the actuator piezo lines, each twisted pair consists of two wires, where each is connected to separate pins on the feedthrough, including the ground lines. One of the wires carries the actuation signal, while the other carries ground. At the bottom of the probe, the wires are directly connected to the actuator piezo.

For the Attocube piezo cabling twisted pairs of brass[14] wires are also used. The Attocube cable bundle is enclosed in a thin-wall Teflon tube[15], surrounded by a flexible stainless steel shield[16], and finally covered with a larger-diameter Teflon tube[15] (see Figure 3.2). With the outer tube it is possible to have them shielded and to decouple the probe ground from the metallic shield ground within the probe. In addition to the shielding and the decoupling from the ground within the probe, the actuator and Attocube piezo bundles are also spatially separated from the other lines, by running them down the tube on the opposite side.

For the Attocube piezo lines, one wire of each twisted pair is designated as ground. All ground and signal wires of the Attocube piezo lines are individually connected to separate pins. At the bottom of the probe, the wires connect directly to the dedicated piezo. Importantly, all the piezo lines, including the actuator lines, are not thermally anchored at the spring-loaded copper thermalization contacts or further down the probe. Although this configuration is not optimal in terms of thermal management perspective, separate grounding of the piezo lines and the remaining lines could not be implemented otherwise. Directly connecting the two grounds led to sample damage, potentially due to ground loops.

The remaining signal lines connecting to the second 32-pin feedthrough are for the sample, cantilever sensor, temperature sensor, amplifier, and some spare wires in case some would get damaged. For the amplifier, which is explained in Section 3.2.4, twisted pair brass wires[14] are used. All other wires are twisted pair phosphor bronze wires[17] to minimize heat leak into the system. Each of the two wire bundles is shielded using a Teflon shield[15] and a stainless steel shield[16] which is electrically connected to the probe ground. In each twisted pair, one wire is designated as the local ground. All those ground wires are electrically connected together at the top

[14]Enamelled Ms 90 wire 0.25 mm Polysol 155, Elektrisola
[15]Thin Wall Teflon Insulating Tubing, SPC Technology
[16]Flexible Shielding Stainless Steel, Accu-Glass Products, Inc.
[17]Duo-Twist cryogenic wire WDT-32, LakeShore Cryotronics

of the insert and routed to one common ground pin on the vacuum feedthrough (see Figure 3.2). In contrast, each signal wire is individually connected to its dedicated pin on the feedthrough, ensuring isolated routing of the lines. At the bottom of the probe all wires going to the sample or the sensor are routed through a two stage RC low-pass filter sitting on the second gold-plated thermal stage. The used RC filters are described in Section 3.2.3. The brass wires for the amplifier, as well as the wires for the temperature sensor, are routed directly to their respective components.

Despite extensive shielding and grounding strategies, high-frequency voltage spikes remain a critical threat to sensitive devices. To provide an additional layer of protection, all signal lines to the sensor and sample are routed through dedicated low-pass RC filters. These filters, mounted close to the base temperature, help suppress residual noise and transients, and are the focus of the next section.

3.2.3 RC Filters

Since very delicate samples are studied, which will get damaged if there are voltage spikes, a two stage RC low-pass filter is employed. All lines going to the sample or the sensor are run through the RC filters at the second gold-plated thermal stage. A schematic of the used circuit can be seen in Figure 3.3.

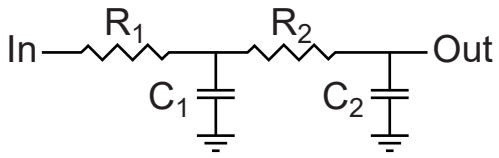

Figure 3.3: Schematic of the RC filter used to protect the sample from high-frequency noise and voltage transients. The filter consists of two cascaded RC stages, each consisting of a resistor ($R_1 = 510\,\Omega$, $R_2 = 2\,k\Omega$) in series with the signal path and a capacitor ($C_1 = 1.2\,\mathrm{nF}$, $C_2 = 220\,\mathrm{pF}$) connected to ground. This configuration attenuates high-frequency components while allowing low-frequency signals to pass with minimal loss.

The filter board implemented consists of the input passing through a $510\,\Omega$ resistor (R_1), then a $1.2\,\mathrm{nF}$ capacitor (C_1) to ground as the first stage and for the second stage it continues through a $2\,k\Omega$ resistor (R_2), followed by a $220\,\mathrm{pF}$ capacitor (C_2) to ground. The ground nodes of both capacitors are tied to the probe ground at the corresponding thermal stage, providing a well-defined ground. This layout creates a two-pole filter with enhanced suppression of high-frequency noise relative to a single RC section. The effective cutoff frequencies of the two stages are approximately

$f_{c1} \approx 260\,\text{kHz}$ and $f_{c2} \approx 360\,\text{kHz}$, respectively, providing broadband attenuation of unwanted signals. This relatively simple circuit offers effective line filtering for a cryogenic measurement setup.

While the RC filters provide efficient suppression of high-frequency noise and voltage spikes on the DC lines, high-frequency signal handling requires a dedicated approach. To this end, a separate RF line architecture is integrated within the probe, enabling future implementation of reflectometry-based measurements and high-speed charge sensing. The design and thermal integration of these RF components are detailed in the following section.

3.2.4 RF Circuit and Amplifier

Although RF reflectometry is not used in the experiments presented in this work, the scanning probe system is designed to support such measurements. An RF-compatible wiring infrastructure is included to enable future integration of high-frequency detection schemes.

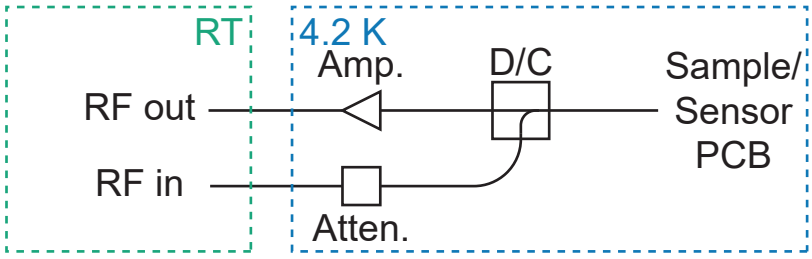

Figure 3.4: Schematic of the RF reflectometry circuit integrated into the probe. An RF signal is injected at the RF in port at RT and transmitted to the cryogenic stage through a cryogenic attenuator (Atten.). The attenuated signal is routed via a cryogenic directional coupler (D/C) to the sample PCB and subsequently to the sample. The reflected signal follows the reverse path, passing from the directional coupler to a cryogenic amplifier (Amp.) and then to the RF out port at the vacuum feedthrough of the probe, where it is analyzed by the RT detection electronics.

For the RF setup, the insert is equipped with four semi-rigid coaxial lines[18] extending from the RT vacuum feedthrough at the top down to the cold base. All coaxial lines are individually clamped to the spring-loaded copper thermalization contacts to ensure effective heat sinking and reducing thermal load on the cold base temperature stage. From the cold base onward, each coaxial line transitions to

[18]Stainless steel 50 Ohm semi-rigid cables UT-085B-SS, Micro-Coax (Amphenol)

flexible coaxial cable[19]. This transition reduces mechanical stress on the connectors and compensates thermal contraction of the lines caused by the cooldown. In addition, it also allows for easier routing and bending within the confined geometry, for example to connect to the cryogenic amplifier[20] or an attenuator[21]. One of the lines is used as the main RF input. It is connected to a cryogenic attenuator[22], which is thermalized at the first gold-plated thermal stage. The attenuated signal is then routed to the output port of a cryogenic directional coupler[23], located between the first and second gold-plated thermal stage. The input port of the coupler is connected to the sample, such that the signal from the attenuated line goes to the sample via the coupler, with an additional attenuation. The signal is then reflected from the sample and is collected with minimal attenuation at the coupled port of the directional coupler and routed to the cryogenic amplifier mounted on the first thermal stage. The amplified signal is then routed back to RT via a second semi-rigid coaxial line (see Figure 3.4).

One of the two remaining coaxial lines can be connected via an additional attenuator at the first thermal stage to a gate electrode on the AFM lever or sample and is intended to be used as a fast pulsing gate. The fourth coaxial line is reserved for future upgrades or as a backup.

With all mechanical, thermal, and electrical interfaces in place, the scanning probe insert provides the necessary infrastructure to host and operate the sensor system under cryogenic conditions. At the core of this setup lies the scanning probe head, which integrates the cantilever sensor, sample holder, positioning elements, and optical readout. The following section details the design and implementation of this central component.

3.3 Scanning-Probe Head

Situated at the coldest and most vibration-isolated point of the scanning probe insert, the scanning probe head forms the core of the experimental setup. It integrates all components required for sensing, actuation, sample positioning, and optical readout within a compact and thermally anchored platform.

As described in Section 3.2, the scanning probe head is suspended from the second thermal stage via four copper beryllium springs for passive vibrational isolation. The basis of the scanning probe head consists of a gold-plated copper platform,

[19]Formable 047 Semi-rigid Coax Cable with Tinned Copper Braid Outer Conductor, Pasternack
[20]Cryogenic Low Noise Amplifier $LNF - LNC0.3_14A$, Low Noise Factory AB
[21]Atten 2.92mm-f/f 18GHz 1W bulkhead, XMA Corporation-Omni Spectra
[22]Atten 2.92mm-f/f 18GHz 1W bulkhead -20dB, XMA Corporation-Omni Spectra
[23]Coaxial Directional Coupler ZEDC-15-2B, Mini-Circuits

referred to as spring plate, which serves as the mechanical support of the head. To ensure good thermalization, four flexible copper braids connect the second thermal stage directly with the spring plate, providing a good thermal connection.

The conceptual design of the scanning probe system is based on keeping the AFM cantilever at a fixed position, while scanning the sample relative to it. The cantilever can be driven into oscillation using a piezoelectric actuator, integrated on the cantilever holder, enabling dynamic AFM operation modes. Optical interferometry is used to detect the cantilever's motion with high sensitivity. To focus the interferometer beam onto the cantilever, an optical lens is aligned using a stack of positioners.

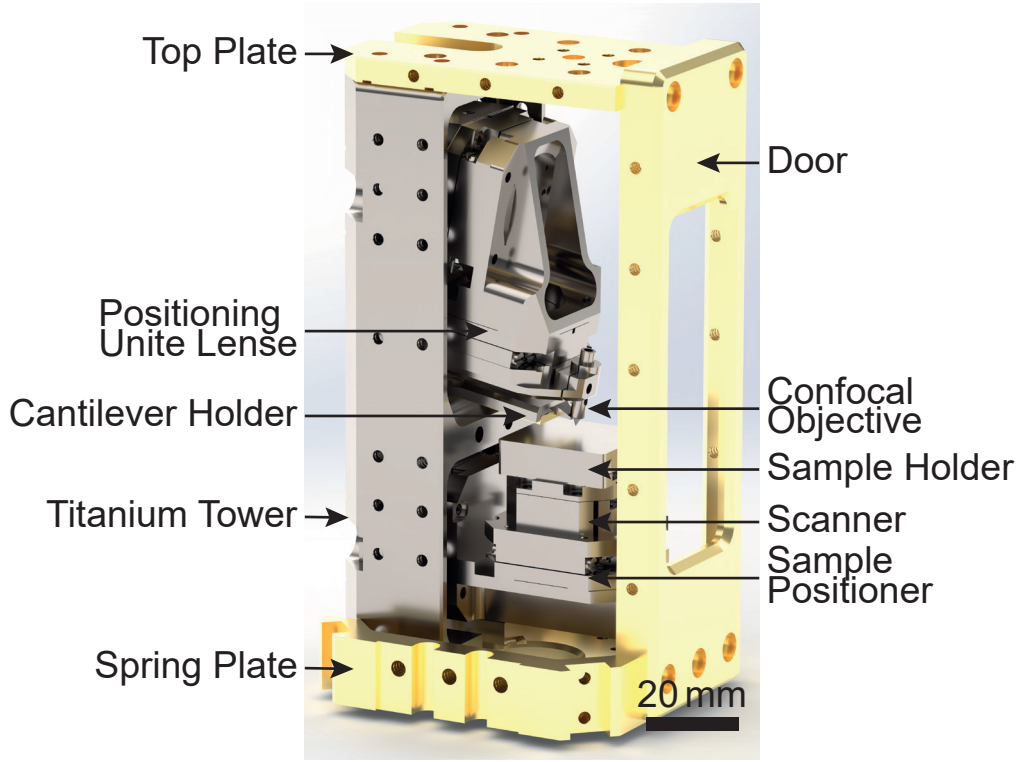

Figure 3.5: Rendered image of the scanning probe head. At the bottom, the spring plate is mounted to the second thermalization stage via four springs (not shown) to provide vibration isolation. On one side, a rigid titanium tower supports the cantilever holder, the positioning unit for the confocal objective lens, the lens holder itself, as well as a second positioning unit and scanner for precise sample positioning. Opposite the titanium tower, a gold-coated door provides access for mounting and dismounting the sample. The door is mechanically connected at the top to the titanium tower via the top plate and directly to the spring plate at the bottom, ensuring rigidity and mechanical stability.

On one side of the spring plate a rigid titanium tower hosts the cantilever holder, the positioning unit for positioning the lens and a second unit to position the sample, and the lens holder itself. The nanopositioning unit for sample positioning and scanning protrudes forwards so that the sample stage is located at the center of the spring plate, although its base is fixed to the titanium tower. Opposite to this tower, a gold-coated copper door provides accessibility for sensor and sample mounting/dismounting. These two vertical components are mechanically joined by a gold-plated copper top plate to build a frame in order for stability, as can be seen in Figure 3.5. The top plate additionally hosts a temperature sensor[24]. The place for the temperature sensor is chosen to be as close as possible to the sample but without interfering with scanning or sample mounting/dismounting.

In the following sections a detailed description of the AFM lever holder, including the PCB and integrated actuator piezo, the optical interferometer readout system, and the positioning and scanning unit for sample translation will be given.

3.3.1 AFM Cantilever Assembly: Holder, Actuator, and PCB Integration

To operate the AFM cantilever, a dedicated holder is designed to meet several key requirements: It must be easily mounted and dismounted from the probe, provide a dedicated place for the cantilever to be glued on, include an actuator piezo for mechanical excitation of the lever, and integrate a compact PCB that incorporates required circuitry and electrical connectors. The connectors have to interface with the RC filtered lines and it must be possible to wire-bond from the PCB to the cantilever's bonding pads. The resulting design is shown in Figure 3.6.

At the front of the holder, a machined groove provides a platform for gluing[25] the cantilever. Threaded holes are made to mount the PCB as well as additional holes to attach the holder to a flat base plate compatible with the used wire-bonder[26]. A dedicated place on the bottom side of the holder accommodates the actuator piezo disk[27]. To electrically insulate the disk from the holder, a layer of Kapton tape is first applied. On top of the Kapton tape, a small PCB piece is glued to provide a convenient solderable surface. The piezodisk is then glued[25] onto the PCB. Electrical connection of the disk requires contacts to both top and bottom side. The bottom contact is realized by soldering[10] a wire to the PCB surface, while the top contact is established by soldering a second wire directly to the upper

[24]Cernox 1030 sensor in MT package, calibration 1.4-325K, LakeShore Cryotronics
[25]Electrically Conductive Silver Epoxy EPO-TEK E4110, Epoxy Technology, INC.
[26]Series 56i, F&S Bondtec
[27]Piezodisk PRYY-000053024, PI Ceramic GmbH

electrode of the piezodisk. This can be seen in Figure 3.6b. Both wires are then routed to an adapter, allowing connection to the dedicated 32-pin piezo feedthrough. On the back of the holder, two additional holes allow secure mounting to the rigid titanium tower inside the scanning probe head. The geometry of the holder is designed such that the cantilever is positioned at a 10° angle relative to the sample plane, making sure the tip of the cantilever approaches the sample surface first. Below these two mounting holes, an additional threaded hole is provided to attach an auxiliary extension piece. This extension helps with a more convenient and safe insertion and removal of the cantilever holder during mounting and dismounting procedure within the scanning head. Once the holder is installed, the extension is removed.

Beyond the mechanical design, the cantilever holder also integrates a custom PCB to route electrical signals. The PCB design supports both fast gate pulsing and sensitive charge readout via RF reflectometry, while maintaining independent control of up to five DC gate lines. For the electrical connection to the RC filter, signal lines are routed via brass wires[14] and connectors[28]. A schematic of the custom PCB circuit can be seen in Figure 3.6. It is designed to interface DC control lines and RF signals with quantum devices under test. Five bias lines, labeled with Pad 1 to Pad 5, route signals via wire-bonds to the sample, while connectors Gate 1 to Gate 6 receive external signals from the top of the probe via the RC filters. In addition, two RF lines (RF 1, RF 2) are available for high-frequency operation.

Lines for Pad 2, Pad 3 and Pad 4 are pure DC lines, directly connected to their respective input pins Gate 2, Gate 3, and Gate 4. These lines are exclusively used for low frequency gate control and DC biasing. The line for Pad 5 includes a bias-tee circuit, allowing simultaneous application of DC voltage (via Gate 5) and RF pulses (via RF 2). The RF path is high-pass filtered using capacitors C_4 (22 pF) and C_5 (22 nF), leading to a cutoff frequency of 145 kHz. The DC path is low-pass filtered using capacitor C_6 (100 nF) and resistor R_3 (10 MΩ) yielding a cutoff frequency of 0.16 Hz. Pad 1, which is configured as a reflectometry channel, also employs a bias-tee structure. It combines a DC signal (Gate 1) with an RF signal (RF 1). The DC path is low-pass filtered by a capacitor C_1 (100 pF) and a resistor R_1 (5 kΩ) with a cutoff frequency of 318 kHz. The RF path contains a tunable impedance matching network composed of a fixed capacitor C_2 (87 pF), a tunable varactor acting as a shunt capacitor, and an inductor L_1 (470 nH). The varactor, e.g. based on strontium titanate [84], is voltage tuned via Gate 6 and enables fine matching to the sample impedance.

[28] CONN RCPT 6POS 0.079 GOLD PCB, Harwin Inc.

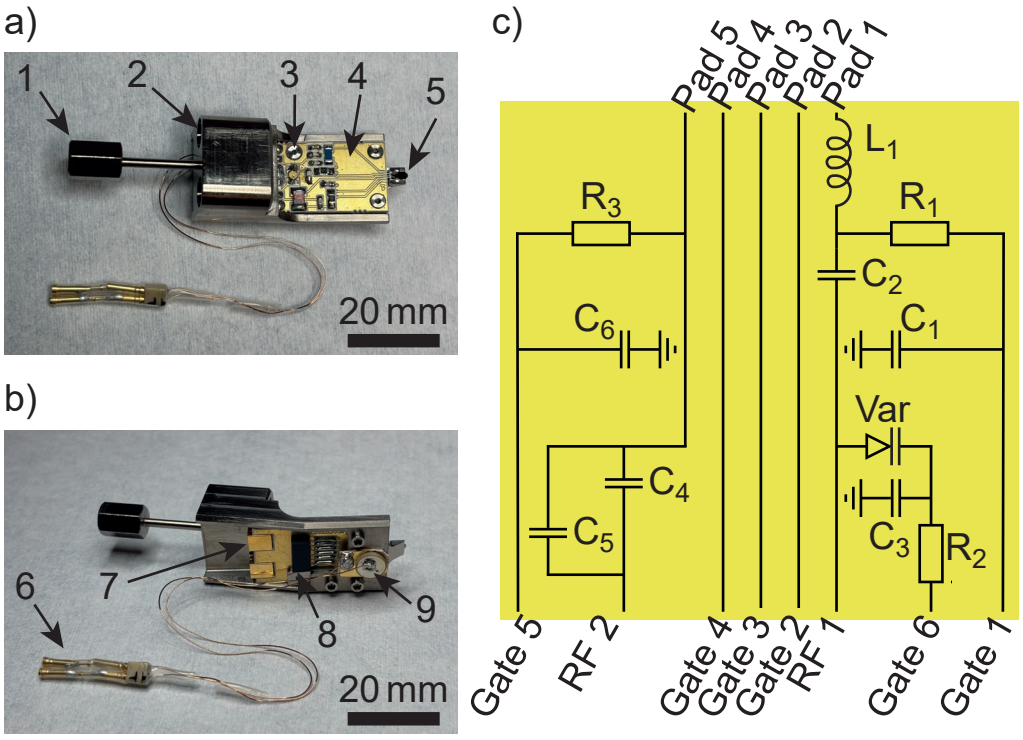

Figure 3.6: Optical images of the holder with 1. auxiliary extension, 2. mounting holes, 3. screws holding PCB, 4. PCB, 5. cantilever, 6. actuator connection, 7. RF line connections, 8. DC lines connections, and 9. actuator piezo disk, along with the schematic of the PCB circuit. **a)** Top view and **b)** bottom view of the titanium holder body. **c)** Schematic of PCB circuit with six gate lines and five pad lines. Pad 1 combines a DC path with an RF signal via an impedance matching network, while Pad 5 incorporates a bias-tee for applying both DC and RF signals.

To ensure robust electrostatic protection during installation, each pin (Gate 1-Gate 6) on the PCB is equipped with two soldered connectors in parallel. One of these connectors is dedicated to grounding and is used to electrically short all the pins to the PCB ground during the whole time of wire bonding and mounting. This ensures that both the PCB body and all signal lines remain on the same potential, preventing electrostatic discharge events during handling. Importantly, the cantilever remains grounded through the whole mounting process, including the connection of its contact to the probe connector. The grounding bridge is only removed after all other electrical connections are established. This precaution is critical, as damage to the cantilever sensor was observed in earlier trials when the grounding was done differently or not done at all. With the cantilever holder

assembly providing both electrical integration and mechanical stability, precise interferometric detection of the cantilever motion becomes possible. The following section describes the optical path, including the fiber-coupled objective and its alignment system.

3.3.2 Optical Path

To detect the motion of the AFM cantilever with high sensitivity, a fiber-based optical interferometer is employed. The optical path consists of a single-mode fiber delivering the light and a compact confocal objective focusing the beam onto the backside of the cantilever. Inside the probe, a single-mode optical fiber[29] with an FC/APC connector on one end and a custom-built confocal objective on the other is routed through the support tube, as described in Section 3.2. The confocal objective consists of a titanium housing, a glass ferrule, and a compact aspheric lens[30]. Assembly begins by gluing[31] the aspheric lens to one end of the titanium housing. The fiber-ferrule assembly purchased with a glass ferrule on one end is fixed in place at a distance of approximately the effective focal length (1.69 mm) of the lens. During this process, the optical beam is monitored to ensure proper alignment. The completed confocal objective is mounted on the dedicated positioning unit located within the titanium tower (see Figure 3.5). The positioning unit incorporates steppers along all three spatial directions (x, y, z[32]), allowing precise alignment of the laser beam onto the reflective backside of the AFM cantilever positioned below. This optical path forms the basis for a fiber-based interferometer used to readout the motion of the cantilever, as described in Section 3.4.1. With the cantilever and optical detection system in place, precise control over the sample position becomes the next essential component for scanning probe measurements.

3.3.3 Sample Positioners

Accurate positioning and scanning of the sample relative to the cantilever is a central requirement for scanning probe microscopy. To enable this, the sample is mounted on a multi-axis nanopositioning system that provides both coarse and fine control. Installed beneath the AFM cantilever is the sample, which is mounted on a nanopositioning unit consisting of three Attocube nanopositioners used for stepping (x and y[32], z[33]) for coarse positioning in all three spatial directions

[29]SMF-28-Custom, ThorLabs
[30]Aspheric Lens 352450C, AMS Technologies
[31]Torr Seal epoxy resin 9530001, Agilent
[32]Nanopositioner ANPx311/LT/HV, attocube systems GmbH
[33]Nanopositionier ANPx311/HL/LT/HV, attocube systems GmbH

(see Figure 3.5). The z nanopositioner is not only used for stepping but also for fine positioning in z-direction. Additionally, there is a dedicated piezoelectric scanner, for fine positioning and scanning in x and y directions[34]. According to the manufacturer's specifications, the x-y scanner offers a scanning range of 30 µm×30 µm at a temperature of 4.2 K, while the z positioner has a range of 800 nm. However, as discussed in Section 5.1, the effective scan range observed in the scanning probe measurements deviates from the nominal specifications.

All piezo elements are connected via dedicated wiring to the 32-pin electrical feedthrough reserved for piezo control, as described in Section 3.2.2. To facilitate straightforward mounting and removal of the sample, a titanium sample stage is screwed onto the positioning unit. This stage incorporates a sliding mechanism, allowing the sample holder to be inserted along guide rails and then secured using clamping screws. This design allows sample exchange even when the cantilever is already fixed in place. The titanium stage is anchored to the spring plate via a copper braid, ensuring good thermal contact and providing an electrical ground to the sample. This copper braid is crucial as the positioning unit does not provide electrical conductivity between their top and bottom interfaces. Moreover, the thermal conductance of the positioning unit is assumed to be insufficient to cool the sample without the added copper braid.

The design and integration of the scanning probe head, including the cantilever assembly, optical interferometric path, and nanopositioning system, form the foundation for cryogenic scanning probe operation. In the following chapter the instrumentation architecture outside the cryostat is described.

3.4 Instruments

The operation of the scanning probe platform relies on a coordinated set of external instruments that generate, route, and monitor all electrical and optical signals connected to the cryogenic insert. Here the instrumentation infrastructure outside the cryostat, including signal generation and readout hardware, the optical interferometry system, piezo driver and scanning control, as well as grounding and filtering strategies are detailed. For clarity, the section is divided into two main parts: the first focuses on the control and readout of the AFM system, while the second addresses instrumentation for electrical transport measurements.

[34] xy-Scanner ANSx100lr/LT/HV, attocube systems GmbH

3.4.1 AFM Control and Readout

The instrumentation for operating the AFM cantilever includes both optical detection and mechanical actuation. Displacement is monitored using a fiber-based interferometric readout, while scanning and positioning are controlled via a piezoelectric driver integrated with the system control software. The following two sections describe these components.

Optical Interferometric Readout System

Among the various cantilever deflection detection schemes developed for AFM, optical interferometry offers high displacement sensitivity and is particularly well suited for cryogenic and ultra-high-vacuum environments. [85, 86] A fully fiber-coupled interferometer is employed to transduce the cantilever motion into an optical intensity modulation. This approach leverages mature designs from earlier interferometric AFM systems [87–89] and benefits from prior implementation expertise within the research group [90, 91]. The optical path inside the probe insert, including the fiber routing, confocal objective, and alignment mechanics, is described in Section 3.3.2. In this section, the operating principle of the interferometer and the external instruments used for the readout and stabilization is described.

The interferometer detection is based on a cleaved single-mode fiber end at a short distance to a reflective backside of the cantilever, forming a so-called Fabry-Pérot cavity. [92] The fiber end is fixed inside a titanium housing that includes an aspheric lens, which focuses the beam onto the cantilever's backside. The titanium housing is mounted on a positioning stage to enable precise alignment of the focal spot on the backside of the cantilever. When laser light is sent through the fiber, one part of it is reflected at the fiber-air interface, while the remaining part exits the fiber, reflects off the cantilever surface, and partially couples back into the fiber. The reflected light from the fiber end and the reflected light from the cantilever result in an interference and therefore in an intensity modulation at the output of the fiber. The modulation depends on the difference of the optical path length and therefore the cantilever displacement. A schematic of the optical path can be seen in Figure 3.7.

To realize this principle experimentally, a stabilized laser source and fiber-coupling scheme are employed. The light source is a laser diode head[35] operating at a wavelength of 1550 nm, controlled via a digital laser controller[36] that provides control over laser current and temperature. The laser drive current is set to 18 mA. Using the specified slope efficiency (0.147 W/A) and threshold current (14 mA),

[35] Distributed-feedback laser pro LD-1550-0040-DFB-8, Toptica
[36] DLC pro, Toptica

the nominal optical output is $P = \eta(I - I_{th}) \simeq 0.6\,\mathrm{mW}$. The laser from the diode is injected into Port 1 of a fused single-mode fiber coupler[37] with a nominal coupling ratio of 99:1 (port 1 to Port 4 and Port 3). The 1 % power output (port 3) is connected to the optical fiber feedthrough of the insert via an FC/APC connector. The light from port 3 propagates down the insert and enters the Fabry-Pérot cavity formed at the cantilever. The reflected signal from the cavity travels back through the same optical path and enters the single-mode fused fiber coupler for a second time at Port 3, which directs 99 % of the return signal to Port 2. Port 2 is connected to a fiber-optic receiver[38] converting the optical laser signal into an electrical signal. A schematic can be seen in Figure 3.7.

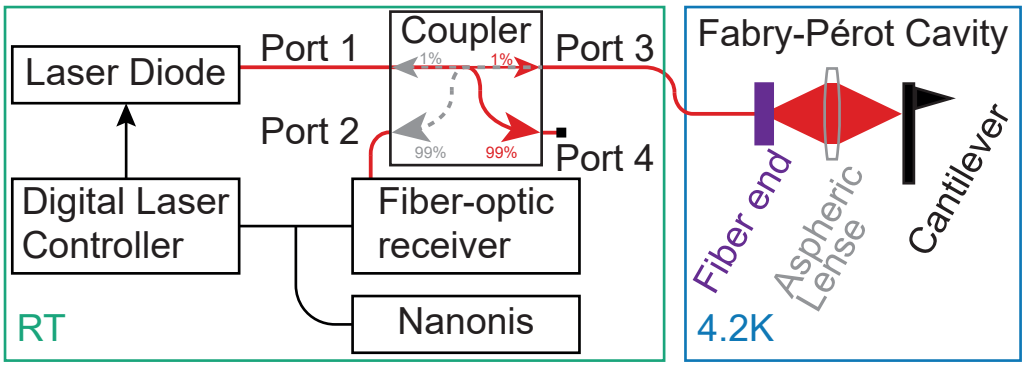

Figure 3.7: Schematic of the fiber-based interferometric detection system. A 1550 nm laser is coupled into a fiber coupler, sending light down the probe to the cantilever backside where a Fabry-Pérot cavity is formed. The reflected signal returns through the same optical path to the coupler and from there the signal is directed (via Port 2, gray) to a fiber-optic receiver, with the output used for both interferometer stabilization and cantilever motion readout via the Nanonis system.

The fiber-optic receiver includes an adjustable gain stage which is set to 10^3V/mW and features independently adjustable 6-dB high- and low-pass filters. In the present setup the high-pass filter is set to DC and the low-pass filter to 1 MHz. The resulting electrical signal is routed to the input monitor of the digital laser controller. Using the controller software, the laser frequency is locked to a flank of a selected interference fringe via an internal PID feedback loop which adjusts the laser temperature, thereby tuning its emission wavelength. This active stabilization compensates for slow thermal drifts in the cavity length. The high-frequency mechanical motion of the cantilever induces fast intensity modulations around the lock point. These modulations are demodulated to extract the AFM cantilever

[37] 2x2 Wideband Fiber Optic Coupler 1550 nm ± 100 nm 99:1 Split FC/APC, ThorLabs
[38] Fiber-Optic Receiver Model 2053-FC, Newport Corporation

dynamics. To do so, the fiber-optic receiver is also connected to the Nanonis control system[39] (see Figure 3.7).

In addition to detecting the cantilever motion, the functionality of the AFM requires precise and coordinated control of the cantilever's position relative to the sample. This is achieved through dedicated scanning and actuation hardware, which interfaces with the system control software and integrates both coarse and fine positioning elements.

AFM Scanning Control and Actuation

This section details the external hardware used to actuate the piezo elements for both stepping and scanning operations, as well as the software environments responsible for scan execution and synchronization. To enable precise scanning, the sample is moved relative to the fixed AFM cantilever using a combination of coarse and fine motion control. Coarse positioning is achieved using Attocube piezo steppers, as described in Section 3.3.3, which provide independent motion in x, y, and z-direction. The steppers are controlled via a modular positioner control unit[40] together with the dedicated stepping module[41]. These components are operated externally and communicate with the Nanonis control system[39]. A schematic of the instrument setup is shown in Figure 3.8, which integrates the optical interference readout discussed above with the electrical transport measurements instruments presented in the following section.

Fine scanning is accomplished using scanner piezos integrated into the sample stage for precise x-y motion, while z displacement is provided by a piezo nanopositioner (see Section 3.3.3). Like the steppers, they are connected to the Attocube positioner control unit, but are operated via a scanner module[42]. The scanning piezos are controlled through the Nanonis system, which provides high-resolution voltage output and synchronized scanning signals.

At the core of the Nanonis system is a high-performance FPGA board that handles all analog and digital inputs/outputs via dedicated analog-to-digital (ADC)/digital-to-analog converter (DAC) boards, enabling nanosecond level synchronization between scanner control, auxiliary drive channels, and data acquisition. This hardware level timing ensures that motion control is fully coordinated with the acquisition of optical interferometer signals from the AFM cantilever.

[39] Nanonis Mimea Base Package BP5e SPM, SPECSGROUP
[40] ANC300, Attocube
[41] ANM150, Attocube
[42] ANM300, Attocube

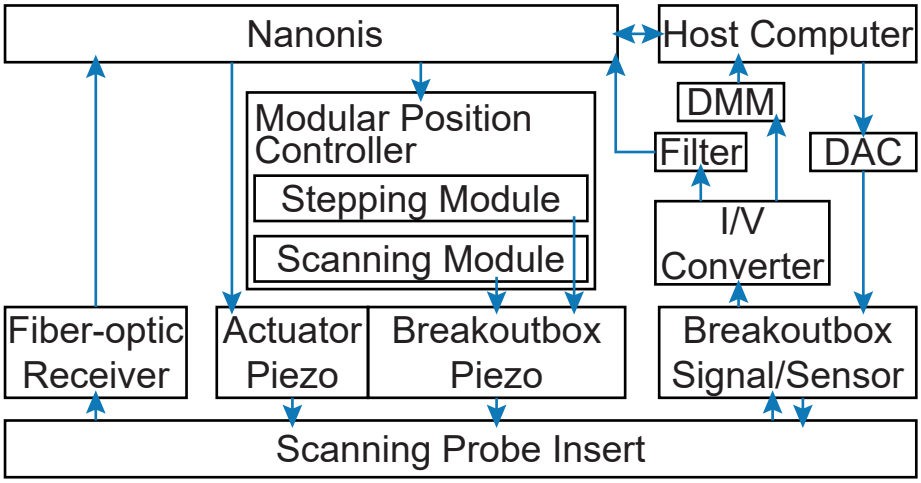

Figure 3.8: Schematic of the instrument setup. The host computer runs the Nanonis control software, which configures measurement parameters and communicates with the Nanonis control system. The Nanonis serves as the central control and data acquisition system. It reads the signal from the fiber-optic receiver to detect the cantilever motion, drives the actuator piezo for cantilever oscillation, and controls both stepping and scanning piezos via the modular position controller. Electrical transport signals from the sample or sensor, measured relative to the cantilever tip position, are routed through an I/V converter (optionally followed by a filter) to the Nanonis. The system thus synchronizes scanning probe operation with simultaneous transport measurements.

Nanonis serves as the central control platform for the approach of the tip to the sample, scanning control, height control (feedback loop for topography/constant-frequency operation), and data acquisition (synchronous recording of electrical and optical readouts).

For mechanical excitation during dynamic AFM operation, the actuator piezo disk is connected to the oscillation controller[43] of the Nanonis system, allowing drive signals to be generated and synchronized within the same platform. Beyond handling input/output synchronization, the FPGA manages the routing of all analog signals to the actuator drive, optical readout, and external controllers such as the positioner and scanner unit. This integration avoids timing mismatches inherent to PC-based systems and provides a single control hub for configuring scanning parameters, executing scans, and acquiring both electrical and optical data.

[43] OC4 oscillation controller, SPECSGROUP

3.4.2 Electrical Transport Measurements

In addition to mechanical control, the experimental platform requires precise electrical interfacing with quantum devices integrated on the cantilever and sample. This includes generating stable bias and gate voltages, monitoring low transport currents, and ensuring robust signal integrity through proper grounding and filtering. Furthermore, accurate temperature monitoring of the scanning head is essential for the cooldown process. The following sections describe the instrumentation for DC signal generation and acquisition, filtering and grounding strategies, and temperature sensing during operation.

DC Signal Generation and Acquisition

Precise generation and acquisition of DC signals are essential for electrical transport measurements. The setup uses a DAC[44] to apply bias and gate voltages to both the sample and the device integrated on the AFM cantilever. The DAC provides high resolution and excellent voltage stability, enabling fine control of the device. A low-noise current-to-voltage (I/V) converter[45] is used to convert small transport currents into measurable voltages. The I/V offers five decades of gain ranging from 10^5 to 10^9 V/A and includes an integrated low-pass filter with an adjustable cut-off between 30 Hz and 100 kHz. This converter is important for monitoring transport currents through the QDs and charge sensors, where the current signal can be on the order of picoamperes. The output voltage of the I/V converter is monitored either using a digital multimeter[46] (DMM), which provides accurate, low-noise DC readout with high resolution or directly via the Nanonis input. All instruments are connected via Bayonet Neill-Concelman (BNC) cables to the dedicated breakout box connected to the top of the insert. From there, signals are routed through the RC-filtered lines described in Section 3.2.2 to the sensor or sample. To ensure that these low-level signals are transmitted reliably and remain at low-noise, careful attention is paid to filtering and grounding, as described in the following section.

Filtering and Grounding

As previously described all signal lines inside the insert are routed through low-pass RC filters (see Section 3.2.3). These connect at the top of the insert to a 32-pin vacuum feedthrough, which interfaces with the external wiring. There is a second 32-pin vacuum feedthrough, which comes from the piezo lines, whose ground is not connected inside the probe. From each feedthrough, a shielded multi-core cable connects to a custom-designed breakout box located outside the cryostat. Each

[44] Low Noise High Resolution DAC SP927, Basel Precision Instruments
[45] Low Noise High Stability I to V Converter SP983, Basel Precision Instruments
[46] 34465A/34411A 6.5 Digit Multimeter Truevolt, Keysight

breakout box provides a BNC connector for every line with a toggle switch to allow each channel to be individually set to either floating or grounded with respect to the box.

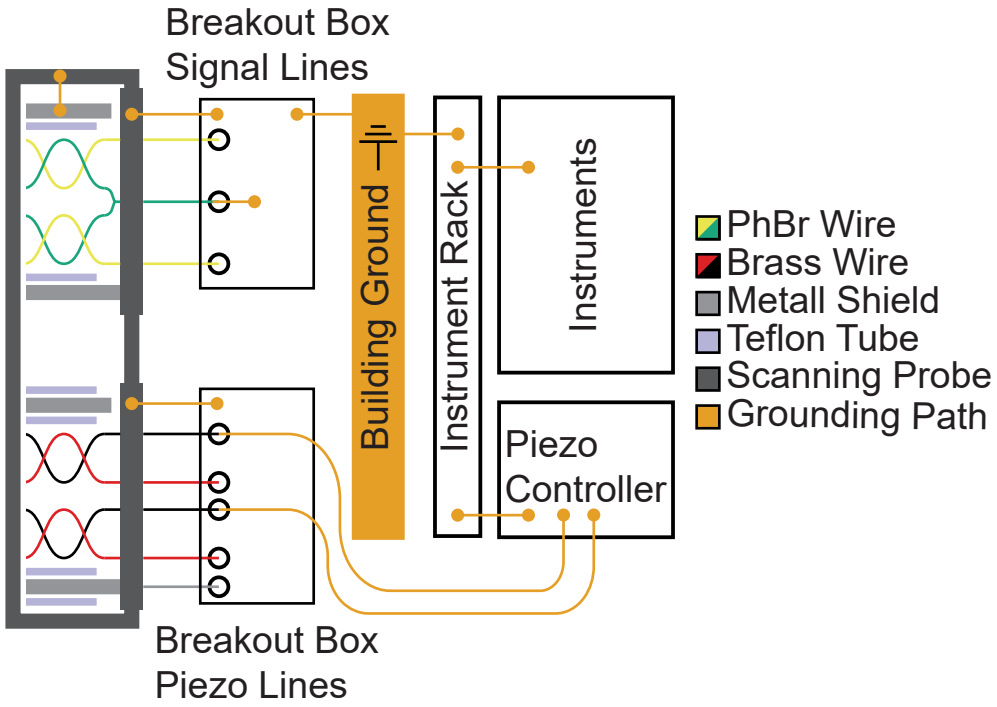

Figure 3.9: Star-like grounding scheme of the measurement setup. A dedicated building ground line is connected to the signal breakout box via a copper braid. From this point, the ground is distributed through the shielding of the signal cables to the cryogenic insert, and further to the breakout box of the piezo lines. In parallel, the building ground is connected to the instrument rack, ensuring that the instruments mounted on the rack share a common chassis reference. The signal grounding lines are tied to the ground potential of the signal breakout box, providing a single reference node for all electrical measurement channels. In contrast, the piezo lines are treated separately. Their ground return is provided directly by the piezo controller, which is itself connected to the building ground through the instrument rack, thereby avoiding ground loops.

During installation and operation proper grounding is essential to prevent sample damage. Therefore, a dedicated building ground line, made of thick copper, is connected to the signal breakout box via a copper braid. From this point, the shielding of the cable connecting the breakout box to the insert is used to ground the probe. All measurement instruments are mounted on grounded instrument

racks, which are via the rack also connected to the building ground using copper braids. This makes sure that all the connected equipment and the scanning probe system have a common ground reference. An illustration of the grounding schema can be seen in Figure 3.9.

To avoid ground loops when connecting multiple output channels from the DAC to the breakout box, only the first BNC cable is connected directly. For all additional DAC outputs, ground decouplers are used to break redundant ground paths which would otherwise introduce noise or voltage offsets.

In contrast, the piezo breakout box is treated differently. It is not directly connected to ground like the signal breakout box. Instead, it is electrically isolated from its surroundings by a cardboard box, ensuring that it does not accidentally make any contact to grounded surfaces. The only ground reference for the piezo lines come from the Attocube piezo driver module, which itself is grounded to the instrument rack and therefore the building ground. This isolation is essential, as improper grounding of the piezo lines has previously caused voltage spikes on sample/sensor lines that led to device damage. As shown in Figure 3.8 filtering is performed using a low-noise preamplifier[47], with the two configurable low-pass or high-pass filters adjusted according to the measurement requirements.

Temperature Monitoring

To accurately monitor the temperature of the scanning head during cooldown, a temperature sensor[24] is installed at the top plate of the scanning head. As discussed in Section 3.3, this location is chosen because it does not interfere with scanning operations or the mounting and dismounting of samples. While direct placement near the sample or sensor is intended for the future optimization of the probe, the selected position offers close proximity to the sample or sensor, ensuring reliable thermal tracking of the region of interest.

With the instrumentation for mechanical control, electrical interfacing, and temperature monitoring in place, the following section describes how these components come together during a typical experimental run, from sample installation to cooldown and scanning.

[47] Low-Noise Voltage Preamplifier SR560, Stanford Research Systems

3.5 Measurement Workflow: From Preparation to Cryogenic Scanning

The operation of the scanning probe microscope follows a defined sequence of preparation, cooldown, and measurement steps designed to ensure reproducibility and to protect sensitive quantum devices from damage. This section outlines the full experimental workflow, starting from sample and cantilever installation at RT, followed by system evacuation, precooling, and cooldown to cryogenic temperatures. It then describes the procedure for laser locking, mechanical approach, and frequency tracking, ending in the acquisition of spatially resolved data. Emphasis is placed on critical alignment and safety steps that ensure reproducibility and prevent damage to delicate quantum devices during operation.

A typical scanning routine begins with mounting the sample in the scanning probe head, followed by the installation of the AFM cantilever and alignment of the confocal objective onto the cantilever's backside. The cantilevers used in the probe have gold evaporated on the backside for better reflection. Using an optical microscope, the cantilever is coarsely aligned and approached to the sample surface. A temperature scan of the laser diode is done to identify a suitable interference fringe, and the laser is then locked to the side of a fringe with the integrated software of the digital laser controller. The mechanical resonance of the cantilever is then checked by applying a sinusoidal voltage to the actuator piezo and performing a frequency sweep to find its resonance frequency. The signal connections between the breakout boxes and external measurement instruments are established but kept grounded. Depending on the device on the cantilever and the sample, these configurations may vary significantly. Signals to be recorded during scanning are connected via BNC cables to the Nanonis system, enabling synchronized acquisition of AFM data and transport signals from the cantilever sensor and the sample. These initial steps are performed at RT with the can open.

Once functionality of all the mentioned steps is confirmed, the can is mounted, and the insert is evacuated to a pressure of approximately 10^{-6} mbar. The system is then precooled using LN_2 and subsequently transferred carefully into the cryostat for cooling to LHe temperature. During cooldown, the alignment of the laser is periodically readjusted to compensate for thermal contraction effects that otherwise cause the optical axis to shift relative to the cantilever.

Once the temperature measured at the scanning probe head drops below 5 K, typically after 12 h, the process of approaching the sample towards the cantilever tip is started. The interferometric readout is reoptimized by scanning and locking to a fringe again. A new frequency sweep is performed to determine resonance frequency, phase, and amplitude setpoints, which change with reduced temperature.

At this point a PLL is activated. The PLL continuously tracks the resonance frequency of the cantilever by adjusting the voltage signal sent to the actuator in real time to maintain a constant phase relationship between the drive and the cantilever response. This makes precise tracking of small shifts in the resonance frequency caused by tip-sample interactions during scanning possible.

Then the approaching procedure is started. The software begins by fully extending the z-scanner piezo, bringing the sample closer to the AFM tip. If no resonance frequency shift is detected, the piezo is retracted and the stepper motor moves the sample closer with a small number of coarse steps. This loop continues, alternating between piezo extension and steps, until a set frequency shift (here $-5\,\mathrm{Hz}$) is detected. This indicates a close proximity of the tip to the surface. During this process, a DC voltage of about $1\,\mathrm{V}$ is applied to a gate electrode on the cantilever. The resulting electrostatic tip-sample force makes the approach curve shallower, making the process more gradual and safer.

Once the desired approach is achieved, scanning parameters are configured. Scans are performed using a closed feedback loop that adjusts the z-piezo height to maintain a constant frequency shift. This feedback ensures that topographic variations on the sample are tracked accurately and that the sample does not crash into the tip. As RT optical alignment only provides rough orientation guidance, initial scans are used to identify the landing position on the sample. Lithographically defined alignment markers or distinct topographical features on the sample are used for spatial orientation. Successive 2D scans are taken while stepping towards the region of interest until the target area is reached. At this stage, the stepper motors for coarse positioning are no longer in use, and the sample and sensor can therefore be ungrounded.

It is important to note that the laser used for interferometric cantilever readout introduces significant noise in the charge sensor and the sample QD (see Figure 5.5d). To mitigate this, a constant frequency scan is first performed with the laser active for feedback. This gives a topographical image of the scanned area. The z-position of the piezo is then fixed to a certain extension, allowing the laser to be switched off during signal acquisition and different measurements may be performed without introducing optical noise into the charge sensor or the QD. The measurement procedures and corresponding results are discussed in Chapter 5.

Chapter 4

Functionalization of NC-AFM Cantilevers

This chapter explains how commercial NC-AFM cantilevers are converted into platforms that host nanoscale devices at the tip apex. It is organized as follows:

- Section 4.1 introduces the preparation of AFM levers, including the choice of suitable probes, the definition of a plateau at the tip by FIB milling, cleaning by CO_2 snow, ALD deposition of insulating oxide, and bonding pad fabrication.
- Section 4.2 presents resist-coating techniques, with a focus on the floating-PMMA transfer method adapted to cantilever geometry, enabling uniform coatings on sloped tips and compatibility with both positive- and negative-tone lithography.
- Section 4.3 details the fabrication of scanning multi-gate levers, describing the gold base metallization, EBL alignment strategy, development, pattern transfer by Ar ion beam etching, and electrical integration via wire bonding.
- Section 4.4 describes the fabrication of scanning NWQD levers, covering membrane-based nanowire device preparation, release and transfer to cantilever tips, final interconnect processing, and optimized annealing and testing protocols.

Together, these procedures establish a reproducible route to integrate multi-gate and NWQD sensors at the cantilever apex, providing the device platforms used in the subsequent measurement chapter.

4.1 AFM Lever Preparation

The integration of functional nanodevices at the apex of AFM cantilevers requires a sequence of preparatory steps to adapt commercially available probes into suitable fabrication platforms. Standard AFM levers are optimized for imaging performance, but not for subsequent nanofabrication. Their geometry, surface topography, and material composition introduce challenges for resist-coating, electrical isolation, and electrode patterning. In the following sections, the preparatory procedures applied to the AFM levers are described. These include the rationale for selecting specific commercial cantilevers, the focused ion beam (FIB) milling used to create a plateau at the tip, cleaning strategies to ensure oxide integrity, atomic layer deposition (ALD) of an insulating dielectric, and the definition of metallic bonding pads for electrical interfacing. Together, these steps establish a reproducible platform on which more complex nanostructures, such as multi-gate electrodes or NWQDs, can be fabricated in later stages.

4.1.1 Commercial AFM Lever Selection

The first step in preparing AFM levers for device fabrication is the choice of a suitable cantilever. Since the mechanical properties, tip geometry, and surface topography critically determine the feasibility of subsequent nanofabrication, different probe types were evaluated.

For this work, it is chosen to base the devices on commercially available AFM cantilevers in order to ensure reproducibility and to avoid the complexity of in-house cantilever fabrication. Specifically, NC Advanced Tip at the End of the Cantilever (ATEC)[1] are employed, which are designed for NC-AFM operation. NC-mode is essential for the present application, since direct tip-sample contact would risk damaging the fragile nanodevice fabricated on the cantilever tip.

A key requirement for stable NC operation is a relatively stiff cantilever, which suppresses snap-in. The NC-ATEC meets these criteria with a nominal spring constant of $\sim$45 N/m. Their resonance frequencies lie in the range of 210-490 kHz and their quality factor Q is >5000. The cantilever dimensions are 150-170 µm in length, 40-50 µm in width, and 3.6-5.6 µm in thickness. The NC-ATEC probes feature tips with a nominal height of 15-20 µm and the cantilevers are fabricated from highly doped silicon, intended to dissipate static charge. Their geometry is advantageous for subsequent nanofabrication. The cantilever body and lever are free of prominent surface structures, facilitating uniform resist-coating, while the tip emerges smoothly from the cantilever. The tip itself is formed by anisotropic

[1] ATEC-NC, Nanosensors

silicon etching, resulting in a slope of 54.7°. This produces a pyramidal profile that is wide at the base and tapers towards the apex (see Figure 4.1d). Such a geometry is particularly suitable for the present purpose, as sufficient area along the incline is available for the deposition and patterning of metallic electrodes that extend towards the tip.

In addition to the NC-ATEC probes, other alternatives were evaluated. Probes from NuNano[2] with conical tips were tested, but the tip geometry proved unsuitable for the lithography used, since the slope becomes too steep at the top of the tip and their lever bodies exhibited significant topographic variation, complicating resist-coating and subsequent processing. Further, custom-fabricated levers from IBM which are provided with pre-patterned Au bonding pads, were tested. While attractive in principle, these probes exhibit leakage across the front of the lever and have a flat tip geometry, increasing the risk of snap-in during tip-sample approach. Tip-less levers[3] from other suppliers were also investigated. Although the topography on the body exhibits some variation, uniform resist coating is still achievable. Nevertheless, given the absence of a tip, reliable scanning performance could not be assured, for example because the likelihood of snap-in may be increased, and these probes were therefore not pursued further. Based on these experiences, the NC-ATEC offers the most favorable balance between mechanical properties, tip geometry, and surface morphology, and is therefore adopted as the standard platform for the scanning probe charge and multi-gate sensors.

While the NC-ATEC provides the most suitable platform, their as-supplied pyramidal tips do not offer the flat surface required for device integration. Therefore, the next step is to define a plateau at the tip apex using FIB milling.

4.1.2 FIB Plateau Definition

To integrate the sensor as close as possible to the sample, it is fabricated directly at the apex of the AFM tip. For this purpose, a flat plateau is defined at the end of the tip to serve as the substrate for subsequent nanofabrication (see Figure 4.1). This modification is performed using a Ga^+ FIB[4].

The as-supplied silicon tip has a pyramidal geometry with a slope of 54.7°. Such a steep slope complicates resist processing, in particular metal lift-off, as discussed in our work. [93] To address this issue, the slope angle is reduced to approximately 20° by controlled ion milling, producing a more gradual slope that facilitates reliable lithography. However, it is seen that for tips with a height of less than 5 µm,

[2]Scout 350, NuNano
[3]TL-NCH, Nanosensors
[4]FIB, FEI Helios NanoLab 650

slope reduction is not required. The original etched slope is sufficient and provides superior smoothness compared to the milled surface. This insight reduces fabrication time and improves reproducibility, as slope adjustment is time-consuming and cannot achieve the crystalline quality of the etched sidewalls.

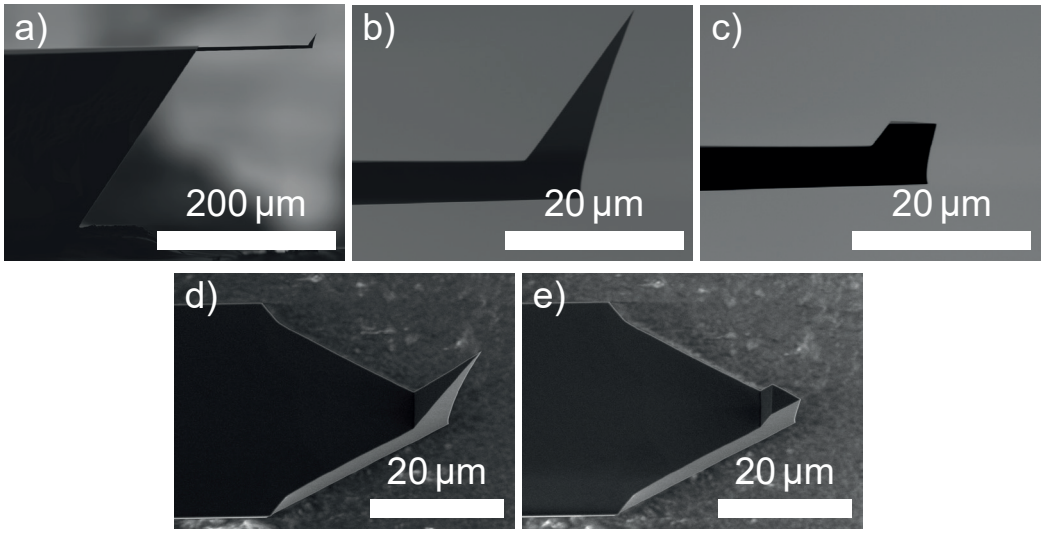

Figure 4.1: NC-ATEC cantilever before and after FIB milling of a tip plateau. **a)** FIB side-view overview: the lever body is visible on the left and the cantilever with its pyramidal tip on the right. **b)** FIB magnified side view of the pristine tip, showing the anisotropic-etch slope of 54.7°. **c)** FIB side view after milling, revealing a planar plateau at the apex and a reduced height that facilitates subsequent lithography. **d)** SEM oblique view of the pristine tip, corroborating the geometry observed in b). **e)** SEM oblique view after plateau definition, highlighting the lateral extent and surface quality of the milled plateau. Images are representative of the procedure described in Section 4.1.2.

The plateau is defined by Ga^+ milling at 30 keV. The beam current is adjusted depending on the milling step: higher current for rapid material removal during coarse shaping and lower current for fine polishing of the plateau surface. The exact choice of current also depends on the vacuum conditions of the FIB system, since higher currents can be employed under more stable vacuum operation without sacrificing milling quality. The process is monitored and pre-aligned using the scanning electron microscope (SEM) column of the dual-beam system, while material removal is performed exclusively with the ion beam.

As a consequence of FIB milling, Ga^+ implantation into the silicon tip is unavoidable. [94, 95] In this case, this does not compromise device insulation, since

the entire cantilever is subsequently covered with an ALD oxide layer. Nevertheless, Ga^+ implantation-related effect may contribute to charge noise in the final device. [46, 96] Given the available instrumentation, however, Ga^+ FIB milling provides the only viable approach for plateau definition.

The resulting modification produces a triangular flat surface at the tip apex. The lateral dimensions of the plateau are tailored depending on the intended device: smaller plateaus of approximately 4 µm are used for multi-gate levers, while larger plateaus are prepared for QD sensor devices. Representative micrographs of the ATEC before and after FIB milling are shown in Figure 4.1b and d and the plateau created by ion milling in Figure 4.1c and e. Before dielectric deposition, the modified levers require thorough cleaning to remove redeposited fragments and handling-induced contaminants.

4.1.3 Cleaning

During manipulation of the cantilevers with tweezers, small fragments from the sharp edges of the cantilever body can detach and redeposit on the cantilever surface. Such contaminants interfere with ALD films and may lead to dielectric failure, resulting in leakage pathways between electrodes. To avoid this, a CO_2 snow cleaning procedure is employed.

In this method, high-purity compressed CO_2 is expanded through a nozzle[5] to form a high-velocity jet of solid-gas mixture, commonly referred to as a CO_2 snow stream. This stream efficiently removes both particles and thin surface films from silicon substrates without leaving detectable residues. [97] For cleaning, the cantilevers are mounted on an aluminum plate using double-sided Kapton tape. The devices are secured from the back to prevent displacement by the CO_2 stream and to keep the top surface unobstructed. The plate is placed on a hot plate at 150 °C to prevent condensation of ambient moisture during cleaning, which otherwise leads to freezing and water stains on the cantilevers. A continuous flow of dry nitrogen is simultaneously directed over the plate to further suppress adsorption of water vapor.

The CO_2 nozzle is aligned such that the stream is directed from the tip of the cantilever towards the body, preventing dislodged particles from being driven into the sensitive tip region. The nozzle-sample distance is optimized using dummy cantilevers to determine the closest approach that removes contamination without damaging the cantilever. After cleaning, the aluminum plate with cantilevers is immediately transferred into the ALD chamber to minimize recontamination. This

[5] K1-10 Unite, Applied Surface Technologies

procedure significantly reduces the occurrence of leakage between electrodes in subsequent devices.

4.1.4 Oxide Deposition by ALD

To electrically isolate subsequently fabricated electrodes from the highly doped silicon substrate of the cantilever, a conformal dielectric layer is deposited onto the cantilevers. For this purpose, ALD is chosen. Unlike other thin-film deposition techniques such as chemical vapor deposition (CVD) or physical vapor deposition (PVD), which may produce non-uniform coatings on 3D structures, ALD proceeds through sequential, self-limiting surface reactions of alternating precursors. [98] This mechanism allows films to grow layer-by-layer with angstrom-level thickness control, while ensuring excellent conformability and coverage even on complex geometries such as AFM cantilever tips. [98] These properties make ALD particularly suitable for the present application, where reliable insulation of electrodes on steep and irregular surfaces is key.

Among the dielectric materials available in the in-house ALD system[6], aluminum oxide (Al_2O_3) and hafnium oxide (HfO_2) are considered. While HfO_2 offers a higher dielectric constant, initial trials with it did not deliver reproducible results under the conditions available. Al_2O_3 is therefore chosen because it provides more reproducible results and superior reliability in terms of leakage suppression on the cantilever geometry.

After the cleaning step, the cantilevers are transferred into the ALD system for oxide deposition. Al_2O_3 is deposited using trimethylaluminum (TMA) and water (H_2O) as precursors, with a deposition temperature of 200 °C. The precursor pulse time for both TMA and H_2O is 0.007 s. A total of 600 ALD cycles are performed, corresponding to an oxide thickness of approximately 66 nm. The resulting Al_2O_3 layer encapsulates the entire cantilever, except for the region in contact with the Kapton tape used to mount the levers during processing. As in the cleaning step, the cantilevers are secured from the back to prevent displacement by precursor pulses and to keep the tip surface unobstructed.

4.1.5 Bonding Pad Fabrication

Following the deposition of the insulating oxide layer, bonding pads are fabricated on the cantilevers. Unlike in conventional nanofabrication, where small features are typically defined first and larger contact structures are added in subsequent steps, the order is reversed here. Bonding pads are fabricated at an early stage for

[6]Savannah S100 ALD, Cambridge Nanotech

two reasons. First, the pads allow an immediate test for electrical leakage through the oxide, enabling the selection of suitable cantilevers before undertaking the more time-consuming steps of device fabrication. Second, the alignment precision available in this step is insufficient for reliably contacting fine electrode lines extending from the tip region. Pads therefore have to be fabricated independently and prior to the definition of smaller features.

In addition to mounting the cantilever at an incidence angle of 10° relative to the sample, it is further essential that the bonding pads are placed as far as possible towards the rear end of the cantilever body. This placement minimizes the risk that wire bonds protrude into the sample region and interfere mechanically with the scanning probe experiments before the tip itself engages with the sample.

Lithography on AFM cantilevers is particularly challenging due to their 3D geometry, as will be discussed in detail in Section 4.2. In principle, electron-beam lithography (EBL) could be employed to define bonding pads, but this approach would require large-area, uniform resist-coating and long writing times. Instead, a more practical method is implemented using silicon shadow masks. These masks are fabricated by collaborators[7] using deep reactive ion etching with the Bosch process (detailed recipe in Appendix A.4). The Bosch process is used as it enables deep, high-aspect ratio etching of silicon with nearly vertical sidewalls. [99] Each mask contains five rectangular openings corresponding to bonding pads, as well as connecting lines extending towards the front of the cantilever body.

For deposition, the cantilevers are mounted in a custom-built holder designed to clamp the lever securely without covering the main part of the body. The silicon shadow mask is positioned above the lever, and a coarse alignment of the mask to the cantilever is performed under an optical microscope. Metal deposition is carried out in an electron-beam (e-beam) evaporator[8]. In this process, a focused e-beam is scanned across a crucible containing the source material, causing localized heating and evaporation. The evaporated atoms travel ballistically in high vacuum and condense on the sample surface. To ensure uniform coverage, the sample stage is continuously rotated during deposition. A stack of Ti (5 nm)/Au (120 nm)/Ti (5 nm) is deposited. The bottom Ti layer serves as an adhesion promoter between Au and the Al_2O_3 surface. Au provides the main conducting layer of the pads, while the top Ti layer acts as a protective cap. This final layer is particularly important for cantilevers later used in multi-gate sensor fabrication, where etching steps would otherwise damage the bonding pads.

After deposition, the cantilevers are removed from the holder and electrically tested

[7]Fabio Bersano, NanoLab, EPFL
[8]MEB550S, Plassys Bestek

at RT using a needle probe station. Leakage between bonding pads is checked, and only cantilevers without detectable leakage are selected for further device processing. Cantilevers exhibiting leakage are discarded at this stage.

With the bonding pads in place and verified for electrical integrity, the cantilevers provide a reliable platform for subsequent device processing. A representative optical image of a prepared cantilever is shown in Figure 4.2. The next crucial step is the development of a suitable resist-coating strategy, which is particularly challenging on the 3D geometry of AFM cantilevers and is therefore discussed in detail in Section 4.2.

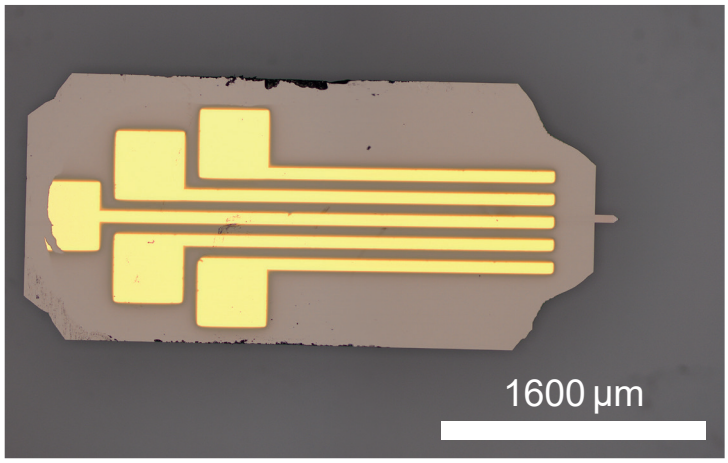

Figure 4.2: Optical image of an NC-ATEC cantilever platform prepared for subsequent device processing. The cantilever incorporates a cut plateau at the tip apex (not visible at this magnification), a conformal Al_2O_3 insulating layer, and Ti/Au/Ti bonding pads with lines extending toward the front of the body. Small edge defects are visible near the middle of the lever body originating from mechanical handling with tweezers.

4.2 Resist-Coating Techniques

EBL is a widely used technique for fabricating nanoscale structures such as gate electrodes. With modern instrumentation, EBL routinely achieves feature sizes on the order of 10 nm [100], while also enabling batch fabrication and the use of standardized process recipes. This makes it a flexible and high-yield technique for device prototyping. In a typical process, a planar substrate is spin-coated with an e-beam resist, which is then selectively exposed to electrons, developed, and further processed.

However, conventional spin coating becomes problematic for small or non-planar substrates. Effects such as edge beading, imperfect pattern transfer, and poor lift-off performance often result in non-uniform resist layers and reduced device yield. [93] Nevertheless, there are many applications where EBL on irregular substrates would be highly desirable.

Alternative approaches to resist-coating have been reported, including spray coating [101], the use of ice resists [102], evaporative methods [103], and resist transfer techniques. [104–106] Other strategies involve direct focused-ion or e-beam deposition [107] and milling. While these methods can be effective in specific cases, they are either slow, expensive, only demonstrated for photoresists, or not tailored toward patterning on fragile substrates, such as scanning probe microscopy cantilevers, which are vulnerable, suspended structures, which typically are 100 µm in length and a few micrometers in width and thickness.

To address this challenge, a new resist-coating method is developed as part of this work and published in [93]. The technique builds on concepts originally used for resist transfer onto exfoliated flakes of 2D materials [108] and adapts them to suspended AFM cantilevers. Compared to the version published in [93], several modifications are later introduced to improve fabrication yield and reproducibility, as described in the following paragraphs.

4.2.1 Floating-PMMA

To enable uniform, controllable resist coverage on suspended cantilevers, a floating-PMMA transfer is implemented. A polymethylmethacrylate (PMMA) film is formed on a sacrificial dextran layer, released to float on water, and then gently laminated onto the cantilever, yielding smooth, conformal coatings over the tip apex with minimal handling. The protocol used here follows the published concept but adds cleanliness and alignment refinements to improve yield on fragile levers, as detailed below.

First, a sacrificial film is prepared by spin coating a glass slide with a 15 % solution of dextran in deionized (DI) water at 2000 rpm for 40 s. The slide is then baked at 150 °C for 3 min to remove residual solvent. On top of this sacrificial dextran film, the desired resist is spin coated. Various PMMA-based resists were tested and found to be compatible with the method. An overview of the floating-PMMA process to coat a cantilever, is illustrated in Figure 4.3.

For the demonstration structures shown in Figure 4.4 and 4.5, a solution of 4.5 % PMMA[9] is spin coated at 4000 rpm for 40 s and baked at 150 °C for 3 min, yielding

[9] AR-P 672.045 950k, Allresist

a resist thickness of approximately 230 nm. The PMMA/dextran stack is then sectioned into ∼10x10 mm^2 pieces with a razor blade and immersed in fresh DI water for ∼10 min to dissolve the dextran film (longer times required for thicker resist). To initiate detachment, the slide is briefly withdrawn, tilted at a small angle, and slowly reinserted into the water. The PMMA film detaches from the glass and floats at the water surface. Up to this point, the procedure followed Reference [93].

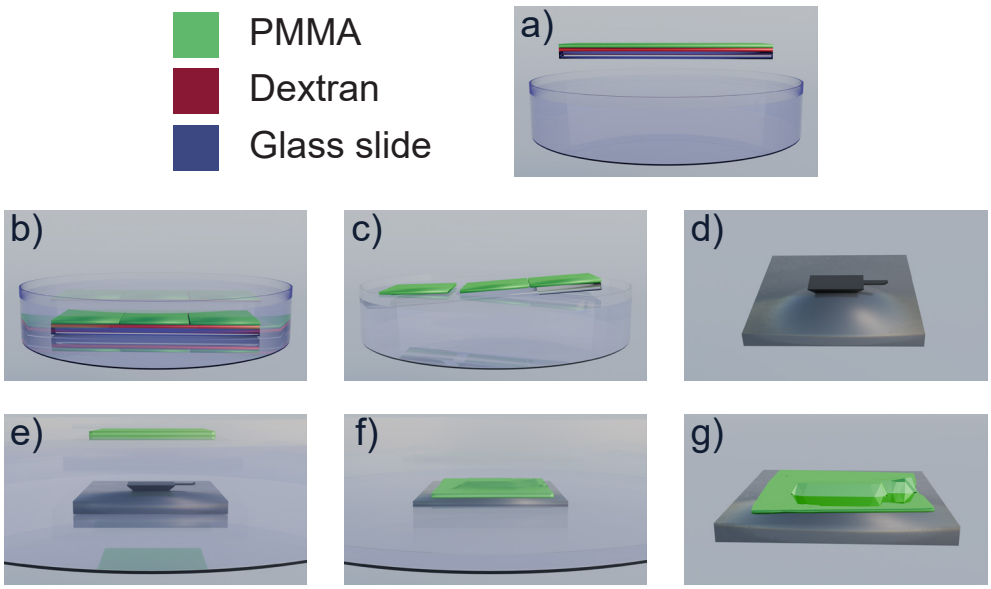

Figure 4.3: Overview of the floating-PMMA resist-coating process (not to scale). a-c Preparation of a floating-PMMA layer. **a)** A glass slide is spin-coated with dextran and PMMA, **b)** immersed in DI water, and **c)** reinserted at an angle to release the floating-film. d-g Transfer onto a cantilever, **d)** the cantilever is mounted on a metal support, **e)** immersed in DI water, **f)** coated as the water is drained. **g)** After drying and baking, a uniform PMMA layer is obtained. Adapted from [93] with permission.

For transfer onto cantilevers, several modifications are introduced to improve yield and cleanliness. The cantilevers are clamped to a metal holder using an uncoated metal rod secured with two screws. This approach replaces Kapton tape, which is found to leave contamination on the cantilevers after subsequent solvent treatments. Rather than lowering the cantilever upside down into the floating resist, the transfer is performed in a separate petri dish filled with DI water. The metal holder with the cantilever is submerged in the DI water. A piece of floating-PMMA is transferred into the petri dish using a plastic spoon and positioned under the

optical microscope micromanipulator. Its location is stabilized with a glass needle mounted on a micromanipulator arm. A small outlet at the bottom of the petri dish is then used to gradually lower the water level. As the level decreases, the PMMA film gently settles onto the cantilever. The glass needle height is adjusted continuously to suppress lateral drift, and the process is monitored in real time through the microscope.

After the water has fully drained, the cantilever is removed from the petri dish. Residual water is removed using a tissue, the sample is rested, and then baked at 150 °C for 2 min. This procedure yields a uniform PMMA coating with minimal wrinkles. The method combines the uniform resist thickness from spin coating with the versatility of resist transfer, making it applicable to non-planar and fragile substrates such as AFM cantilevers.

When coating cantilevers carrying pre-fabricated NW devices at the tip (as described in Section 4.4.3), the final drying step is modified to avoid mechanical disturbance of the device. In such cases, no tissue is applied to remove residual water. Instead, the sample is left to dry in vacuum for at least 1 h, after which it is baked at 150 °C for 2 min.

Additional tests with photoresist[10] demonstrate that the floating-layer method is not generally applicable to all resist types. Under otherwise identical conditions, the photoresist fragments upon contact with water into many small pieces rather than remaining as a continuous sheet. As a result, only PMMA-based resists are found to be compatible with this technique.

To demonstrate the potential of the floating-PMMA method, representative test structures are fabricated on cantilevers using both positive- and negative-tone lithography. For the positive-tone (lift-off) process, the tip slope is reduced by FIB milling to facilitate lift-off, and Ti/Pd is employed as metallization to improve process yield. In this configuration, a gate array with widths of approximately 350 nm and a pitch of 400 nm is obtained on sloped ATEC (Figure 4.4b). On a flat cantilever provided by IBM, the same process achieved gate dimensions down to 70 nm width and 90 nm pitch (Figure 4.4a). For the negative-tone (etch) process, the original pyramidal slope of the ATEC is retained. Here, the same PMMA resist is used in a negative-tone process by applying a sufficiently high e-beam dose [109], after which the cross-linked PMMA serves as a robust etch mask, enabling the definition of five narrow gates with widths of approximately 100 nm and pitch of 180 nm (Figure 4.5). In subsequent work, optimized fabrication yields gate widths below 50 nm and pitches below 100 nm. [110]

[10] S1805 Photoresist, Microposit

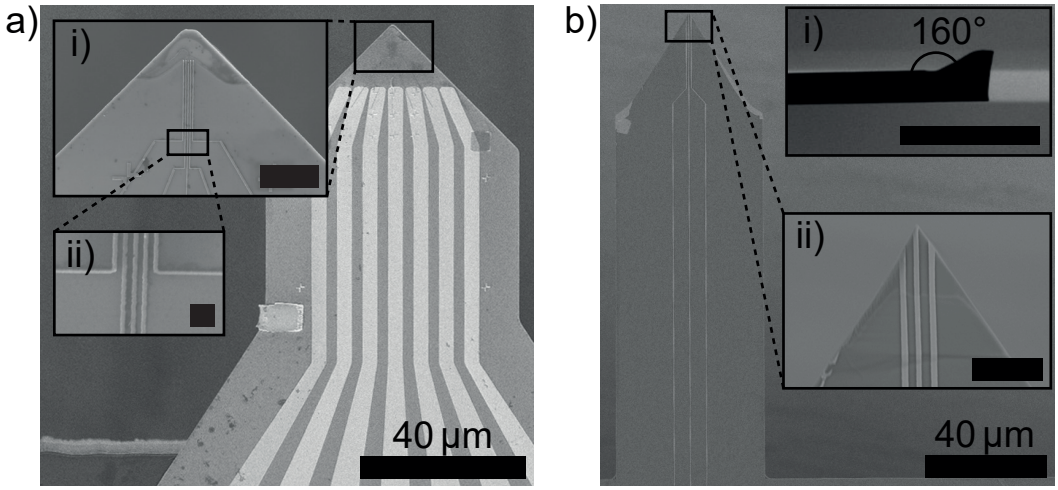

Figure 4.4: Scanning electron micrographs of AFM cantilevers patterned using the floating-PMMA method. **a)** Flat cantilever with seven large Au gates connected to five finer Ti/Pd gates at the front. Inset: **i)** magnified view of the gates array near the tip (scale bar: 4 µm), **ii)** further zoom of the boxed region in i), showing individual gates in detail (scale bar: 400 nm). **b)** Tipped cantilever with three Ti/Pd gates. Inset: **i)** magnified view of the tip region with the measured 160° opening angle indicated (scale bar: 20 µm), **ii)** SEM side view of the tip apex (scale bar: 4 µm). Adapted from [93] with permission.

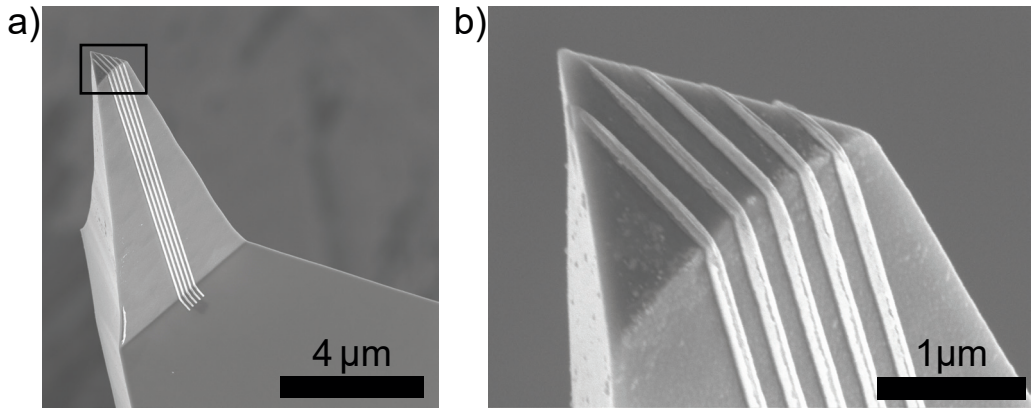

Figure 4.5: Scanning electron micrograph of AFM cantilever tip patterned with a gate array using the negative-tone process. The PMMA resist was cross-linked by high e-beam dose and subsequently used as an etch mask during ion-beam etching. **a)** Overview of the cantilever tip with the gate array. **b)** Magnified view showing individual gate width of ∼100 nm and a pitch of ∼180 nm. These demonstration structures illustrate the versatility of the floating-PMMA method. Adapted from [93] with permission.

4.3 Fabrication of Scanning Multi-Gate Lever

As introduced in Section 2.6, the aim is to integrate multiple independent gate electrodes at the tip of a NC-AFM cantilever. Compared to standard SGM, this configuration allows simultaneous control of several gates and, as proposed by Shim et al. [71], could enable the non-destructive characterization of semiconductor wafers by locally inducing QDs in the material system of interest. To realize such devices, a dedicated fabrication procedure is developed and presented in the following section.

The starting substrates are ATEC, prepared as described in Section 4.1, comprising a tip plateau defined by FIB milling, a conformal Al_2O_3 insulating layer, and five Ti/Au/Ti bonding pads with lines extending towards the front of the cantilever body. An overview of the multi-gate lever fabrication process is shown in Figure 4.6. With the prepared cantilever as a starting platform, fabrication proceeds by depositing a continuous Au base layer, as detailed next.

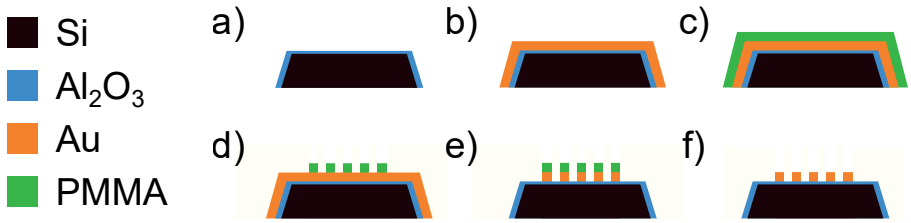

Figure 4.6: Process flow for the fabrication of multi-gate AFM lever (front view of the tip region, not to scale). **a)** Prepared ATEC featuring a FIB-defined plateau, conformal Al_2O_3 insulation, and rear bonding pads (not shown). **b)** E-beam evaporation of 20 nm Au base layer. **c)** Application of PMMA resist by the floating-PMMA method. **d)** EBL of the gate pattern followed by development, leaving the cross-linked PMMA as negative-tone etch mask. **e)** Pattern transfer into the Au by Ar ion-beam etching. **f)** Resist removal by O_2 plasma descum, yielding five electrically isolated gate electrodes on the plateau. Adapted from [93] with permission.

4.3.1 Gold Base Layer Deposition

To provide a conductive base layer connecting the bonding pads to the tip region, a 20 nm Au film is deposited on the front part of the cantilever. The deposition is performed using the same custom-built holder as for the bonding pads (see Section 4.1.5), but with a different shadow mask consisting of a titanium plate with one opening. The evaporation is carried out in an e-beam evaporator[8] with the sample mounted on a rotating stage to ensure uniform coverage of the slope and

the plateau region. Although the bonding pads consist of a 5/120/5 nm Ti/Au/Ti trilayer, the additional 20 nm Au does not compromise electrical connections as the height step is not critical for contacting due to the gradual thickness profile of the bonding pads introduced by the shadow mask evaporation. With the conductive base in place, the cantilever is next prepared for lithographic definition by applying a uniform resist coating.

4.3.2 Resist-Coating

Following base metallization, the cantilever is mounted on a metal piece using the method described in Section 4.2 and coated with PMMA by the floating-layer technique (Figure 4.3). A resist with 200 k molecular weight[11] is spin coated at 4000 rpm for 40 s and baked at 150 °C for 2 min, yielding a resist thickness of approximately 120 nm. A 200 k resist is chosen instead of the commonly used 950 k PMMA[9] because the electron dose required to cross-link the resist is lower, reducing the total writing time and thereby mitigating the impact of beam and stage drift during long exposures. Moreover, preliminary tests indicated improved reproducibility with the 200 k variant. After coating, the resist uniformity is checked by optical microscopy, and images of the cantilever are acquired to be used for design alignment.

After coating, gold nanoparticles[12] are deposited at the corners of the cantilever body to provide high-contrast focusing targets on the PMMA. The cantilevers are then ready for e-beam lithography to define the gate structures.

4.3.3 Electron-Beam Lithography

With the resist in place, the gate pattern is written by EBL. The gate design is adapted to the individual cantilever geometry based on the acquired optical images. To balance resolution requirements and writing time, the EBL exposure is divided into writing steps with different aperture and dose. The five gates at the tip plateau (see Figure 4.7b) are written with the 7.5 µm aperture and dose 140 000 µC/cm^2, the connecting lines on the plateau with the 20 µm aperture and dose 40 000 µC/cm^2, the broader leads extending towards the cantilever body with the 60 µm aperture (dose 40 000 µC/cm^2), and the connections to the bonding pads with the 120 µm aperture (dose 40 000 µC/cm^2). This strategy enables high precision in the critical tip region while maintaining acceptable writing times further back on the lever.

For alignment, prominent cantilever features are used. The corners of the cantilever

[11] AR-P 672.04 200k, Allresist
[12] 100 nm diameter OD 1 suspension in citrate buffer Gold NP, Sigma-Aldrich

serve as general alignment marks, while the tip apex is employed as an additional reference for the critical writing of the five gates on the plateau. Relying solely on the cantilever corners is found to result in misalignment at the tip, making the additional use of the tip apex essential for accurate gate placement.

Exposures are carried out in a SEM[13] equipped with a EBL system[14]. A custom-written script controls the entire lithography process. A three-point alignment using the deposited gold nanoparticles to define the focus plane across the cantilever is performed. This ensures uniform focusing despite the cantilever's slight tilt and topographic variation. Additionally, an angle alignment is carried out to establish the horizontal axis of the cantilever relative to the writing field. Afterward, the stage is positioned at the lower left corner of the cantilever, and the automated script executes all subsequent steps. This includes stage movements, alignment routines for each aperture, and the writing process itself. The only user input required is to specify the positions of the alignment features from SEM images. This automation minimizes the impact of operator error, while ensuring consistent dose control across all writing steps. Following exposure, the patterned resist is developed and inspected to verify correct alignment and feature integrity.

4.3.4 Development and Inspection

Development is done in acetone (ACE) for 3 min, rinsed in isopropanol (IPA) for 1 min, and dried with N_2. During development, ACE and IPA are dispensed with a pipette to flush the cantilever, particularly the tip region, which significantly improves the pattern quality and reduces resist residues. The resulting pattern leaves cross-linked PMMA in the exposed regions, serving as a negative-tone etch mask. The alignment of the resist mask is checked in the SEM. Unlike conventional positive-tone processes, the cross-linked PMMA [109] is sufficiently stable under the e-beam to allow imaging without destroying the pattern. After confirming the resist mask, the pattern is transferred into the Au base described in the next section.

4.3.5 Ion Beam Etching and Resist Removal

Pattern transfer is performed by Ar ion-beam etching (IBE) in the Plassys[8] system with the following parameters: 500 V acceleration voltage, 100 V extraction voltage, 20 mA beam current, and 8 sccm Ar flow. During etching, the sample stage is rotated and tilted by 10° relative to the ion beam, which substantially improves etch uniformity across the lever. A typical etching time of 3 min is used, followed

[13]Supra 35 SEM system, Zeiss
[14]EBL Elphy Plus, Raith

by SEM inspection to verify removal of Au in unprotected areas, with particular attention to the slope and plateau. If residual Au is observed, additional etching cycles are performed. Finally, the remaining PMMA is removed by oxygen plasma ashing using a reactive-ion etcher[15] (RIE) (6 min, O_2 20 sccm, 60 W). This sequence yields cantilevers with five independent gate electrodes aligned on the tip plateau, as illustrated in Figure 4.7.

Following fabrication, the backside of the lever is coated with 20 nm of Au in order to increase beam reflectance for better readout of the cantilever motion. The lever is mounted onto the cantilever holder described in Section 3.3.1. Electrical connection between the cantilever bonding pads and the PCB is established using a wire-bonder[16] with aluminum wire. Particular care is taken to minimize the loop height of the bonding wires, since excessive wire protrusion can result in the bond touching the sample surface before the cantilever tip makes contact. Such premature contact would risk damaging either the sample or the sensor.

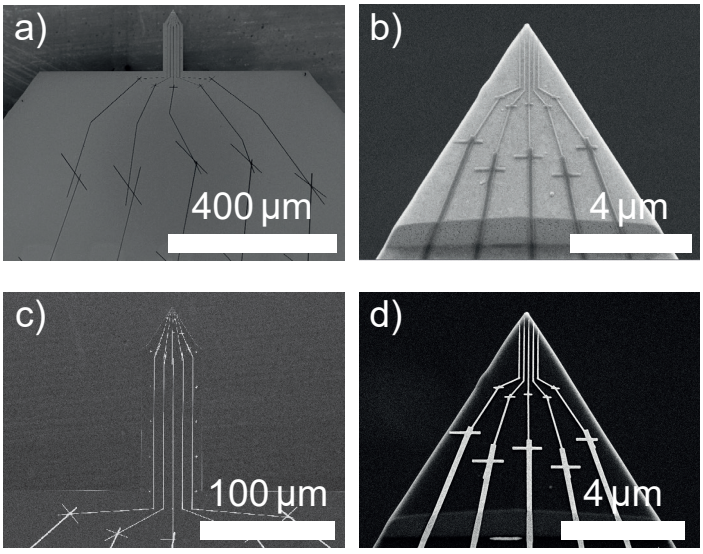

Figure 4.7: Scanning electron micrograph of AFM cantilevers during and after negative-tone patterning. **a)**, **b)** Cantilevers coated with a thin Au base layer and patterned with high-dose PMMA resist, which after exposure remains as a cross-linked mask. **c)**, **d)** Final structures after pattern transfer by Ar IBE and resist removal by RIE.

[15]Plasma Pro 80 RIE, Oxford Instruments
[16]Series 56i, F&S Bondtec

4.4 Fabrication of Scanning NWQD Lever

To realize a QD charge sensor on the apex of an AFM cantilever, one possibility is to integrate a semiconductor NW with intrinsic tunnel barriers. In this geometry, only a source, drain, and plunger gate are required for device operation (see Section 2.1). InAs NWs incorporating InP tunnel barriers are chosen for this purpose, motivated both by promising results reported in literature [19] and by their availability within the department. Such heterostructures provide strong and reproducible confinement due to the large conduction-band offset between InAs and InP ($V_0 \sim$ 400-600 meV). [111, 112]

The InAs/InP NW heterostructure QDs are grown by gold-assisted chemical beam epitaxy. [113] The wires have a diameter of 50±5 nm, set by the size of the Au seed particles. A typical dot consists of an InAs segment of ∼19 nm in length, bound by two InP barriers of ∼5 nm thickness. The QD is positioned approximately 450 nm from the Au seed end of the NW. Similar structures have been successfully employed for single [114–116] and double QD devices [117, 118].

With the heterostructure and target device architecture defined, the practical task of transferring and positioning a single NW at the cantilever apex needs to be addressed. The transfer strategy is detailed in the following section.

4.4.1 Transfer Strategies for NW to Cantilever Tips

Several approaches were explored to position NWs directly on the cantilever plateau. Using a micromanipulator[17] in a SEM, individual NWs could be transferred with reasonable accuracy. However, this approach requires exposing the wires to the e-beam for 20-30 min, which is found to degrade device performance. In separate test samples, Coulomb oscillations measured before and after prolonged e-beam exposure disappeared after 30 min irradiation, indicating damage to the NW.

An alternative strategy involves AFM-based pick-up [119, 120], where the cantilever tip is scanned across a substrate until contact is made with an individual NW. This succeeds occasionally, but the reproducibility is very poor. Furthermore, when such cantilevers are subsequently coated using the floating-PMMA method, the NWs are consistently dislodged from the plateau.

To overcome these challenges, an alternative concept is pursued. Instead of transferring bare NWs, complete NW devices are fabricated on thin SiN_x membranes, which are subsequently released and transferred to the cantilever tip. This approach offers several advantages. First, the larger membrane structures are better visible

[17] MM3A-EM micromanipulator, Kleindiek Nanotechnik

under an optical microscope, facilitating alignment and manipulation. Second, the NW devices can be fabricated in a planar geometry using established EBL methods prior to transfer. Finally, the adhesion of the larger membrane structures to the tip is superior, increasing robustness during subsequent floating-PMMA coating steps. Moreover, this route enables the fabrication and transfer of diverse device architectures to the AFM tip, making the method highly versatile.

In the following section, the fabrication of these suspended SiN_x membranes is described.

4.4.2 Fabrication of SiN_x Membranes

Suspended SiN_x membranes serve as carrier platforms for the transferable NW device. A schematic of the fabrication process can be seen in Figure 4.8.

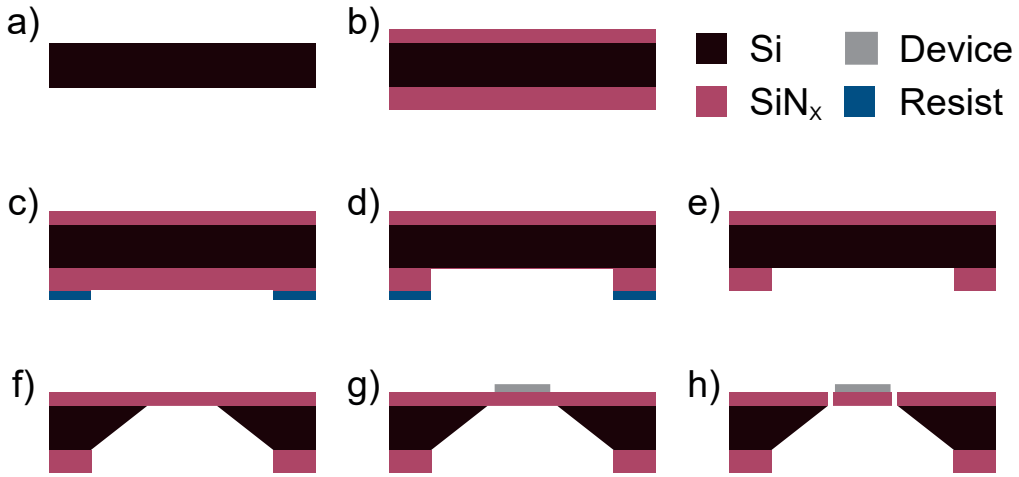

Figure 4.8: Schematic of SiN_x membrane fabrication. **a)** Double-side polished Si ⟨100⟩ wafer, **b)** PECVD SiN_x deposition: 300 nm on backside and 50 nm on frontside. **c)** Square windows ($400\times400\,\mu m^2$) patterned on the backside SiN_x by photolithography. **d)** Backside SiN_x opened by CHF_3/O_2 RIE[15]. **e)** Photoresist stripping in O_2 plasma. **f)** KOH wet etch of Si to form suspended 50 nm thick SiN_x membranes. **g)** Device fabrication on the membrane. **h)** Membrane release into triangular transfer shape.

Starting substrate is a double-side polished Si wafer[18]. A 300 nm SiN_x layer is deposited on the backside and a 50 nm layer on the frontside by PECVD[19]. Square windows ($400\times400\,\mu m^2$) are defined on the backside SiN_x by photolithography using a S1805 resist[10] (spin coating at 4500 rpm, 45 s, baked 125 °C for 2 min) and exposed in a laser writer[20]. The resist is developed[21] for 1 min, rinsed in DI water, and dried with N_2. The backside SiN_x is then etched by CHF_3/O_2 RIE[15] (16 min, O_2 5 sccm , CHF_3 50 sccm, 150 W), followed by resist removal in O_2 plasma (10 min, O_2 20 sccm, 60 W). A second O_2 plasma clean is performed on the frontside to clean residual resist. The underlying Si is subsequently etched in a 33 % KOH solution at 87 °C for ∼3 h, yielding suspended SiN_x membranes of thickness 50 nm and lateral dimensions of $\sim50\times50\,\mu m^2$. An optical image of the resulting membrane can be seen in Figure 4.10b.

With suspended membranes available, the next step is to fabricate NW devices directly on these supports.

4.4.3 NW Device Fabrication on Membranes

On the suspended SiN_x membranes, alignment markers (5 nm Ti / 20 nm Au) are first defined by EBL and evaporated. NWs are then transferred to the membranes using a glass needle in a micromanipulator setup, with subsequent SEM imaging to define contact designs.

Standard EBL with PMMA resist[9] (spin coating at 4000 rpm, 40 s, baking at 150 °C for 2 min, thickness ∼230 nm) is used to pattern source, drain and plunger electrodes. After development (1 min in AR-600-55[22], 1 min IPA) O_2 plasma descum[23] (20 s, O_2 8.3 sccm, 30 W) ensures resist-free contact areas. Metal deposition is performed in an e-beam evaporator[8] equipped with in-situ Ar IBE to remove the native NW oxide. The sequence is Ar IBE (35 s, 250/50 V, 8 mA), followed by 5 nm of Ti and 65 nm of Au evaporation while the sample stage is rotating to achieve more uniform etching and evaporation. Lift-off is performed in ACE at 50 °C for 15 min with pipette agitation.

Alternative contact schemes were also explored. Sulfur passivation [121] prior to metallization provides limited reproducibility, whereas in-situ Ar IBE yields more reliable low-resistance contacts. In later optimization, Ti/Pd/Au (5 nm/20 nm/50 nm)

[18]DSP Si wafer, diameter 50.8 mm, thickness 280 µm, orientation ⟨100⟩, undoped
[19]PECVD silicon nitride is referred to as SiN_x to reflect non-stoichiometric composition.
[20]uPG 101 Laser Writer, Heidelberg Instruments
[21]MF-319, Microposit
[22]Developer AR 600-55, Allresist
[23]ATTO Plasmacleaner, Diener Electronic

trilayers are employed. The inclusion of Pd [122] or Pt [123] interlayers is known to suppress the penetration of Au atoms into the underlying semiconductor during annealing, thereby acting as an effective diffusion barrier. Diffusion of Au into InAs NW is considered to be a possible source for the increased noise observed after prolonged annealing. To the best of our knowledge, no direct literature evidence confirms this mechanism in InAs NWs. However, multiple annealing cycles (described in Section 4.4.6) of Ti/Pd/Au contacted InAs/InP NW are performed, and no increase in noise is observed even after three successive anneals. This empirical result indicates that Ti/Pd/Au stacks constitute a more reliable approach for future device fabrication.

After device fabrication on the membranes, the membranes are prepared for transfer to cantilever tips.

4.4.4 Membrane Release and Transfer to Cantilevers

To enable transfer, triangular membrane devices are defined by EBL (PMMA 672.045[9], spin three times at 4000 rpm, 40 s, bake 150 °C for 2 min, thickness ∼600 nm, dose 375 µC/cm^2) and subsequent RIE[15] etching of SiN_x (3 min, O_2 5 sccm , CHF_3 50 sccm, 150 W) is performed. The triangles remain attached to the substrate by narrow beams, allowing controlled break-off under an optical microscope using a micromanipulator glass needle (Figure 4.10b). The resist layer is intentionally left on top of the released devices to facilitate manipulation and protect the NW.

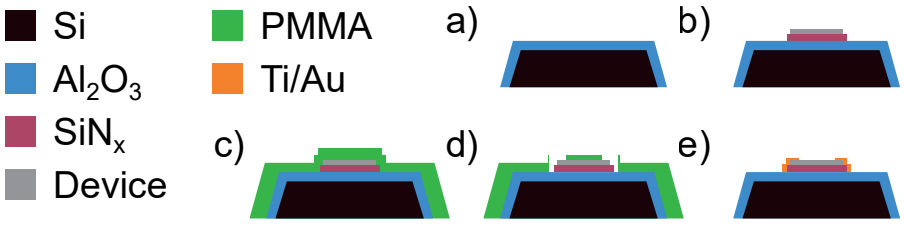

Figure 4.9: Process flow for fabrication of NWQD AFM lever (front view of the tip region, not to scale). **a)** Prepared ATEC featuring a FIB-defined plateau, conformal Al_2O_3 insulation, and rear bonding pads (not shown). **b)** Transfer of contacted NW device on a suspended SiN_x membrane onto the plateau. **c)** Application of PMMA resist by the floating-PMMA method. **d)** EBL and development to open vias to the membrane device electrodes. **e)** E-beam evaporation of Ti/Au and subsequent lift-off to form interconnects from the device to the cantilever pads, yielding a fully contacted NW at the cantilever apex with defined source, drain, and plunger gate.

Triangles are then picked up with a glass needle mounted on a micromanipulator

arm and transferred onto the plateau of pre-fabricated AFM cantilevers. In early trials, attachment to the plateau was achieved using UV-curable adhesive, in subsequent, separate trials, a two-part epoxy[24] was used. In later iterations, it was found that simple placement without adhesive was sufficient for the membranes to remain in place throughout subsequent processing, likely due to van der Waals adhesion.

Asymmetrical designs facilitate orientation control during transfer, since the thin membranes appear nearly transparent under optical inspection. After placement, the protective PMMA is removed by O_2 plasma (4 min, O_2 20 sccm, 60 W).

Once transferred, the final processing of contacting the device is performed directly on the cantilever.

4.4.5 Final Processing on Cantilevers

Following transfer, the cantilevers are coated with PMMA using the floating-layer technique displayed in Figure 4.3. To prevent displacement of the membranes, the samples are left to dry in vacuum for at least 1 h before baking. Coated levers are inspected optically, and only those where the membrane remains properly positioned are processed further. EBL patterning of interconnect lines from the membrane electrodes to the cantilever bonding pads follow the same strategy as described for the multi-gate lever (Section 4.3.3), with the difference that only two apertures (7.5 and 60 µm) are employed and the dose is 225 µC/cm^2. After exposure, the resist is developed (1 min in AR-600-55[22], 1 min IPA), O_2 plasma (30 s, O_2 20 sccm, 30 W) descum is performed, and metallized with 5 nm of Ti and 75 nm of Au by e-beam evaporation with rotation. Lift-off is carried out in ACE at 50 °C with gentle pipette agitation, followed by an IPA rinse and N_2 blow-dry.

Figure 4.9 presents an overview schematic of the cantilever fabrication sequence. Figure 4.10 shows four representative images of the corresponding process stages, from the prefabricated cantilever to a fully contacted NW charge sensor at the tip apex.

The completed levers are evaporated with 20 nm of Au from the backside to increase beam reflectance for better readout of the cantilever motion, glued onto the cantilever holder (Section 3.3.1), and wire-bonded to the PCB. Proper grounding during operation is critical to prevent electrostatic discharge damage as discussed in Section 3.5.

[24]Araldite Standard G, Huntsman Advanced Materials

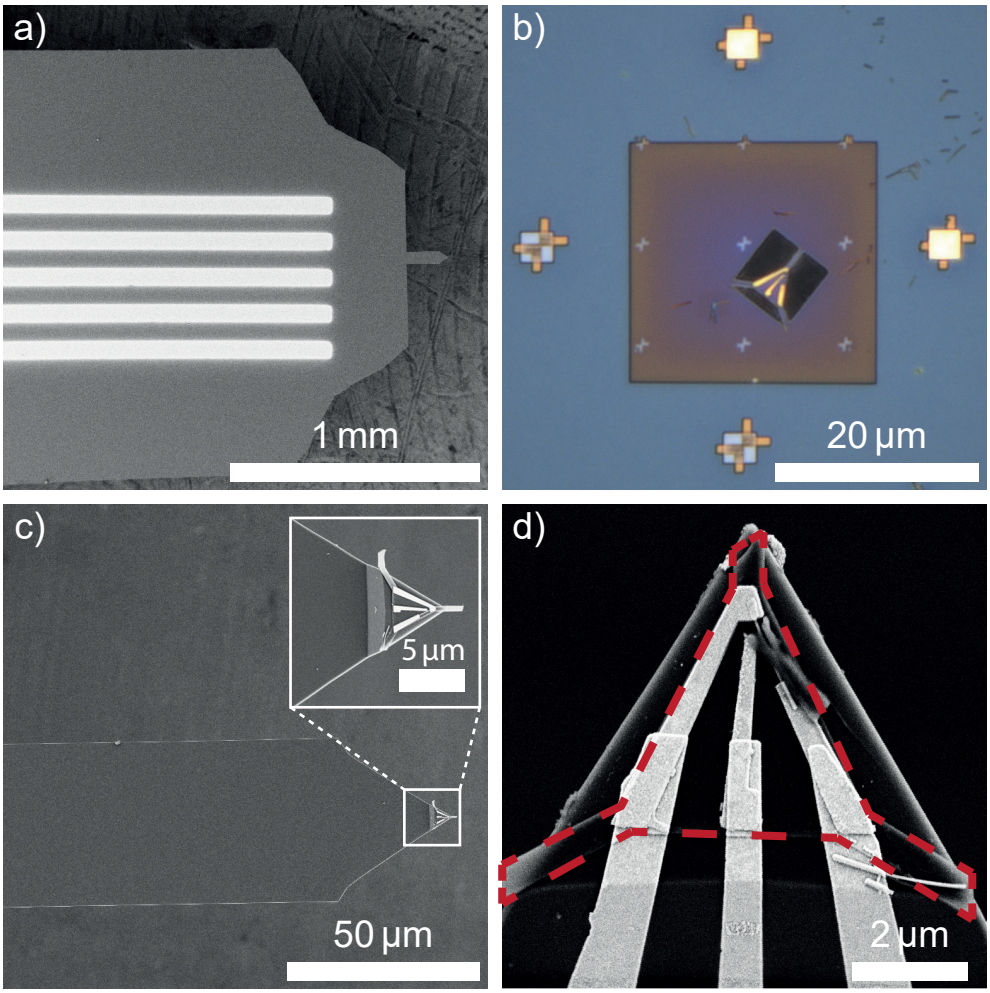

Figure 4.10: Integration of NW device on AFM cantilever tip. **a)** SEM image of a prefabricated AFM cantilever platform with bonding pads and interconnect lines as described in Section 4.1. **b)** Optical micrograph of a suspended SiN_x membrane containing a contacted NW device. The membrane remains attached to the substrate by three narrow beams, which are broken during transfer with a glass needle. **c)** SEM image of a membrane triangle transferred onto the tip plateau of an AFM cantilever. Inset: magnified view of NW triangle on the plateau. **d)** SEM close-up of a contacted NW device positioned at the cantilever apex. The outline of the transferred membrane is indicated by the red dashed line for clarity. This sequence illustrates the assembly route from a prefabricated cantilever platform to a functional NW charge sensor at the tip apex.

With fabrication completed, the devices are subjected to annealing and low-temperature testing to optimize and verify their electrical performance.

4.4.6 Contact Annealing and Testing

Before electrical characterization, the contact resistance of the NW devices on the lever is reduced by thermal annealing. The initial protocol consists of Ar flushing followed by annealing at 200 °C for 10 min in vacuum. Devices are then screened in a dedicated low-temperature probe that reaches LHe temperature within ∼2 h, prior to installation in the scanning probe system, which requires ∼2-3 days for cooldown. Because this intermediate screening step exposes the devices to air and handling, a second anneal with the same vacuum recipe is typically performed immediately before mounting the lever into the scanning probe.

Subsequent measurements reveal that some NWQD levers exhibit excessive current noise after the second vacuum annealing, consistent with over-annealed contacts. To mitigate this, an optimized protocol is employed. Annealing is done in 30 mbar forming gas (FG) with a temperature ramp of ∼10 °C/min up to 190 °C, 20 min dwell time, and subsequent controlled cooldown. This modified process preserves low contact resistance while avoiding the noise increase observed after vacuum anneal.

A further advantage of the FG protocol is its ability to recover degraded devices. Samples stored in air for one week show negligible conductance and no Coulomb peaks. After the optimized anneal, Coulomb oscillations reappeared and transport is stable, indicating that the process not only lowers initial contact resistance but can also restore device performance after adverse storage.

In summary, commercially available NC-ATEC are converted into fabrication platforms by defining a tip plateau, cleaning, depositing an Al_2O_3 insulation layer, and patterning robust bonding pads. A floating-PMMA transfer is developed to achieve uniform resist coverage on sloped and suspended geometries, enabling both positive- and negative-tone EBL with sub-100 nm features. Two kinds of devices are realized: multi-gate levers defined by negative-tone pattern transfer into an Au base, and NWQD levers assembled via SiN_x membrane transfer and on-lever metallization. Process choices that improve yield are identified. The resulting levers constitute the device platforms used in Chapter 5 for proof-of-concept scanning experiments.

Chapter 5

Proof-of-Concept Experiments

This chapter reports proof-of-concept measurements performed with the two cantilever sensor types developed previously: scanning multi-gate levers and NWQD levers. It is organized as follows:

- Section 5.1 describes the scanner calibration, where in-plane scale factors are obtained from AFM images of lithographic markers and the out-of-plane response is calibrated interferometrically.
- Section 5.2 presents measurements with the multi-gate lever on a bare InAs NW, where constant-z maps reveal gate-induced conductance modulation and motivate constant-z operation.
- Section 5.2.2 demonstrates multi-gate operation above an InAs/InP NWQD, where equipotential rings, position-dependent lever coupling, and lever-induced Coulomb diamonds are observed.
- Section 5.3 introduces and characterizes the NWQD lever as a charge sensor. Coulomb diamonds verify device functionality and the intrinsic charge sensitivity for the NWQD on lever is extracted. A "reversed-plunger" configuration quantifies coupling to sample gates and constant-z scans in one- and two-gate configurations are compared to electrostatic simulations.
- Section 5.4 provides a comparative discussion of capabilities, limitations, and implications for further optimization.

Together, these sections establish the scanner calibration, demonstrate multi-gate local gating, validate the NWQD lever as a quantitative charge sensor, and relate scanning measurements to simulations, providing a concise proof-of-concept foundation for this work.

5.1 Calibration of the Scanning Probe

Calibration of the scanning probe is required to ensure that the system produces reliable and quantitatively meaningful images. Since the cantilever sensors are self-fabricated and integrated into a custom-built scanning probe system, it is necessary to verify that the response of the scanner piezos corresponds to the expected displacements. Manufacturer specifications provide nominal values for the piezo, but variations are introduced by wiring, mounting, load, and operation at LHe temperature. It is therefore insufficient to rely on nominal values, and calibration has to be performed under the actual measurement conditions. Importantly, only the scanning piezos are calibrated. The stepper motors are not characterized.

For the in-plane (x, y) calibration, a test sample with lithographic markers of known spacing is used. AFM images of the markers are compared to the separations determined from SEM images to establish the lateral scale. The manufacturer-specified scan range is found to correspond to approximately half of the piezo's achievable displacement. The piezo response is nonlinear across the full field of view, with larger errors occurring near the outer edges of the scan range. Possible reasons for the nonlinearity of the piezo are ferroelectric hysteresis, creep, and mechanical effects. To minimize these nonlinear effects, the scanned region is positioned near the bottom-left of the scan window using the stepper motors, where the piezo extension remains relatively small. A scale factor of 1.2 is identified for the bottom-left window, by comparing AFM images with SEM images of the same region. Consequently, all scan images shown in this thesis have been corrected in post-processing by this factor. This approach yields a practical compromise, where a global correction factor is applied while residual nonlinearities are acknowledged as a source of systematic uncertainty that is not corrected on a per-scan basis.

Calibration of the z-piezo is performed using an interferometric approach. Once the cantilever has approached the sample surface, the laser spot is shifted laterally off the cantilever onto the sample surface, thereby forming an optical cavity between the fiber end and the sample. During a continuous extension of the z-piezo, the interferometer signal exhibits periodic fringes as the cavity length decreases. Each fringe corresponds to a displacement of half the laser wavelength. By counting the number of fringes across the full piezo extension, the total displacement is obtained and compared with the nominal value. The measured displacement exceeds the nominal value predicted by a factor of 2.73, which is subsequently applied as the calibration factor for z. Within the accessible range, the response of the z-piezo is found to be linear. Although the z-piezo is calibrated with high precision using the interferometer, potential slow drift and creep under constant-z setpoints are not quantified in this work. Any such effects would add uncertainty to the absolute height over long timescales. For completeness, it is noted that repeatability to an

identical setpoint is not verified. It is not assessed whether returning to the same setpoint at a later time reproduces the same extension.

In summary, the z-piezo response is calibrated interferometrically with high accuracy and verified to be linear within range. The x-y scanner requires a global correction factor and exhibits residual edge nonlinearities that are not corrected for. The achieved calibration is adequate for the proof-of-concept experiments reported in this chapter, although a more refined treatment of piezo nonlinearities as well as quantitative assessment of z-axis drift and creep under constant-z operation remains a task for future optimization.

5.2 Multi-Gate Lever

5.2.1 Multi-Gate Lever on Bare InAs NW

The multi-gate lever employed in this experiment is fabricated as described in Section 4.3. It contains five individually addressable metallic gates extending to the tip plateau. The pitch and width of the gates are approximately 120 nm and 55 nm, respectively. A representative image of the device is shown in Figure 5.1a.

The sample consists of a bare undoped InAs NW of diameter 75 nm and length 6 µm, grown by the group of Lucia Sorba[1]. The wire is contacted by standard EBL. Prior to metallization, the native oxide is removed by in-situ IBE, followed by deposition of Ti/Au (5 nm/120 nm). Only source and drain contacts are fabricated, without additional gates. The NW is mounted on a custom PCB, bonded with aluminum wire, and annealed. A detailed fabrication recipe is given in Appendix A.1.2. Electrical characterization at room temperature yields conductance in the low kΩ range. The source-drain separation is 3 µm. The corresponding AFM image of the source and drain can be seen in Figure 5.1b.

Measurements are performed at LHe temperature in the scanning probe system described in Chapter 3. Frequency modulation AFM imaging is first carried out to identify a safe height for constant-z scan. Operation in constant-z mode is essential, because applying voltages to the lever gates produces frequency shifts that would otherwise trigger compensation movements of the z-piezo through the PLL feedback. For example, at one position, applying −3 V on a lever gate induces a frequency shift of −300 mHz, while −6 V on the same gate and at the same spatial position results in a −2.5 Hz shift. If the PLL has been left active, these shifts would have been compensated by z-piezo adjustments, masking the true electrostatic effect of the lever gates.

[1]NEST, Istituto Nanoscienze-CNR and Scuola Normale Superiore, Pisa, Italy

Throughout this thesis, "constant-z" is used to denote a fixed z-piezo extension (setpoint), not a strictly constant tip-sample separation. Accordingly, any reported height refers to the setpoint, with the understanding that the absolute spacing may vary due to cantilever bending, piezo creep/drift, and residual sample tilt.

After a safe scanning height is established, constant-z current maps are recorded by applying a source-drain bias to the NW and measuring the current with an I/V converter synchronized to the cantilever position as described in Section 3.4.1. Each of the five lever gates is biased to $-2\,\mathrm{V}$ in turn, with all other gates at $0\,\mathrm{V}$. For comparability, the current maps are normalized by subtracting the mean current measured in a $1\,\mu\mathrm{m}\times1\,\mu\mathrm{m}$ reference region in the upper left corner of the scan. This normalization facilitates direct comparison between measurements performed with different gates and reduces the impact of slow background drifts. The resulting images, shown in Figure 5.1c-g, reveal the outlines of the gates in the NW conductance signal. This confirms that each gate locally modulates the current. The magnitude of the effect, however, varies between gates. Possible reasons include small asymmetries of the FIB-milled plateau, tilt introduced during cantilever mounting, and variation in sample gluing, which varies the capacitive coupling between the gate and the sample. The back of the gates, which extend over the sloped region of the tip, has a reduced influence, since their effective distance from the NW increases in constant-z operation.

Attempts are also made to electrostatically define a QD in the bare NW using the lever gates. Three of the five gates can pinch-off the wire at voltages below $-10\,\mathrm{V}$ at the chosen position. Two of these gates are employed as tunnel barriers and a third as plunger. Although the current can be suppressed, reproducible Coulomb blockade is not observed. Some traces display irregular structures that resemble Coulomb oscillations, but these cannot be attributed unambiguously to dot formation.

Notably, attempted dot formation also led to apparent suppression of conductance across the NW. This effect was initially mistaken for device failure. However, the conductance is fully restored after warming up the device, indicating that the suppression is reversible. A possible mechanism is transient charge trapping in or near the NW, which can modify local electrostatics and intermittently block transport without permanently damaging the device. This interpretation is supported by reports of transient charging of surface/oxide traps in or near InAs NWs, which dynamically alter the local electrostatics and produce hysteresis, random-telegraph-like switching, and even temporary conductance suppression that recovers upon trap emptying via heating or over time. [124–126] Additionally, it is reported that a biased scanning cantilever can deposit and pattern charge on insulating and oxide surfaces. [127, 128]

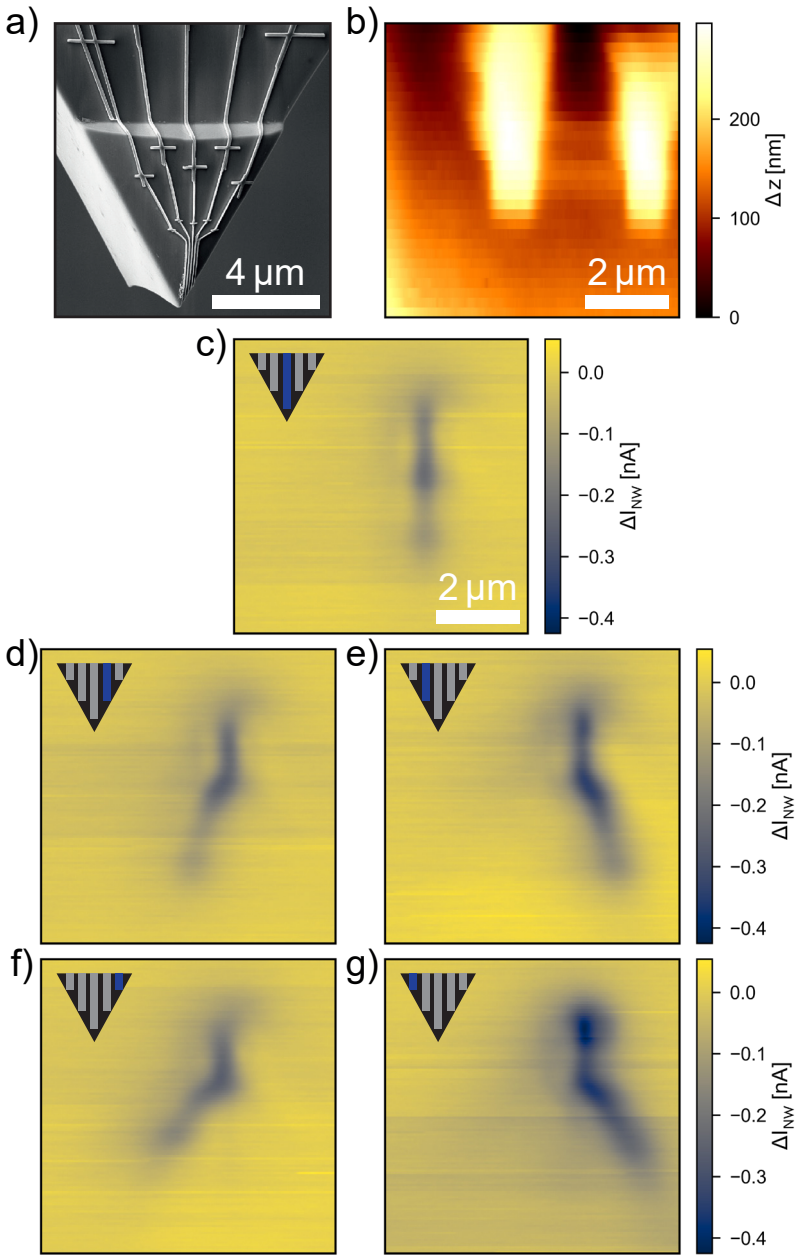

Figure 5.1: Gate-defined conductance modulation in a bare InAs NW using a multi-gate AFM lever. **a)** SEM image of the lever with five independent gates extending to the tip apex. **b)** AFM topography of the InAs NW (plane detrended). **c-g)** Constant-z current maps of a bare InAs NW, recorded while biasing one gate at −2 V (Inset schematics: active gate blue, others gray, 0 V). Current change ΔI_{NW} reflects the spatial influence of the lever gate, revealing the outline of the biased gate. Current values are normalized to a $1\times1\,\mu\mathrm{m}^2$ reference region (upper left corner) to facilitate comparison between different gates. Scale bar common to b-g.

In summary, this experiment demonstrates that all five lever gates are functional and can, depending on the position, strongly modulate NW conductance. The work also establishes constant-z operation as the mode for such measurements, since PLL-based constant-frequency operation introduces large artifacts. The data confirms the viability of multi-gate levers as local gate structures, while also showing that reliable dot formation in bare InAs NWs remains challenging.

5.2.2 Multi-Gate Lever above NWQD

A second proof-of-concept experiment is performed with a multi-gate lever above an InAs NW containing intrinsic InP tunnel barriers. The NW has a diameter of 50±5 nm with a 19 nm InAs island confined between two 5 nm InP barriers and is grown by gold-assisted chemical beam epitaxy by the group of Lucia Sorba[2]. The NW is contacted with Ti/Au (5 nm/65 nm) electrodes following in-situ oxide removal by IBE. In addition, a plunger gate is fabricated adjacent to the QD, enabling tuning of its charge state independently of the lever gates. Details of the fabrication are shown in Appendix A.1.3. The sample is mounted in the scanning probe together with the multi-gate lever and cooled down to LHe temperature.

The device is first tuned using the sample plunger gate to a regime with closely spaced Coulomb peaks ($V_{PG} = 8.6\,\mathrm{V}$). At this operating point, constant-z current maps are recorded while individual lever gates are biased to 6 V, with all other gates at 0 V. Several tip-sample separations are investigated, referenced to a height ($\Delta z = 0\,\mathrm{nm}$) corresponding to a -5 Hz frequency shift at the upper left of the scan area. Tip-sample distance is reduced as Δz gets more negative. Representative results are displayed in Figure 5.2, together with control scans where no lever voltage is applied.

The maps reveal ring-like features that correspond to equipotential contours, as seen previously in SGM [129, 130], where the lever-induced electrostatic potential shifts the QD occupation by one electron. As the tip approaches the sample additional rings become visible, consistent with stronger capacitive coupling at reduced distance and consistent with literature. [129, 130] Figure 5.2b shows an AFM topography with overlaid outlines of the source (S), drain (D), gate (G), and NW, as well as a neighboring electrode (NE). These outlines are drawn for clarity. Their positions are registered from an AFM topography acquired prior to the constant-z current map measurements. An offset of ∼1 µm is observed between the ring center in the current maps and the QD position inferred from the AFM image. This displacement is consistent with the ∼1 µm lateral separation between the AFM plateau-tip and the gate setback on the plateau (see Figure 5.2a).

[2]NEST, Istituto Nanoscienze-CNR and Scuola Normale Superiore, Pisa, Italy

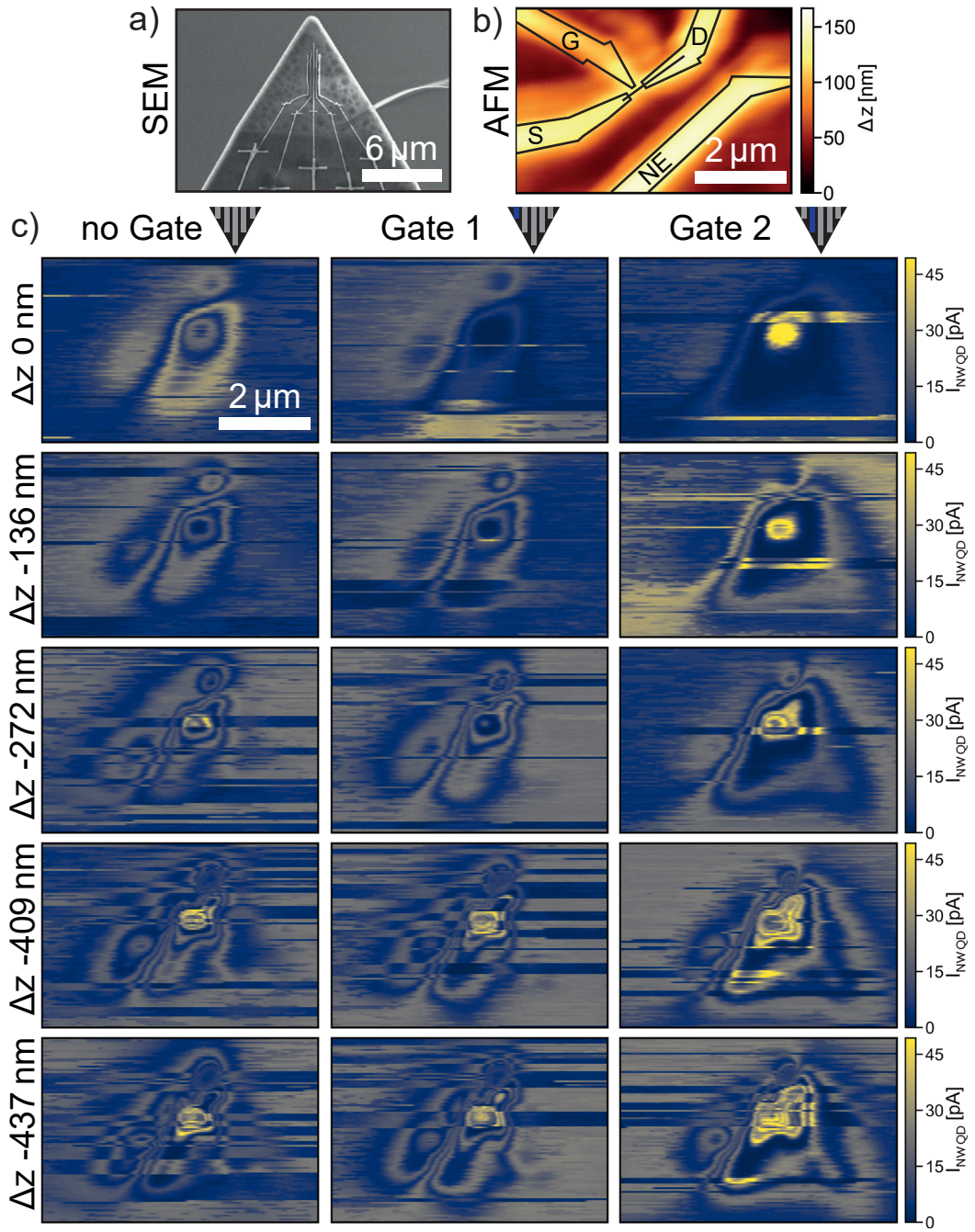

Figure 5.2: Electrostatic influence of single lever gates on an InAs/InP NWQD. **a)** SEM of the multi-gate lever after scanning (separate scale bar). **b)** AFM topography with outlines of the S, D, G, NW and a NE, drawn for clarity. **c)** Constant-z current maps with one gate at 6 V (schematics: active gate blue, others gray, 0 V). Rows decreasing Δz (more negative = smaller tip-sample separation). Ring-like patterns mark electron charging of the QD. Shown: no gate, weakly coupled Gate 1, strongly coupled Gate 2. Scale bar common to b and c.

The modulation strength varies strongly between gates. For example, Gate 2 produces pronounced oscillations, while Gate 1 shows only minimal coupling, similar to the no-gate reference. Such differences can arise from slight asymmetries of the FIB-milled plateau, variation in cantilever tilt during mounting, or leakage in the oxide insulation, or non-functional gates.

In several maps, multiple ring centers are visible. In addition to the intrinsic dot defined by the InP barriers, an additional center appears in the vicinity of the source and drain electrodes. These features may reflect localized states forming near the metal contacts, which can give rise to ring-like signatures in scanning gate maps.

The data also exhibits noise, which is attributed to charge fluctuation occurring on the timescale of the relatively long scans of $\sim$1 h. In later experiments it is revealed that keeping the interferometer laser on during such measurements further amplifies noise (see Section 5.3.1). This explains the reduced stability and signal quality observed here.

To further probe the spatial variation of the lever coupling, Gate 2 is next used as a mobile plunger electrode. The tip is brought closer to the surface ($\Delta z = -545\,\mathrm{nm}$) and the dot is tuned into a regime with higher Coulomb peaks ($V_{PG} = 9.05\,\mathrm{V}$). At this operating point, the lever gate 2 voltage (V_{LG2}) is swept from 0 to 10 V at a grid of positions separated by 300 nm across the scanned area. Representative traces are shown in Figure 5.3.

The raw traces are strongly affected by noise. To improve clarity, the data is processed by a two-step filtering procedure. First, a median filter is applied to suppress spikes, followed by a third-order Butterworth low-pass filter with normalized cutoff frequency of 0.05. The raw data are displayed as faint gray traces, while the filtered data are shown in color. The measurements reveal a pronounced dependence of the lever arm on lateral position. At certain positions (e.g., Figure 5.3b and h), multiple Coulomb oscillations appear, indicating strong capacitive coupling between the lever gate and the dot. At other positions (e.g., Figure 5.3a, d, g), the coupling is too weak to resolve any peaks. Intermediate cases (Figure 5.3c, e, f) exhibit broadened oscillations, consistent with weaker coupling and reduced lever arm.

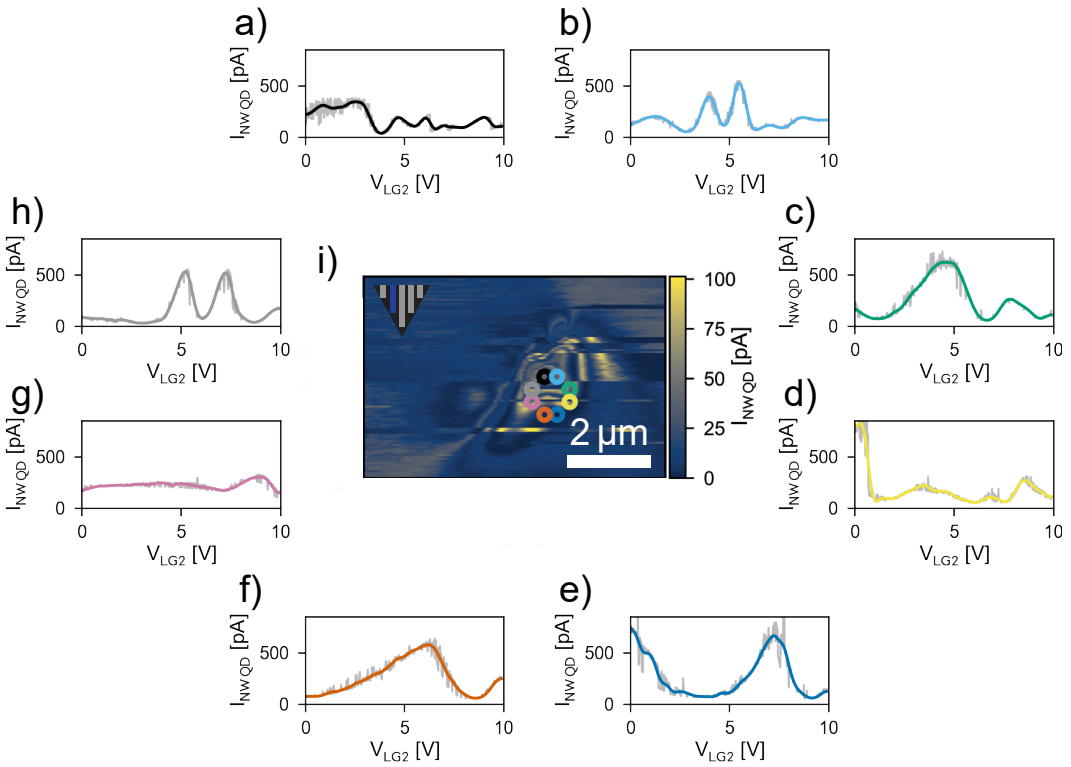

Figure 5.3: Local lever gating of an InAs/InP NWQD at multiple positions. **a)-h)** Current through the sample QD as a function of the lever gate voltage (V_{LG2}) recorded at positions marked by colored circles in panel i). The faint gray traces represent raw data, while the colored lines display the same traces after spike removal by median filtering and subsequent low-pass smoothing. Depending on the measurement position, the lever arm varied strongly: in some cases (e.g., b, h) multiple Coulomb oscillations are observed, while in others (e.g., a, d, g) no clear peaks are recognizable. Intermediate cases (e.g., c, e, f) showed broadened oscillations consistent with weaker capacitive coupling. **i)** Constant-z current map with overlaid positions where the gate sweeps are performed. The variation across positions highlights the strong geometrical dependence of the lever-QD coupling.

At the most favorable positions identified from the oscillation scans, full Coulomb stability diagrams are measured. Figure 5.4 displays representative data, where current through the dot is plotted as a function of V_{LG2} and V_{SD} (source-drain bias). Clear Coulomb diamonds are observed, demonstrating that the lever gate can act as an effective mobile plunger, adding or removing electrons from the dot.

Interestingly, the strongest and most stable coupling is not obtained directly above the centers of the rings observed in the constant-z maps, but rather at nearby

displaced positions. This discrepancy may result from small offsets of the piezo scanner between imaging and point measurements. When the lever is positioned exactly at the ring center, Coulomb diamond measurements are noisy and unstable, whereas moving the lever off center yields cleaner and more reproducible diamonds.

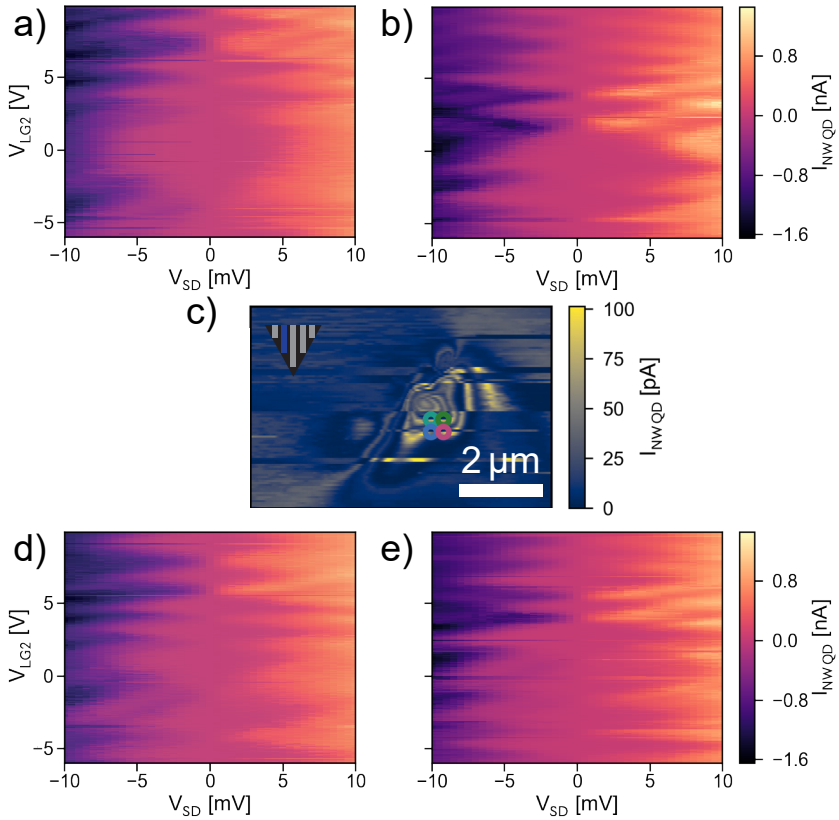

Figure 5.4: Coulomb diamonds obtained by lever gating of an InAs/InP NWQD. **a)**, **b)**, **d)**, **e)** Current through the sample QD as a function of lever gate voltage (V_{LG2}) and V_{SD}, recorded at positions marked by colored circles in panel **c)**. The circles correspond to: top-left = **a)**, top-right = **b)**, bottom-left = **d)**, bottom-right = **e)**. Coulomb diamonds are visible, demonstrating that the lever gate can add and remove individual electrons from the dot by tuning its electrostatic potential. **c)** Constant-z current map at $\Delta z = -545\,\text{nm}$ with overlaid measurement positions.

This experiment establishes that lithographically defined gates on an AFM cantilever can directly couple to a semiconductor QD in the sample. Equipotential contours, Coulomb oscillations, and full Coulomb diamonds are observed, all induced by the lever gates. Three of the five gates show significant coupling, while two are ineffective, likely due to oxide leakage and geometric asymmetries. The data reveals concentric equipotential contours of the QD, a hallmark of scanning gate

microscopy, here obtained using lithographically defined lever electrodes rather than a sharp conducting tip.

A significant limitation is the presence of noise in all the measurements, which can be mitigated in future experiments by switching off the interferometer laser during sensitive measurements. Furthermore, the fact that only three of the five gates are operational underlines the importance of fabrication improvements. Despite these limitations, the results demonstrate the feasibility of using multi-gate levers as movable local gates for QD experiments.

5.3 NWQD Lever

Portions of this chapter form the basis of a manuscript in preparation.

5.3.1 Lever-QD as Charge Sensor

The NWQD cantilever used in this experiment is fabricated as described in Section 4.4. Briefly, an InAs NW with intrinsic InP barriers is first contacted on a suspended SiN_x membrane and then transferred to the tip of an AFM cantilever. Subsequent EBL defines interconnects from the prefabricated device on the tip to the bonding pads. The cantilever is glued to the holder, bonded with Al wire, and mounted into the scanning probe setup, which is then cooled to LHe temperatures. An image of the device used for this experiment is shown in Figure 4.10d.

As a sample, a bare InAs NW is employed, fabricated in the same way as for the multi-gate lever experiments (Section 5.2.1). In addition to source and drain contacts, six local gates (three on each side of the wire) are included to allow the possibility of forming a QD electrostatically (fabrication details in Appendix A.1.2).

Characterization of the NWQD Lever

Before scanning, the lever device is characterized to verify the formation of a QD on the tip. Coulomb oscillations are measured by applying V_{SD} to the lever NW and sweeping the plunger gate (V_{LG}) on the lever. The current is read out via an I/V converter and digitized by a DMM (10 PLC integration) or during scanning by the Nanonis (see Section 3.4.1). The Coulomb oscillation measurements reveal strong noise, which is significantly reduced when the optical interferometer laser is switched off. Figure 5.5d illustrates this effect. In the measurement shown in Figure 5.5d, Coulomb oscillations are recorded first without the interferometer laser (left side, lower-noise trace) and then, above V_{LG} =6.25 V with the laser switched on (gray-shaded region), where a pronounced increase in current fluctuations is

observed. This behavior is consistent with laser-induced perturbations of InAs NWs. [131, 132] Photons at a wavelength of 1550 nm have an energy of ∼0.8 eV, which exceeds the InAs band gap (∼0.4 eV at 300 K [133]), therefore absorption and photogeneration are expected under the used readout wavelength. Such photogeneration can produce a photovoltage in the NWQD system, leading to additional shot-like and 1/f type current noise, and has been directly exploited in InAs NW photodetectors at 1550 nm. [131] In line with this interpretation, all subsequent current measurements are therefore performed with the laser off to suppress optically induced noise.

Coulomb diamonds obtained from the lever-QD are shown in Figure 5.5a. Differential conductance maps (Figure 5.5b) additionally highlight excited states. These data demonstrate the successful realization of a functional QD at the tip of a NC-AFM cantilever, validating the fabrication procedure described in Chapter 4.

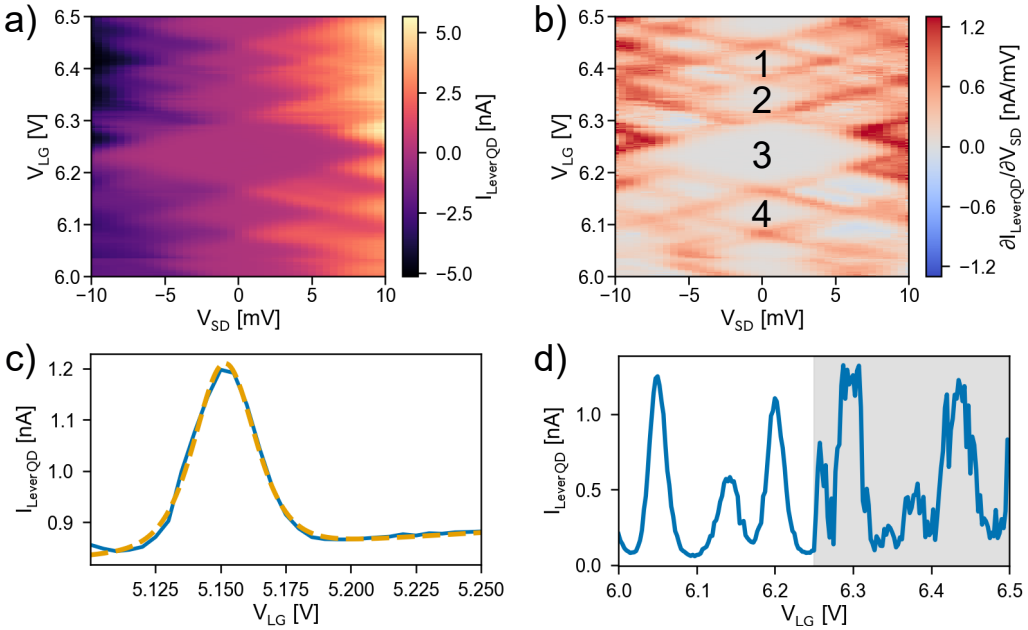

Figure 5.5: Characterization of the NWQD cantilever. **a)** Coulomb diamonds measurement of the NWQD at the tip. **b)** Differential conductance highlighting excited states with numbered Coulomb diamonds referring to Table 5.1. **c)** Coulomb peak used to calibrate the charge sensor response (blue data, orange fit). **d)** Coulomb oscillations recorded with the laser off and then on (gray-shaded region), demonstrating noise induced by the optical readout.

From the Coulomb diamond data (Figure 5.5a), device capacitances C and the lever arm α_G are extracted following Su et al. [25]. The gate, source and drain

capacitances (C_{LG}, C_s, C_d) are obtained from the slopes of the diamond edges. The lever arm is evaluated as $\alpha_G = C_{LG}/C_\Sigma$. Additionally, the conductance near zero source-drain voltage and the intrinsic current response of the source-drain current to the charge ($R_{q0}(V_{LG})$) is extracted as in [25]. For each Coulomb diamond, the electron temperature T_e is extracted from a near–zero-bias Coulomb peak by using the thermal width relation FWHM $\approx 3.53 k_B T_e/(e\alpha_G)$ [25]. This yields a mean T_e of 4.6 K for the four different Coulomb diamonds labeled in Figure 5.5b and indicates effective electronic thermalization of the scanning probe head.

Using those values, the sensitivity δQ_{JN} limited by Johnson-Nyquist noise is calculated using Equation 2.12 and adapting to:

$$\delta Q_{JN}(V_{LG}) = \frac{\sqrt{4k_B T_e G(V_{LG})}}{e|R_{q0}(V_{LG})|} \tag{5.1}$$

Similarly, for the shot noise, Equation 2.8 is used and adapted to:

$$\delta Q_{shot}(V_{LG}) = \frac{\sqrt{2e|I(V_{LG})|F}}{e|R_{q0}(V_{LG})|} \tag{5.2}$$

To obtain the white-noise level, the quadrature sum of the shot noise and the Johnson-Nyquist noise is calculated using:

$$\delta Q^{white}_{Noise}(V_{LG}) = \sqrt{\delta Q^2_{JN}(V_{LG}) + \delta Q^2_{shot}(V_{LG})} \tag{5.3}$$

To estimate the contribution from 1/f noise, time-trace data of the sensor current would be required. However, such data is not available for the NWQD lever investigated here, and no direct 1/f spectrum is recorded. Instead, the low-frequency current noise spectral density is obtained from scanning data recorded with the NWQD sensor parked on a Coulomb-peak flank. Scans of the sample with no sample voltage are analyzed. A current versus time trace from a scan region of interest (ROI) free of sample signal is reconstructed. Its power spectral density (PSD) is fitted to a 1/f plus white-noise model:

$$S_I^{1/f}(f) = \frac{A_I^2}{f} + S_0 \tag{5.4}$$

The extracted amplitude A_I is converted to an equivalent input charge noise via the sensor's transduction factor $e|R_{q0}(V_{LG})|$, determined from the Coulomb-peak slope at the operating setpoint. A more detailed description can be seen in Appendix B.6.2. The corresponding input-referred charge noise is obtained as:

$$\delta Q_{1/f}(f, V_{LG}) = \frac{A_I/\sqrt{f}}{e|R_{q0}(V_{LG})|} \tag{5.5}$$

The resulting 1/f-limited charge noise, expressed in units of $e/\sqrt{Hz}$, is combined in quadrature with the white-noise contributions to obtain the total charge sensitivity:

$$\delta Q_{tot}(V_{LG}) = \sqrt{\delta Q_{JN}^2(V_{LG}) + \delta Q_{shot}^2(V_{LG}) + \delta Q_{1/f}^2(V_{LG})} \tag{5.6}$$

The extracted capacitances (C_{LG}, C_s, C_d), total capacitance C_Σ, α_G, and the resulting δQ values are summarized in Table 5.1 for the four representative Coulomb diamonds labeled in Figure 5.5b. The Johnson-Nyquist and shot-noise contribution yield δQ_{Noise}^{white} values in the low $10^{-5} e/\sqrt{Hz}$ range for three out of the four analyzed diamonds. In contrast, diamond 3 (see Figure 5.5) shows significantly larger δQ_{Noise}^{white}, which correlates with its smaller extracted capacitances.

	Diamond 1	**Diamond 2**	**Diamond 3**	**Diamond 4**
C_{LG} **[aF]**	2.2	2.1	1.2	2.1
C_s **[aF]**	17.7	17.6	9.5	15.8
C_d **[aF]**	22.1	21.3	8.3	16.5
C_Σ **[aF]**	42.0	41.0	19.1	34.3
α_G	0.053	0.052	0.064	0.060
δQ_{JN} **[e/$\sqrt{\text{Hz}}$]**	1.72×10^{-5}	1.28×10^{-5}	48.63×10^{-5}	2.04×10^{-5}
δQ_{shot} **[e/$\sqrt{\text{Hz}}$]**	1.40×10^{-5}	1.09×10^{-5}	38.37×10^{-5}	1.45×10^{-5}
δQ_{Noise}^{white} **[e/$\sqrt{\text{Hz}}$]**	2.22×10^{-5}	1.68×10^{-5}	61.95×10^{-5}	2.50×10^{-5}
$\delta Q_{1/f}$ **[e/$\sqrt{\text{Hz}}$]**	$\sim 3.7 \times 10^{-3}$(1Hz)			
δQ_{tot} **[e/$\sqrt{\text{Hz}}$]**	$\sim 3.7 \times 10^{-3}$			

Table 5.1: C, α_G, and δQ for the lever NWQD. Values are extracted from Coulomb-diamond measurements of the calibration diamonds used to quantify the lever–QD sensor. $\delta Q_{1/f}$ is determined separately using the current-noise spectral density obtained from constant-z scanning data and the reference Coulomb peak of Figure 5.5c.

Comparison with literature indicates that the white-noise contribution of the present device is in the same range as reported in [25]. However, because the present measurements are performed in DC, the effective sensitivity is expected to be dominated by low-frequency fluctuations.

The scanning 1/f noise is extracted in reference to the Coulomb peak shown in Figure 5.5c and is extracted to be $\delta Q_{1/f}(1\text{Hz}) \simeq 3.7 \times 10^{-3}\, e/\sqrt{Hz}$. The scanning 1/f noise extracted exceeds both Johnson-Nyquist and shot noise by two orders of magnitude. The total sensitivity of the present NWQD lever sensors therefore lies in the range of $10^{-3}\, e/\sqrt{Hz}$. The charge sensitivity reported by [11] using an SET

system based on carbon nanotubes [62] is $\delta Q \sim 2 \times 10^{-5}\,\mathrm{e}/\sqrt{\mathrm{Hz}}$ which is at least two orders of magnitude better than the one reported here.

These results demonstrate that the NWQD lever is functional and capable of charge sensing. Nevertheless, its sensitivity is strongly limited by low-frequency noise in DC readout. This motivates the exploration of other readout configurations that improve high-frequency performance and reduce sensitivity to slow charge fluctuations. In the following section, a reversed-plunger configuration is introduced, which enables the extraction of the sensor response with respect to the sample gate and provides a more direct assessment of its voltage sensitivity in the scanning configuration.

Reversed-Plunger Experiment

To provide rough voltage-sensitivity numbers to quantify the NWQD lever, a reversed-plunger configuration is implemented. In this geometry, the NWQD located on the cantilever is tuned to a region with many neighboring Coulomb peaks. Then a gate on the sample acts as the plunger. The cantilever is positioned above a selected sample gate, and Coulomb diamonds measurements are acquired by sweeping the sample-gate voltage. Representative stability diagrams are presented in Figure 5.6, recorded at the closest approach ($\Delta z = 0\,\mathrm{nm}$) and at an increased tip-sample separation of $\Delta z = 273\,\mathrm{nm}$. From the slopes and addition energies of the diamonds, C_s, C_d and the sample-gate capacitance (C_{SG}) are extracted, together with C_Σ and α_G^{SG}, following the procedure outlined by Su et al. [25] The extracted values are presented in Table 5.2. As expected for capacitive coupling, the extracted α_G^{SG} decreases with increasing Δz, resulting in a degraded gate-referred sensitivity.

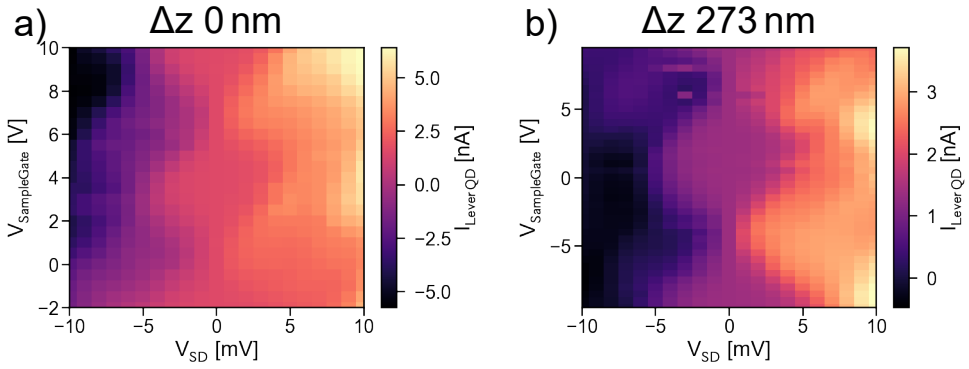

Figure 5.6: Measurement data of reversed-plunger configuration. **a)** Coulomb diamonds measured with the lever-QD while sweeping the sample gate as the plunger at Δz =0 nm. **b)** Same measurements taken at increased separation of Δz =273 nm, showing a reduced lever arm to the sample gate.

Based on the total charge sensitivity $\delta Q_{tot} \simeq 3.7 \times 10^{-3}\,\mathrm{e}/\sqrt{\mathrm{Hz}}$ obtained from the NWQD characterization (Table 5.1), the gate-referred voltage sensitivity δV_{SG} is determined. The conversion is performed using the coupling capacitance C_{SG} according to:

$$\delta V_{SG} = \frac{e}{C_{SG}} \delta Q_{tot} \tag{5.7}$$

	$\Delta z = \mathbf{0\,nm}$	$\Delta z = \mathbf{273\,nm}$
C_{SG} **[aF]**	0.024	0.018
C_s **[aF]**	16.7	14.3
C_d **[aF]**	10.4	12.4
C_Σ **[aF]**	27.1	26.7
α_G^{SG}	0.87×10^{-3}	0.66×10^{-3}
δV_{SG} $\mathbf{[V/\sqrt{Hz}]}$	2.52×10^{-2}	3.38×10^{-2}

Table 5.2: Capacitances extracted from reversed-plunger Coulomb diamonds at two tip-sample separations, together with α_G and δV_{SG}.

At the closest approach ($\Delta z = 0\,\mathrm{nm}$) a voltage sensitivity of $2.52 \times 10^{-2}\,\mathrm{V}/\sqrt{\mathrm{Hz}}$ is obtained, while at $\Delta z = 273\,\mathrm{nm}$ the sensitivity decreases to $3.38 \times 10^{-2}\,\mathrm{V}/\sqrt{\mathrm{Hz}}$, corresponding to a relative degradation of $\sim 35\,\%$. With δV_{SG} of the order $10^{-2}\,\mathrm{V}/\sqrt{\mathrm{Hz}}$, features in the 10-20 mV range are readily resolvable with practical averaging times. By contrast, sub-5 mV contrasts would require substantially longer integration unless 1/f noise is suppressed (e.g., lock-in modulation) or the lever arm is increased.

The observed reduction highlights the strong dependence of sensitivity on tip-sample separation. The QD on the lever is recessed from the tip apex by $\sim 1.8\,\mu\mathrm{m}$ along the cantilever axis (see Figure 4.10d). With the cantilever mounted at an incidence angle of 10° relative to the sample plane, this setback implies a vertical offset of $z_{QD} = 1.8\,\mu\mathrm{m} \times sin(10°) \approx 310\,\mathrm{nm}$ when the apex itself touches the surface. In addition, the QD sits on a $\sim 50\,\mathrm{nm}$ thick SiN_x membrane, yielding an effective minimum achievable QD-sample distance of about 260 nm. This offset limits the effective coupling and emphasizes the importance of positioning the QD as close as possible to the tip for optimized sensitivity performance.

When compared with the literature, the present sensitivities are about four orders of magnitude worse than those reported by Ella et al. [12]. This difference is mainly attributed to the DC readout used here, which is strongly affected by 1/f noise, in contrast to the audio-frequency readout employed by Ella et al. [12] A further difference is the larger tip–sample stand-off in the present work (vs. $\sim 220\,\mathrm{nm}$ in Ref. [12]), which weakens capacitive coupling and degrades δV_{SG}. The discrepancy

is consistent with the findings of the previously extracted δQ_{tot}. The reversed-plunger data does not independently reinforce the 1/f limitation. The relatively poor δV_{SG} primarily reflects the dominance of 1/f noise in the DC readout that sets δQ_{tot}, while the experiment demonstrates how gate referred sensitivities can be obtained and is strongly dependent on coupling and therefore the distance between the QD and the sample.

This configuration is complementary to the multi-gate lever geometry. In the latter, gates fabricated on the cantilever tune a QD in the sample (see Section 5.2), whereas in the reverse-plunger approach, a sample gate tunes a QD integrated on the cantilever. Together these results highlight the versatility of cantilever-based platforms for nanoscale charge sensing.

Constant-z Scanning with the NWQD Sensor

Having confirmed the functionality of the lever-QD, the sensor is used for scanning. An AFM image of the device under study is shown in Figure 5.7a. For quantitative display, AFM topography scans are leveled by subtracting a best-fit plane $Z(x, y) = ax + by + c$. In Figure 5.7a the slopes are about 30 nm/µm in x and 1 nm/µm in y, indicating a significant x-tilt and a negligible y-tilt across the scan window. The three lower gates (left side) are grounded, except for the middle gate, which is biased at 1 V. The lever-QD is tuned to the flank of a Coulomb peak to maximize charge sensitivity. Constant-z scans are performed at Δz =0 nm, 68 nm, 136 nm, 205 nm, and 278 nm (with Δz =0 nm defined at the closest safe approach). For larger separations, additional scans are acquired in ∼278 nm increments. Constant-z scans refer to a fixed scanner z-position, no compensation for the ∼30 nm/µm x-tilt is applied, so the true tip-sample separation varies along x.

The conversion from lever-QD current to an equivalent local gate shift ΔV_g^{eq} (as plotted in Figure 5.7 and 5.8) is calibrated from a single Coulomb resonance peak displayed in Figure 5.5. The peak is modeled by the standard thermally broadened lineshape with a linear background [134, 135]:

$$I(V_{LG}) = \frac{A}{cosh^2((V_{LG} - V_0)/(2k_B T_e))} + mV_{LG} + b \tag{5.8}$$

where A is the peak amplitude, V_0 the peak center, T_e the effective electron temperature, and m and b account for a weak background slope and offset. A nonlinear least-squares fit is performed in a narrow gate window bracketing the maximum to avoid neighboring features and ensure local linearity of the background. The calibrated model is then restricted to the rising flank ($V_{LG} < V_0$) to obtain $V_{LG}(I)$ only for currents within the valid flank range. In practice, each pixel current in a scan is thus mapped to the plunger voltage.

For each height, a "no-gate" reference scan (sample gates all at 0 V) is processed identically and subtracted from the corresponding "gate-on" scan to isolate the gate-induced shift. A small reference region is used to define the zero level by subtracting the mean over this ROI, yielding ΔV_g^{eq} with a common baseline per height. For the 1 V gate scans the global minimum across panels is subtracted so that color scales are non-negative.

Figure 5.7b-f display the resulting current maps for the one gate configuration, which represent the spatial variation of the electrostatic potential sensed by the lever-QD. A consistent increase of ΔV_g^{eq} is observed above the lithographic gate biased at 1 V for all tip-sample separations. Finite ΔV_g^{eq} responses are also visible near the source/drain contacts and above the nominally grounded structures (the three gates at the upper right, the alignment marker, and the two gates adjacent to the 1 V gate), most prominently at smaller Δz. The responses of the two gates adjacent to the 1 V gate are not clearly resolved in the maps of Figure 5.7, as their amplitudes remain below the dominant signal from the biased gate and other grounded features. However, line cuts in Figure 5.9c reveal small shoulders next to the main peak, which are attributed to the lever-QD response to these grounded electrodes.

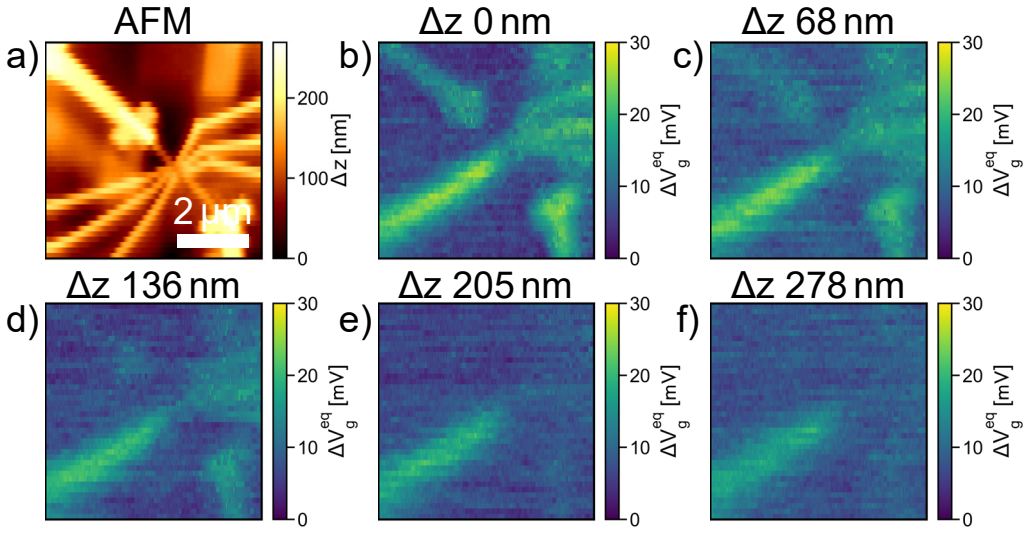

Figure 5.7: One-gate scanning experiment with the NWQD lever. **a)** AFM image of the InAs NW with local gates. Image is plane detrended by subtracting least-squares plane. **b-f)** Response map of lever NWQD recorded at different Δz showing the electrostatic potential map induced by a 1 V bias on the middle left gate. $\Delta z = 0$ is the smallest tip-sample distance. Scale bar common to all maps.

A possible explanation for the residual ΔV_g^{eq} observed above nominally grounded gates, and for its increase toward the right side of the scan, is a combination of sample tilt and a small z-offset between scan series. The leveled AFM topography shows an x-tilt of $\sim$30 nm/µm and a negligible y-tilt ($\sim$ 1 nm/µm). Under constant-z operation (fixed z-piezo extension), such a tilt produces a reduction of the tip–sample separation toward positive x. Over the 6 µm field of view, the QD is therefore expected to be $\sim$180 nm closer at the right edge than at the left. Because the maps with the selected gate at 1 V were recorded at several heights first and the background maps (all gates at 0 V) were acquired afterward, a small offset or drift in absolute tip-sample distance between the two series cannot be excluded. Background subtraction therefore does not remove contrast that arises from the z-dependence of the QD-sample lever arm. Moreover, the observed enhancement of ΔV_g^{eq} toward positive x is consistent with the decreasing tip-sample distance. The QD-sample capacitive coupling increases nonlinearly as the separation is reduced, so an identical geometric height difference yields a larger effective lever arm and thus larger ΔV_g^{eq} on the right side of the scan. In sum, both the nonzero ΔV_g^{eq} above grounded gates and its growth toward positive x are consistent with the sample tilt, a small z-offset between the background and the 1 V maps, and the nonlinear distance dependence of capacitive coupling.

The same measurement and processing procedure is repeated with two gates biased in opposite polarity. The lower left gate is at -1 V, the middle left gate is at 1 V, and the upper left gate is grounded. The data conversion and the data processing are done in the same way as for the one gate scans, except that, because two biased gates generate positive and negative local shifts, the display range is chosen symmetric about zero without global minimum subtraction. The corresponding results are presented in Figure 5.8, with Figure 5.8a showing the AFM topography and Figure 5.8b-f the sensor response at increasing distances.

The strongest signal is localized above the lithographic gates footprints visible in the AFM image. The polarity of the response is correct. Positive ΔV_g^{eq} is observed above the 1 V gate and negative ΔV_g^{eq} above the -1 V gate. At larger tip-sample separations, regions above grounded metal exhibit an approximately zero baseline. At the closest heights, a contrast above grounded metal remains visible but is reduced, with the exception of $\Delta z = 0$ nm, which shows weaker-than-expected contrast for reasons that are presently unclear. With increasing tip-sample distance, the features broaden and their amplitude decreases, consistent with electrostatic spreading and the expected decay of potential with distance. Taken together, these signatures provide a consistent and quantitative basis for attributing the measured contrast to local electrostatic potentials generated by the biased gates and support the conclusion that the NWQD lever is capable of imaging gate-induced

electrostatic potentials.

To assess whether the measured spatial profiles and their distance dependence are consistent with the device geometry, electrostatic simulations are next employed and compared directly with the experimental line cuts.

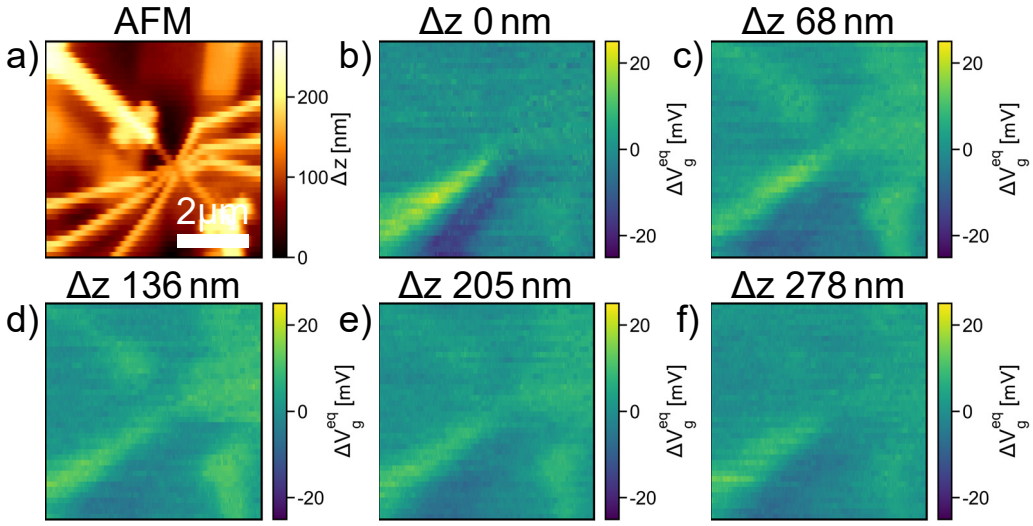

Figure 5.8: Two-gate scanning experiment with the NWQD lever. **a)** AFM image of the InAs NW with local gates. Image is plane detrended by subtracting least-squares plane. **b-f)** Response map of lever NWQD recorded at different Δz showing the electrostatic potential map induced by a 1 V bias on the middle left gate and a -1 V bias on the lower left gate. $\Delta z = 0$ is the smallest tip-sample distance. Scale bar common to all maps.

Comparison with COMSOL Simulations

To assess the measured potential patterns, electrostatic simulations of the device geometry are performed in COMSOL by solving the Poisson equation for different heights, corresponding to measurements taken at different tip-sample distances. Each simulation includes a ground plane 10 nm above the height at which the slice is taken to approximate the presence of the cantilever base. Although simplified, this approach provides a useful reference.

Line cuts are extracted from both experiment and simulation and compared in a single, fixed-model workflow. The conversion between the AFM set-height and the simulation slice heights is fixed by a constant scale factor b=2.73 (the z-calibration factor from Section 5.1). With this fixed scale, a single vertical offset a is fitted to best align experimental and simulation curves along the height axis:

$$h_{sim} = a + b \cdot \Delta z_{AFM} \tag{5.9}$$

where h_{sim} denotes the height of the simulation slice above the sample surface (the z-position at which the simulation is evaluated), and Δz_{AFM} denotes the AFM constant-z setpoint used during acquisition (the commanded tip–sample separation in the instrument's raw z-units).

For each line cut position, the simulation line cut at the closest available height h_{sim} is paired to each experimental line cut at its set-height Δz_{AFM}. Agreement is quantified by a weighted root-mean-square error (RMSE) computed over the lateral coordinate, with enhanced weight within ± 0.5 µm of the experimental peak center to emphasize agreement of the peak region. The offset a that minimizes the average weighted RMSE across all included heights is selected as the best alignment for that line cut position. No amplitude scaling of the curves is applied, only the height mapping is adjusted through a with fixed b. This procedure is repeated for each lateral position to generate the comparisons shown in Figure 5.9c.

Figure 5.9a displays measurement data at Δz =136 nm and Figure 5.9b the best matching simulation data from the line cuts at a tip-sample distance of 500 nm. Figure 5.9c shows three representative line cuts at offsets -0.25 µm, 0 µm, and 0.25 µm, comparing simulation and measurement across multiple heights. The overall similarity in shape between measurements and simulations supports the interpretation of the data as real electrostatic potential maps. Deviations are most apparent at smallest Δz, where the measured peaks are lower than predicted.

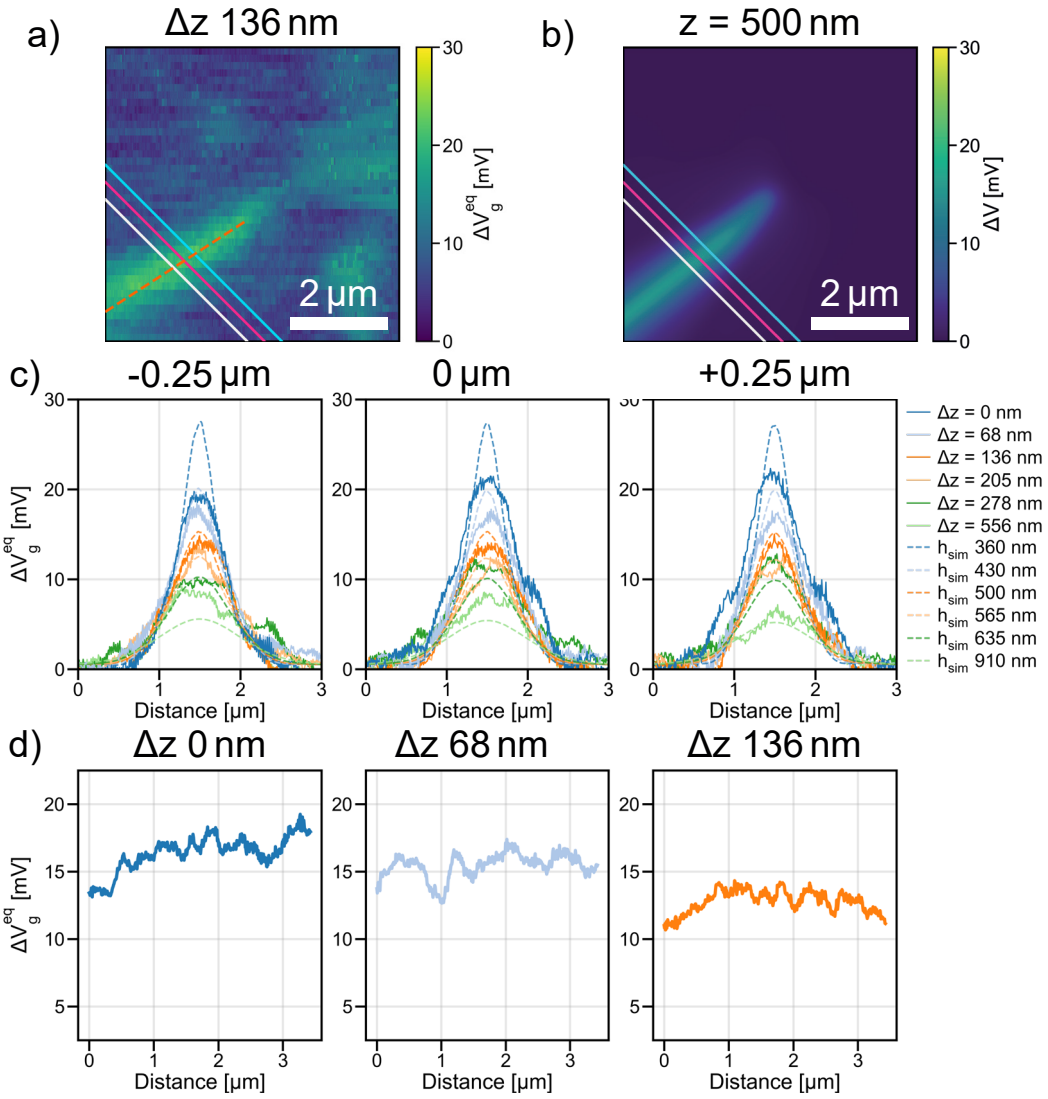

Figure 5.9: Comparison of experiment and simulation for the one-gate configuration. **a)** ΔV_g^{eq}, measured at Δz =136 nm. Solid lines indicate line cut positions used in c), and the dotted line indicates the position used in d). **b)** Corresponding simulated electrostatic potential at 500 nm tip-sample distance. **c)** Line cuts at offset −0.25 µm (white), 0 µm (pink), and 0.25 µm (blue), comparing experimental data across several heights with simulation slices. **d)** A line cut taken along the gate axis for different heights, showing the signal amplitude increase along more positive x values, most clearly for Δz =0 nm.

The quantitative mismatch is most plausibly attributed to limitations of the electrostatic model. In the simulations, the device geometry is idealized with sharp gate edges, nominal widths, and a simplified representation of the cantilever as a thin grounded plane placed a fixed distance above the slice. This treatment underestimates three-dimensional screening by the cantilever body, gates, and other nearby metallic structures, which probably divert field lines and reduce the potential at the dot. Consequently, the simulation maps should be interpreted as qualitative references for the spatial layout of features and their QD-sample distance dependence (height), rather than an absolute prediction of peak amplitude.

The best agreement between simulation and measurement line cuts assigns $\Delta z = 0\,\mathrm{nm}$ to a simulated QD-sample height of 360 nm near 0 µm offsets. This is consistent with the minimal feasible separation of $\sim$260 nm imposed by the QD setback and the SiN_x height.

Agreement degrades progressively toward negative offsets, where the measurement shows reduced peak heights (see Figure 5.9d). This trend is consistent with the lateral variation of the true tip-sample spacing imposed by the sample x-tilt mentioned in Section 5.3.1. Moving to negative x increases the spacing, reducing the capacitive coupling, and thus explaining the under-response of the peak height relative to the simulation.

In summary, the observed discrepancies are possibly due to limitations of the electrostatic model and a lateral spacing gradient that strengthens the response toward positive x and weakens it toward negative x. Residual differences may also reflect drift and lateral misalignment. Absolute height estimates from this comparison should therefore be treated with caution. Consequently, agreement is best near the central offset and deteriorates at larger offsets.

For the two-gate configuration, electrostatic simulations are performed in the same manner as for the one-gate case, with the difference that one sample gate is biased at 1 V and the other at $-1\,\mathrm{V}$. The resulting simulated potential maps exhibit two peaks of equal magnitude but opposite polarity (see Figure 5.10b), as expected from symmetry. When comparing to the experimental data, however, such a one-to-one correspondence cannot be established. As illustrated in Figure 5.10c, the measured line cuts reveal a negative peak of reduced amplitude compared to its positive counterpart. This asymmetry is most pronounced for line cuts taken at negative lateral offsets, whereas cuts closer to the front of the gates yield more balanced peak amplitudes.

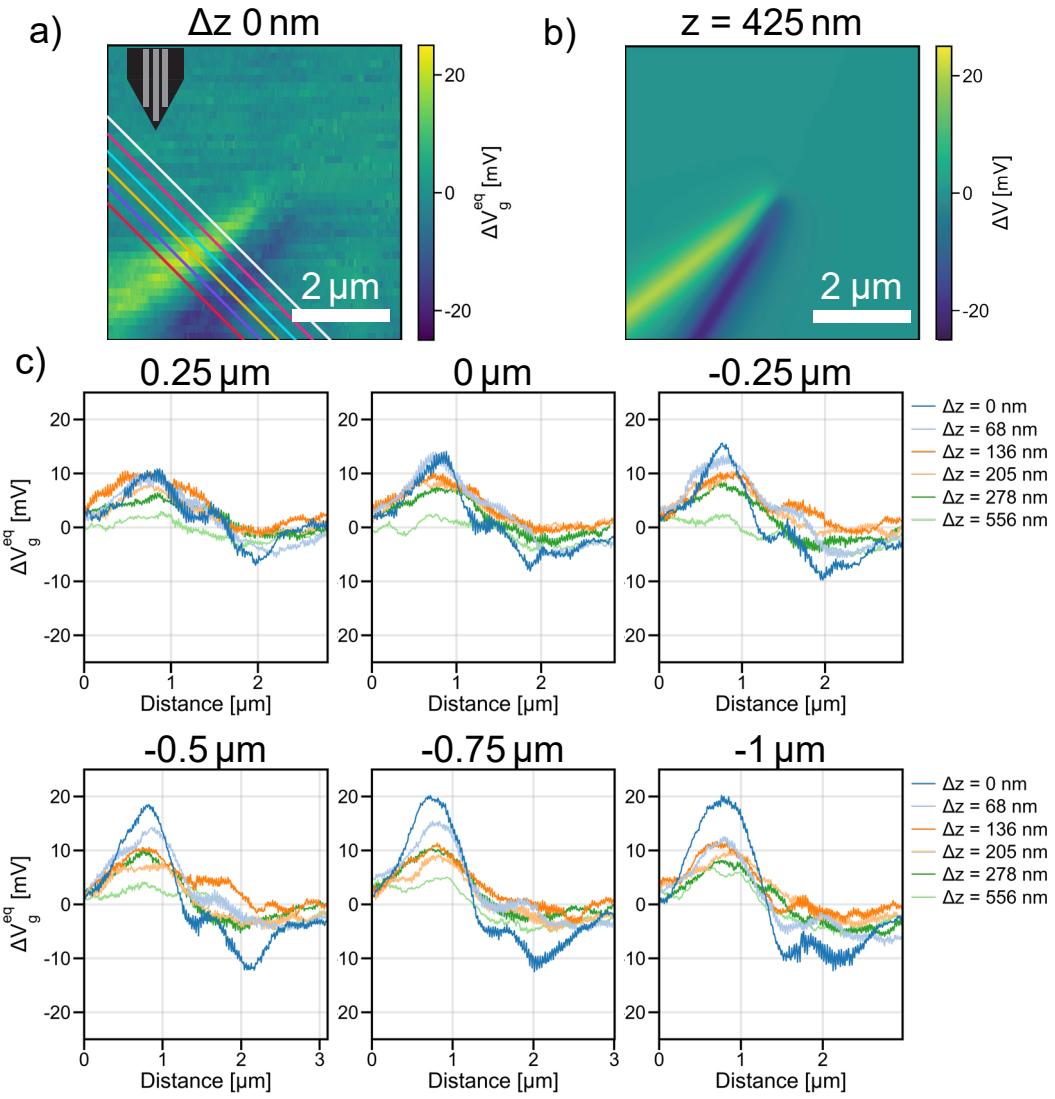

Figure 5.10: Two-gate scan with the NWQD lever. **a)** Response map of lever NWQD recorded at Δz =0 nm, showing the electrostatic potential map induced by a 1 V bias on the middle left gate and a −1 V bias on the lower left gate. Colored lines indicate the position of line cuts, spaced in 0.25 µm steps, with the red line corresponding to an offset of −1 µm. The orientation of the cantilever tip and its electrode traces are indicated at the upper left. **b)** Corresponding simulated electrostatic potential at 425 nm tip-sample distance. **c)** Line cuts extracted at the indicated offsets for several heights (one trace per Δz)

A possible reason for the amplitude imbalance between the 1 V and −1 V peaks is unequal local lever arms between the dot and the two sample gates. The cantilever

orientation and sample x-tilt can increase the effective overlap to the 1 V gate along the negative-offset cuts. A possible consequence is a larger local lever arm to the 1 V gate, i.e., $\alpha_+(1\,\mathrm{V\ gate}) > \alpha_-(-1\,\mathrm{V\ gate})$. In this case, even when the sensor is positioned above the −1 V gate, residual coupling to the 1 V gate produces a superposed shift $\Delta V_g^{eq} \propto \alpha_+ - \alpha_-$, reducing the apparent magnitude of the negative response. This mechanism is consistent with the offset dependence of the asymmetry. To test this hypothesis, one could swap the gate polarities while holding the height, scan path, and working point fixed. If lever arm asymmetry is responsible, the peak imbalance should invert.

Conclusion

This experiment demonstrates that an NWQD integrated on a commercial NC-AFM cantilever can be operated as a scanning probe for charge and electrostatic potential. Coulomb oscillations and diamonds verify the functionality of the tip device. Constant-z scans reveal spatially varying electrostatic potential induced by biased sample gates, and comparison with simulations confirms qualitative agreement. Lessons learned include the importance of switching off the interferometer laser to suppress noise, the sensitivity of lever-arm coupling to tip-sample geometry, and the limitations of simplified simulation models. Together, these results provide strong proof-of-concept for NWQD levers as scanning charge sensors, while also highlighting areas for future optimization in device stability, noise suppression, and simulation fidelity.

5.4 Comparative Discussion

The proof-of-concept experiments establish that both multi-gate and NWQD levers can be integrated into a cryogenic scanning probe system and operated as active device platforms. In addition to demonstrating complementary functionality with distinct advantages and limitations, the measurements verify that the scanning probe hardware, grounding and biasing scheme enable stable operation of sensitive and damage-prone devices without observable discharge or spike-related failure of either sensor or sample. Furthermore, the electron temperature extracted from Coulomb diamonds analysis indicates effective electronic thermalization of the sample at the scanning probe head.

The multi-gate levers demonstrate robust and reproducible operation as movable local gates. Constant-z scans on bare InAs NW directly visualize gate-induced conductance modulations, while experiments on InAs/InP NWQD establish that lever gates can tune QD states, generate equipotential contours, and even induce full Coulomb diamonds. These results confirm the viability of lithographically

defined cantilever gates for scanning gate microscopy. Limitations include the partial functionality of fabricated gates, with two of five gates showing negligible coupling, and the presence of noise with the interferometer laser on. Improvements in gate insulation and laser management are therefore essential for stable operation and future experiments.

The NWQD levers introduce charge sensing at the cantilever tip. Coulomb oscillations and diamonds verify the functionality of the tip QD, and intrinsic sensitivities in the $10^{-3}\,\mathrm{e}/\sqrt{\mathrm{Hz}}$ range are extracted and show that the main noise limiting the sensitivity is currently 1/f noise. Constant-z scans map gate-induced electrostatic potentials above the sample and show qualitative agreement with electrostatic simulations. A reversed-plunger configuration highlights the complementarity of the two platforms, in which the lever-QD sensed a gate potential from the sample rather than vice versa. At the same time, the NWQD approach is found to be fragile. The lever-QD is sensitive to optical readout noise, susceptible to mechanical crashes, and exhibits strong dependence on fabrication quality, particularly contact annealing.

Two additional exploratory attempts underline both the potential and the challenges of the platform. In one experiment, a coupled double-dot system is targeted by combining a lever-QD with a bare InAs NW. Stable dot formation in the sample is not achieved, and the lever device is likely damaged during approach, although no structural damage is visible in SEM inspection. In a second attempt, a dual-dot system is realized using an NWQD lever above an InAs/InP sample QD. Both dots exhibit Coulomb oscillations, and Coulomb diamonds of the sample QD are successfully recorded. However, the lever-QD suffers from excessive noise, attributed to over-annealed contacts, which prevents stable operation on the flank of a Coulomb peak. This issue is subsequently mitigated by improved annealing protocols. Despite their limitations, both experiments point toward the feasibility of coupled QD architectures involving NWQD levers, a promising direction for future work.

Taken together, the two lever types are complementary: the multi-gate lever reliably delivers controllable local electrostatic fields, whereas the NWQD levers provide quantitative charge sensing at the tip apex but demands improvements in stability and noise, most critically, a reduction of 1/f noise. These results lay the groundwork for integrated scanning charge sensors and coupled QD architectures and beyond the immediate demonstrations, the multi-gate approach paves the way towards non-destructive local induction of QDs in situ.

Chapter 6

Summary and Outlook

This thesis develops and validates a cryogenic scanning probe platform in which a NC-AFM cantilever is functionalized with nanoscale electronic devices at its apex. Two complementary tip concepts are realized: multi-gate levers that act as movable local electrodes, and NWQD levers that operate as scanning charge sensors. The work spans device physics, nanofabrication, and low-temperature instrumentation, culminating in proof-of-concept experiments that connect directly to the ambitions set in the introduction: spatially resolved, local electronic control and readout with a scanning probe cantilever.

Chapter 2 establishes the theoretical basis for a scanning QD charge sensor. Quantum confinement, charging energy, and electrochemical potentials are introduced to explain Coulomb blockade, oscillations, and diamonds as diagnostic transport signatures. The charge-sensing principle is defined by biasing the QD on a Coulomb-peak flank, where small nearby charge variations shift the resonance and yield measurable current changes. Charge sensitivity and gate-referred voltage sensitivity are defined and fundamental noise mechanisms (shot, Johnson-Nyquist, 1/f) summarized. These set quantitative targets for the design and for later comparison with the experiment. Furthermore, the two tip architectures are motivated and the NWQD sensor is compared to other possible charge sensing candidates.

To realize stable, low-noise operation, Chapter 3 describes the liquid He cryostat with a custom scanning probe insert that delivers stable, low-noise conditions for cryogenic scanning probe experiments. The insert uses staged radiation shields, gold-plated thermal anchors, and a spring-suspended head where the cantilever stays fixed while the sample is moved by nanopositioners and piezo scanners. Cabling is split into high-voltage piezo lines and low-noise measurement bundles with dedicated shielding, star-grounding, and RC filters at base temperature to suppress spikes and protect devices. A fiber interferometer provides deflection readout. An FPGA scanning probe microscopy controller synchronizes scan, actuation, and data and RF-ready coax lines and cryo components prepare the platform for reflectometry. The workflow proceeds from RT alignment and laser lock to vacuum precool, LHe cooldown, PLL-assisted approach, and constant-z scanning.

In Chapter 4 commercial NC-ATEC are converted into device platforms by FIB-milling a flat plateau at the tip, CO_2-snow cleaning, and conformal ALD Al_2O_3 insulation, followed by rear bonding pads deposited through a silicon shadow mask. A floating-PMMA transfer scheme replaces spin coating, giving uniform resist coverage over the 3D tip and enabling both positive- and negative-tone EBL with sub-100 nm features. Multi-gate levers are realized by depositing a thin Au base from pads to the apex, writing the gate pattern in PMMA, transferring pattern into Au by Ar IBE, and removing the resist to yield five isolated gates. NWQD levers are assembled by first fabricating contacted InAs/InP NWQDs on suspended

SiN_x membranes, releasing triangular devices, transferring them onto the cantilever plateau, and wiring them to the pads by on-lever EBL and lift-off. Forming-gas annealing stabilizes contacts and reduces low-frequency noise. A thin Au coating on the lever backside improves optical reflectance for interferometric readout.

Chapter 5 closes the loop with calibration and first measurements. Scanner calibration is performed in situ. In-plane scale factors come from AFM images of lithographic markers, while the z-piezo is calibrated interferometrically and is found to be linear with a 2.73 correction factor. Multi-gate levers modulate current in a bare InAs NW and generate equipotential rings and Coulomb diamonds in an InAs/InP NWQD when used as a movable plunger, establishing constant-z operation as essential, because gate biases shift the cantilever resonance. NWQD levers are verified by Coulomb diamonds. Measurements reveal strong laser-induced noise, so current readout measurements are done with the laser off. Intrinsic white noise reaches the low $10^{-5}\,\mathrm{e}/\sqrt{\mathrm{Hz}}$ range, but DC 1/f noise dominates, giving total sensitivities around $10^{-3}\,\mathrm{e}/\sqrt{\mathrm{Hz}}$ and gate-referred sensitivities of a few $10^{-2}\,\mathrm{V}/\sqrt{\mathrm{Hz}}$ in a reversed-plunger geometry. At this sensitivity, mV-scale contrasts are detectable with practical averaging. Constant-z scans above one and two biased gates yield electrostatic maps that agree qualitatively with simulations.

The introduction frames a goal: to combine the spatial versatility of AFM with the exquisite charge sensitivity of QDs to image and control nanoscale electronic landscapes. Chapters 3-5 realizes the essential ingredients: platform, devices, and first measurements. The multi-gate lever shows that the sensor can actively shape local potentials, while the NWQD lever shows that the tip can read out local electrostatics quantitatively that compares with simulations. Taken together, the system and sensors developed throughout this work provides a starting platform to explore local gating via the multi-gate lever and charge sensing via the NWQD lever as separate, complementary scanning probes.

The immediate next steps follow directly from the identified limitations in fabrication, instrumentation, and measurement methodology. On the fabrication side, oxide reliability should be improved to ensure that all five gates of the multi-gate lever operate reproducibly. It would be advantageous if commercial cantilevers were supplied with a defined plateau at the tip and with a pre-deposited insulating layer. This yields greater geometric consistency and should increase fabrication yield. As an alternative path, scanning with flat levers should be explored, as flat levers are expected to simplify fabrication, reduce processing time, and increase yield. Moreover, with the NWQD device integrated on a 50 nm SiN_x membrane, an effective tip height of 50 nm is already provided. In parallel, stiffer levers should be adopted to limit bending under tip–sample forces. For levers without a tip, higher stiffness would also lowers the risk of snap-in. For the NWQD lever, the QD should

be positioned closer to the mechanical apex. This may require an NW in which the tunnel-barrier-defined dot is located closer to the seeded end, thereby reducing the axial setback between the dot and the tip.

For the scanning probe platform, the x-y calibration should be refined beyond a scale factor by incorporating piezo nonlinearity. A quantitative assessment of z-axis drift, creep under constant-z operation, and the repeatability of returning to a given z-setpoint is needed, together with corresponding software compensation. The dominant 1/f noise should be reduced by moving to AC lock-in detection for DC transport signals or by implementing the already wired RF reflectometry path for the lever sensor. Thermal referencing can be improved by relocating the temperature sensor closer to the sample region on the head.

Measurement practice should likewise be tightened. Rather than defining constant-z by a fixed piezo extension, a local height plane should be computed from the AFM topography and used as the z-setpoint during signal acquisition. This plane-following approach would maintain a more constant tip-sample spacing across the scan range and reduce systematic variation in capacitive coupling.

With respect to target systems, samples that enable lever-induced confinement should be prioritized. A shallow 2DEG would provide an ideal testbed for inducing a QD with the multi-gate lever. Alternatively, very stable NWs without built-in tunnel barriers could be used to explore lever-defined dots in one dimension. For charge sensing, a coupled-dot geometry, one dot on the sample and one on the lever, should be revisited to detect single-electron hopping events between well-controlled charge states, this time with improved noise performance.

Looking further ahead, the platform could be adapted to probe noise mechanisms in qubit devices. With reduced 1/f noise and RF reflectometry readout in place, a calibrated charge sensor rastered above operating qubits during synchronized spectroscopy would enable spatial maps of low-frequency charge noise. Therefore allowing localization of dominant fluctuators and quantification of their coupling. In dispersive mode, RF reflectometry of the lever sensor could be combined with pulsed gating of the device under test to perform time-resolved noise spectroscopy, distinguishing equilibrium 1/f backgrounds from drive-induced hotspots. Such measurements would provide actionable targets for materials and process optimization and could ultimately be extended to wafer-level screening of candidate stacks prior to qubit fabrication.

With these advances, the platform outlined here can evolve from proof-of-concept into a broadly useful tool for quantum-materials and device imaging, completing the arc set out at the start: better imaging, deeper insight.

Bibliography

[1] Gerd Binnig, Calvin F Quate, and Ch Gerber. "Atomic force microscope". In: *Physical review letters* 56.9 (1986), p. 930 (cit. on p. 2).

[2] Thomas R Albrecht, Peter Grütter, David Horne, and Daniel Rugar. "Frequency modulation detection using high-Q cantilevers for enhanced force microscope sensitivity". In: *Journal of applied physics* 69.2 (1991), pp. 668–673 (cit. on p. 2).

[3] Franz J Giessibl. "Advances in atomic force microscopy". In: *Reviews of modern physics* 75.3 (2003), p. 949 (cit. on pp. 2, 15, 16).

[4] David P DiVincenzo. "The physical implementation of quantum computation". In: *Fortschritte der Physik: Progress of Physics* 48.9-11 (2000), pp. 771–783 (cit. on p. 2).

[5] Daniel Loss and David P DiVincenzo. "Quantum computation with quantum dots". In: *Physical Review A* 57.1 (1998), p. 120 (cit. on p. 2).

[6] RJ Schoelkopf, P Wahlgren, AA Kozhevnikov, P Delsing, and DE Prober. "The radio-frequency single-electron transistor (RF-SET): A fast and ultrasensitive electrometer". In: *science* 280.5367 (1998), pp. 1238–1242 (cit. on pp. 2, 12, 13, 15).

[7] JM Elzerman, R Hanson, LH Willems van Beveren, B Witkamp, LMK Vandersypen, and Leo P Kouwenhoven. "Single-shot read-out of an individual electron spin in a quantum dot". In: *nature* 430.6998 (2004), pp. 431–435 (cit. on p. 2).

[8] Ronald Hanson, Leo P Kouwenhoven, Jason R Petta, Seigo Tarucha, and Lieven MK Vandersypen. "Spins in few-electron quantum dots". In: *Reviews of modern physics* 79.4 (2007), pp. 1217–1265 (cit. on p. 2).

[9] MJ Yoo, TA Fulton, HF Hess, RL Willett, LN Dunkleberger, RJ Chichester, LN Pfeiffer, and KW West. "Scanning single-electron transistor microscopy: Imaging individual charges". In: *Science* 276.5312 (1997), pp. 579–582 (cit. on pp. 2, 18, 19, 21).

[10] Jens Martin, Nitzan Akerman, G Ulbricht, T Lohmann, JH v Smet, K Von Klitzing, and Amir Yacoby. "Observation of electron–hole puddles in graphene using a scanning single-electron transistor". In: *Nature physics* 4.2 (2008), pp. 144–148 (cit. on pp. 2, 18).

[11] Maayan Honig, Joseph A Sulpizio, Jonathan Drori, Arjun Joshua, Eli Zeldov, and Shahal Ilani. "Local electrostatic imaging of striped domain order in LaAlO3/SrTiO3". In: *Nature materials* 12.12 (2013), pp. 1112–1118 (cit. on pp. 2, 18, 19, 88).

[12] Lior Ella et al. "Simultaneous voltage and current density imaging of flowing electrons in two dimensions". In: *Nature nanotechnology* 14.5 (2019), pp. 480–487 (cit. on pp. 2, 18, 19, 90).

[13] Joseph A Sulpizio et al. "Visualizing Poiseuille flow of hydrodynamic electrons". In: *Nature* 576.7785 (2019), pp. 75–79 (cit. on pp. 2, 18, 19).

[14] I Shapir, A Hamo, S Pecker, CP Moca, Ö Legeza, G Zarand, and S Ilani. "Imaging the electronic Wigner crystal in one dimension". In: *Science* 364.6443 (2019), pp. 870–875 (cit. on pp. 2, 18, 19).

[15] Marc A Kastner. "Artificial atoms". In: *Physics today* 46.1 (1993), pp. 24–31 (cit. on p. 6).

[16] F Pelayo García de Arquer, Dmitri V Talapin, Victor I Klimov, Yasuhiko Arakawa, Manfred Bayer, and Edward H Sargent. "Semiconductor quantum dots: Technological progress and future challenges". In: *Science* 373.6555 (2021), eaaz8541 (cit. on p. 6).

[17] Floris A Zwanenburg, Andrew S Dzurak, Andrea Morello, Michelle Y Simmons, Lloyd CL Hollenberg, Gerhard Klimeck, Sven Rogge, Susan N Coppersmith, and Mark A Eriksson. "Silicon quantum electronics". In: *Reviews of modern physics* 85.3 (2013), pp. 961–1019 (cit. on pp. 6–8).

[18] A Paul Alivisatos. "Semiconductor clusters, nanocrystals, and quantum dots". In: *science* 271.5251 (1996), pp. 933–937 (cit. on p. 6).

[19] Frederick S Thomas et al. "Highly symmetric and tunable tunnel couplings in InAs/InP nanowire heterostructure quantum dots". In: *Nanotechnology* 31.13 (2020), p. 135003 (cit. on pp. 6, 67).

[20] Malin Nilsson, Luna Namazi, Sebastian Lehmann, Martin Leijnse, Kimberly A Dick, and Claes Thelander. "Electron-hole interactions in coupled InAs-GaSb quantum dots based on nanowire crystal phase templates". In: *Physical Review B* 94.11 (2016), p. 115313 (cit. on p. 6).

[21] Tsuneya Ando, Alan B Fowler, and Frank Stern. "Electronic properties of two-dimensional systems". In: *Reviews of Modern Physics* 54.2 (1982), p. 437 (cit. on p. 6).

[22] Leo P Kouwenhoven, Charles M Marcus, Paul L McEuen, Seigo Tarucha, Robert M Westervelt, and Ned S Wingreen. "Electron transport in quantum dots". In: *Mesoscopic electron transport*. Springer, 1997, pp. 105–214 (cit. on pp. 6–8).

[23] Guido Burkard, Thaddeus D Ladd, Andrew Pan, John M Nichol, and Jason R Petta. "Semiconductor spin qubits". In: *Reviews of Modern Physics* 95.2 (2023), p. 025003 (cit. on pp. 7, 8).

[24] Carlo WJ Beenakker. "Theory of Coulomb-blockade oscillations in the conductance of a quantum dot". In: *Physical Review B* 44.4 (1991), p. 1646 (cit. on pp. 7, 8).

[25] Lina Su, Xinxing Li, Hua Qin, and Xiaofeng Gu. "A sensitive charge scanning probe based on silicon single electron transistor". In: *Journal of Semiconductors* 37.4 (2016), p. 044008 (cit. on pp. 9, 18, 19, 86–89).

[26] DV Averin and KK Likharev. "Coulomb blockade of single-electron tunneling, and coherent oscillations in small tunnel junctions". In: *Journal of low temperature physics* 62.3 (1986), pp. 345–373 (cit. on p. 9).

[27] Konstantin K Likharev. "Single-electron devices and their applications". In: *Proceedings of the IEEE* 87.4 (2002), pp. 606–632 (cit. on pp. 9, 10).

[28] David Berman, Nikolai B Zhitenev, Raymond C Ashoori, Henry I Smith, and Michael R Melloch. "Single-electron transistor as a charge sensor for semiconductor applications". In: *Journal of Vacuum Science & Technology B: Microelectronics and Nanometer Structures Processing, Measurement, and Phenomena* 15.6 (1997), pp. 2844–2847 (cit. on pp. 9, 10).

[29] Thomas Ihn et al. "Quantum dots investigated with charge detection techniques". In: *Solid State Communications* 149.35-36 (2009), pp. 1419–1426 (cit. on p. 10).

[30] Haruki Kiyama, Alexander Korsch, Naomi Nagai, Yasushi Kanai, Kazuhiko Matsumoto, Kazuhiko Hirakawa, and Akira Oiwa. "Single-electron charge sensing in self-assembled quantum dots". In: *Scientific reports* 8.1 (2018), p. 13188 (cit. on p. 10).

[31] Takashi Nakajima, Yohei Kojima, Yoshihiro Uehara, Akito Noiri, Kenta Takeda, Takashi Kobayashi, and Seigo Tarucha. "Real-time feedback control of charge sensing for quantum dot qubits". In: *Physical Review Applied* 15.3 (2021), p. L031003 (cit. on p. 10).

[32] SM Patomäki et al. “Elongated quantum dot as a distributed charge sensor”. In: *Physical Review Applied* 21.5 (2024), p. 054042 (cit. on p. 10).

[33] J Güttinger, C Stampfer, S Hellmüller, F Molitor, T Ihn, and K Ensslin. “Charge detection in graphene quantum dots”. In: *Applied Physics Letters* 93.21 (2008) (cit. on p. 10).

[34] R Schleser, E Ruh, T Ihn, K Ensslin, DC Driscoll, and AC Gossard. “Time-resolved detection of individual electrons in a quantum dot”. In: *Applied physics letters* 85.11 (2004), pp. 2005–2007 (cit. on pp. 10, 21).

[35] LMK Vandersypen, JM Elzerman, RN Schouten, LH Willems van Beveren, R Hanson, and Leo P Kouwenhoven. “Real-time detection of single-electron tunneling using a quantum point contact”. In: *Applied Physics Letters* 85.19 (2004), pp. 4394–4396 (cit. on p. 10).

[36] Yongjie Hu, Hugh OH Churchill, David J Reilly, Jie Xiang, Charles M Lieber, and Charles M Marcus. “A Ge/Si heterostructure nanowire-based double quantum dot with integrated charge sensor”. In: *Nature nanotechnology* 2.10 (2007), pp. 622–625 (cit. on p. 10).

[37] Akito Noiri, Kenta Takeda, Jun Yoneda, Takashi Nakajima, Tetsuo Kodera, and Seigo Tarucha. “Radio-frequency-detected fast charge sensing in undoped silicon quantum dots”. In: *Nano Letters* 20.2 (2020), pp. 947–952 (cit. on pp. 10, 13–15).

[38] H Geng et al. “High-fidelity sub-microsecond single-shot electron spin readout above 3.5 K”. In: *Nature Communications* 16.1 (2025), p. 3382 (cit. on p. 10).

[39] Santiago Serrano et al. “Improved single-shot qubit readout using twin rf-SET charge correlations”. In: *PRX Quantum* 5.1 (2024), p. 010301 (cit. on p. 10).

[40] Joseph Hickie, Barnaby Van Straaten, Federico Fedele, Daniel Jirovec, Andrea Ballabio, Daniel Chrastina, Giovanni Isella, Georgios Katsaros, and Natalia Ares. “Automated long-range compensation of an rf quantum dot sensor”. In: *Physical Review Applied* 22.6 (2024), p. 064026 (cit. on p. 10).

[41] Florian Vigneau, Federico Fedele, Anasua Chatterjee, David Reilly, Ferdinand Kuemmeth, M Fernando Gonzalez-Zalba, Edward Laird, and Natalia Ares. “Probing quantum devices with radio-frequency reflectometry”. In: *Applied Physics Reviews* 10.2 (2023) (cit. on pp. 11, 13–15).

[42] Julien Basset, Anna Stockklauser, D-D Jarausch, Tobias Frey, Christian Reichl, Werner Wegscheider, Andreas Wallraff, Klaus Ensslin, and Thomas Ihn. “Evaluating charge noise acting on semiconductor quantum dots in the circuit quantum electrodynamics architecture”. In: *Applied Physics Letters* 105.6 (2014) (cit. on pp. 11, 12).

[43] Michel H Devoret and Robert J Schoelkopf. "Amplifying quantum signals with the single-electron transistor". In: *Nature* 406.6799 (2000), pp. 1039–1046 (cit. on p. 11).

[44] A Aassime, D Gunnarsson, K Bladh, P Delsing, and R Schoelkopf. "Radio-frequency single-electron transistor: Toward the shot-noise limit". In: *Applied physics letters* 79.24 (2001), pp. 4031–4033 (cit. on p. 11).

[45] Md Zahid Hossain, Sergey L Rumyantsev, Khan MF Shahil, Desalegne Teweldebrhan, Michael Shur, and Alexander A Balandin. "Low-frequency current fluctuations in "graphene-like" exfoliated thin-films of bismuth selenide topological insulators". In: *ACS nano* 5.4 (2011), pp. 2657–2663 (cit. on p. 12).

[46] Elliot J Connors, JJ Nelson, Haifeng Qiao, Lisa F Edge, and John M Nichol. "Low-frequency charge noise in Si/SiGe quantum dots". In: *Physical Review B* 100.16 (2019), p. 165305 (cit. on pp. 12, 55).

[47] John Bertrand Johnson. "Thermal agitation of electricity in conductors". In: *Physical review* 32.1 (1928), p. 97 (cit. on p. 12).

[48] Harry Nyquist. "Thermal agitation of electric charge in conductors". In: *Physical review* 32.1 (1928), p. 110 (cit. on p. 12).

[49] SJ Angus, AJ Ferguson, AS Dzurak, and RG Clark. "A silicon radio-frequency single electron transistor". In: *Applied Physics Letters* 92.11 (2008) (cit. on pp. 12, 20, 21).

[50] Imtiaz Ahmed et al. "Radio-frequency capacitive gate-based sensing". In: *Physical Review Applied* 10.1 (2018), p. 014018 (cit. on p. 12).

[51] N Ares et al. "Sensitive radio-frequency measurements of a quantum dot by tuning to perfect impedance matching". In: *Physical Review Applied* 5.3 (2016), p. 034011 (cit. on p. 13).

[52] MC Cassidy, AS Dzurak, RG Clark, KD Petersson, I Farrer, DA Ritchie, and CG Smith. "Single shot charge detection using a radio-frequency quantum point contact". In: *Applied Physics Letters* 91.22 (2007) (cit. on pp. 14, 15, 20, 21).

[53] DJ Reilly, CM Marcus, MP Hanson, and AC Gossard. "Fast single-charge sensing with a rf quantum point contact". In: *Applied Physics Letters* 91.16 (2007) (cit. on p. 15).

[54] SJ Chorley, J Wabnig, ZV Penfold-Fitch, KD Petersson, J Frake, CG Smith, and MR Buitelaar. "Measuring the complex admittance of a carbon nanotube double quantum dot". In: *Physical review letters* 108.3 (2012), p. 036802 (cit. on p. 15).

[55] Edward J Thomas et al. “Rapid cryogenic characterization of 1,024 integrated silicon quantum dot devices”. In: *Nature Electronics* 8.1 (2025), pp. 75–83 (cit. on p. 15).

[56] Fangzhou Xia and Kamal Youcef-Toumi. “Advanced atomic force microscopy modes for biomedical research”. In: *Biosensors* 12.12 (2022), p. 1116 (cit. on p. 16).

[57] Fangzhou Xia, James Quigley, Xiaotong Zhang, Chen Yang, Yi Wang, and Kamal Youcef-Toumi. “A modular low-cost atomic force microscope for precision mechatronics education”. In: *Mechatronics* 76 (2021), p. 102550 (cit. on p. 16).

[58] Yves F Dufrêne, Toshio Ando, Ricardo Garcia, David Alsteens, David Martinez-Martin, Andreas Engel, Christoph Gerber, and Daniel J Müller. “Imaging modes of atomic force microscopy for application in molecular and cell biology”. In: *Nature nanotechnology* 12.4 (2017), pp. 295–307 (cit. on p. 17).

[59] Yoichi Miyahara, Antoine Roy-Gobeil, and Peter Grutter. “Quantum state readout of individual quantum dots by electrostatic force detection”. In: *Nanotechnology* 28.6 (2017), p. 064001 (cit. on p. 17).

[60] Paul Girard. “Electrostatic force microscopy: principles and some applications to semiconductors”. In: *Nanotechnology* 12.4 (2001), p. 485 (cit. on p. 17).

[61] A Yacoby, HF Hess, TA Fulton, LN Pfeiffer, and KW West. “Electrical imaging of the quantum Hall state”. In: *Solid state communications* 111.1 (1999), pp. 1–13 (cit. on p. 18).

[62] Jonah Waissman, Maayan Honig, Sharon Pecker, Avishai Benyamini, Assaf Hamo, and Shahal Ilani. “Realization of pristine and locally tunable one-dimensional electron systems in carbon nanotubes”. In: *Nature nanotechnology* 8.8 (2013), pp. 569–574 (cit. on pp. 18, 19, 89).

[63] L Gurevich, L Canali, and LP Kouwenhoven. “Scanning gate spectroscopy on nanoclusters”. In: *Applied Physics Letters* 76.3 (2000), pp. 384–386 (cit. on p. 18).

[64] MA Topinka, Brian J LeRoy, SEJ Shaw, EJ Heller, RM Westervelt, KD Maranowski, and AC Gossard. “Imaging coherent electron flow from a quantum point contact”. In: *Science* 289.5488 (2000), pp. 2323–2326 (cit. on p. 18).

[65] MA Topinka, BJ LeRoy, RM Westervelt, SEJ Shaw, R Fleischmann, EJ Heller, KD Maranowski, and AC Gossard. "Coherent branched flow in a two-dimensional electron gas". In: *Nature* 410.6825 (2001), pp. 183–186 (cit. on p. 18).

[66] Michael T Woodside and Paul L McEuen. "Scanned probe imaging of single-electron charge states in nanotube quantum dots". In: *Science* 296.5570 (2002), pp. 1098–1101 (cit. on p. 18).

[67] Ania C Bleszynski, Floris A Zwanenburg, RM Westervelt, Aarnoud L Roest, Erik PAM Bakkers, and Leo P Kouwenhoven. "Scanned probe imaging of quantum dots inside InAs nanowires". In: *Nano Letters* 7.9 (2007), pp. 2559–2562 (cit. on p. 19).

[68] Lynda Cockins, Yoichi Miyahara, Steven D Bennett, Aashish A Clerk, Sergei Studenikin, Philip Poole, Andrew Sachrajda, and Peter Grutter. "Energy levels of few-electron quantum dots imaged and characterized by atomic force microscopy". In: *Proceedings of the National Academy of Sciences* 107.21 (2010), pp. 9496–9501 (cit. on p. 19).

[69] Lynda Cockins, Yoichi Miyahara, Steven D Bennett, Aashish A Clerk, and Peter Grutter. "Excited-state spectroscopy on an individual quantum dot using atomic force microscopy". In: *Nano letters* 12.2 (2012), pp. 709–713 (cit. on p. 19).

[70] Hermann Sellier, Benoit Hackens, MG Pala, Frederico Martins, Samuel Baltazar, Xavier Wallart, Ludovic Desplanque, Vincent Bayot, and Serge Huant. "On the imaging of electron transport in semiconductor quantum structures by scanning-gate microscopy: successes and limitations". In: *Semiconductor science and technology* 26.6 (2011), p. 064008 (cit. on p. 19).

[71] Yun-Pil Shim, Rusko Ruskov, Hilary M Hurst, and Charles Tahan. "Induced quantum dot probe for material characterization". In: *Applied physics letters* 114.15 (2019) (cit. on pp. 19, 63).

[72] CC Williams, WP Hough, and SA Rishton. "Scanning capacitance microscopy on a 25 nm scale". In: *Applied physics letters* 55.2 (1989), pp. 203–205 (cit. on p. 20).

[73] Yves Martin, David W Abraham, and H Kumar Wickramasinghe. "High-resolution capacitance measurement and potentiometry by force microscopy". In: *Applied Physics Letters* 52.13 (1988), pp. 1103–1105 (cit. on p. 20).

[74] Albert K Henning, Todd Hochwitz, James Slinkman, James Never, Steven Hoffmann, Phil Kaszuba, and Charles Daghlian. "Two-dimensional surface dopant profiling in silicon using scanning Kelvin probe microscopy". In: *Journal of applied physics* 77.5 (1995), pp. 1888–1896 (cit. on p. 20).

[75] Henrik Brenning, Sergey Kafanov, Tim Duty, Sergey Kubatkin, and Per Delsing. "An ultrasensitive radio-frequency single-electron transistor working up to 4.2 K". In: *Journal of Applied Physics* 100.11 (2006) (cit. on pp. 20, 21).

[76] J Salfi, IG Savelyev, M Blumin, SV Nair, and HE Ruda. "Direct observation of single-charge-detection capability of nanowire field-effect transistors". In: *Nature nanotechnology* 5.10 (2010), pp. 737–741 (cit. on pp. 20, 22).

[77] AS Trifonov, DE Presnov, IV Bozhev, DA Evplov, V Desmaris, and VA Krupenin. "Non-contact scanning probe technique for electric field measurements based on nanowire field-effect transistor". In: *Ultramicroscopy* 179 (2017), pp. 33–40 (cit. on pp. 20, 22).

[78] Michael SJ Barson, Lachlan M Oberg, Liam P McGuinness, Andrej Denisenko, Neil B Manson, Jorg Wrachtrup, and Marcus W Doherty. "Nanoscale vector electric field imaging using a single electron spin". In: *Nano Letters* 21.7 (2021), pp. 2962–2967 (cit. on pp. 20, 22, 23).

[79] Christian Barthel, Morten Kjærgaard, J Medford, Michael Stopa, Charles Masamed Marcus, MP Hanson, and Arthur C Gossard. "Fast sensing of double-dot charge arrangement and spin state with a radio-frequency sensor quantum dot". In: *Physical Review B—Condensed Matter and Materials Physics* 81.16 (2010), p. 161308 (cit. on p. 21).

[80] WW Xue, B Davis, Feng Pan, J Stettenheim, TJ Gilheart, AJ Rimberg, and Z Ji. "On-chip matching networks for radio-frequency single-electron transistors". In: *Applied Physics Letters* 91.9 (2007) (cit. on p. 21).

[81] Prasanta Kumbhakar, Anusha Shanmugam, Chithra H Sharma, JL Reno, and Madhu Thalakulam. "Quantum point contact galvanically coupled to planar superconducting resonator: a shot-noise-limited broad-band electrical amplifier". In: *Quantum Science and Technology* 6.4 (2021), p. 045006 (cit. on p. 21).

[82] Florian Dolde et al. "Electric-field sensing using single diamond spins". In: *Nature Physics* 7.6 (2011), pp. 459–463 (cit. on p. 22).

[83] Davide Cadeddu, Mathieu Munsch, Nicola Rossi, J-M Gérard, Julien Claudon, Richard J Warburton, and Martino Poggio. "Electric-field sensing with a scanning fiber-coupled quantum dot". In: *Physical Review Applied* 8.3 (2017), p. 031002 (cit. on pp. 22, 23).

[84] Rafael S Eggli et al. "Cryogenic hyperabrupt strontium titanate varactors for sensitive reflectometry of quantum dots". In: *Physical Review Applied* 20.5 (2023), p. 054056 (cit. on p. 37).

[85] Alexander von Schmidsfeld, Tobias Nörenberg, Matthias Temmen, and Michael Reichling. "Understanding interferometry for micro-cantilever displacement detection". In: *Beilstein journal of nanotechnology* 7.1 (2016), pp. 841–851 (cit. on p. 41).

[86] M Stark, BN Bercu, Florence Marchi, Joel Chevrier, and Serge Huant. "Marking the difference: Interferometric detection vs optical beam deflection in afm". In: *AIP Conference Proceedings*. Vol. 696. 1. American Institute of Physics. 2003, pp. 385–391 (cit. on p. 41).

[87] Daniel Rugar, H Jonathon Mamin, and Peter Guethner. "Improved fiber-optic interferometer for atomic force microscopy". In: *Applied Physics Letters* 55.25 (1989), pp. 2588–2590 (cit. on p. 41).

[88] D Rugar, HJ Mamin, R Erlandsson, JE Stern, and BD Terris. "Force microscope using a fiber-optic displacement sensor". In: *Review of Scientific Instruments* 59.11 (1988), pp. 2337–2340 (cit. on p. 41).

[89] R Erlandsson, GM McClelland, CM Mate, and S Chiang. "Atomic force microscopy using optical interferometry". In: *Journal of Vacuum Science & Technology A: Vacuum, Surfaces, and Films* 6.2 (1988), pp. 266–270 (cit. on p. 41).

[90] Nicola Rossi, Floris R Braakman, Davide Cadeddu, Denis Vasyukov, Gözde Tütüncüoglu, Anna Fontcuberta i Morral, and Martino Poggio. "Vectorial scanning force microscopy using a nanowire sensor". In: *Nature nanotechnology* 12.2 (2017), pp. 150–155 (cit. on p. 41).

[91] Andriani Vervelaki, Kousik Bagani, Daniel Jetter, Manh-Ha Doan, Tuan K Chau, Boris Gross, Dennis V Christensen, Peter Bøggild, and Martino Poggio. "Visualizing thickness-dependent magnetic textures in few-layer Cr2Ge2Te6". In: *Communications Materials* 5.1 (2024), p. 40 (cit. on p. 41).

[92] A. Ruf, M. Abraham, J. Diebel, W. Ehrfeld, P. Guethner, M. Lacher, K. Mayr, and J. Reinhardt. "Integrated Fabry–Perot distance control for atomic force microscopy". In: *Journal of Vacuum Science & Technology B* 15.3 (1997), pp. 579–585 (cit. on p. 41).

[93] Luca Forrer, Aurèle Kamber, Armin Knoll, Martino Poggio, and FR Braakman. "Electron-beam lithography of nanostructures at the tips of scanning probe cantilevers". In: *AIP Advances* 13.3 (2023) (cit. on pp. 53, 59, 60, 62, 63).

[94] Feridun Ay. "INVESTIGATION OF FOCUSED ION BEAM IMPLANTATION PROFILE OF Ga+ IONS FOR APPLICATIONS IN SILICON PHOTONICS". In: *Eskişehir Technical University Journal of Science and Technology A-Applied Sciences and Engineering* 19.4 (2018), pp. 976–981 (cit. on p. 54).

[95] YJ Xiao, FZ Fang, ZW Xu, W Wu, and XC Shen. "The study of Ga+ FIB implanting crystal silicon and subsequent annealing". In: *Nuclear Instruments and Methods in Physics Research Section B: Beam Interactions with Materials and Atoms* 307 (2013), pp. 253–256 (cit. on p. 54).

[96] Brian Paquelet Wuetz et al. "Reducing charge noise in quantum dots by using thin silicon quantum wells". In: *Nature communications* 14.1 (2023), p. 1385 (cit. on p. 55).

[97] Robert Sherman, John Grob, and Walter Whitlock. "Dry surface cleaning using CO2 snow". In: *Journal of Vacuum Science & Technology B: Microelectronics and Nanometer Structures Processing, Measurement, and Phenomena* 9.4 (1991), pp. 1970–1977 (cit. on p. 55).

[98] Richard W Johnson, Adam Hultqvist, and Stacey F Bent. "A brief review of atomic layer deposition: from fundamentals to applications". In: *Materials today* 17.5 (2014), pp. 236–246 (cit. on p. 56).

[99] Nagarajan Ranganathan, Da Yong Lee, Liu Youhe, Guo-Qiang Lo, Krishnamachar Prasad, and Kin Leong Pey. "Influence of Bosch etch process on electrical isolation of TSV structures". In: *IEEE Transactions on components, packaging and manufacturing technology* 1.10 (2011), pp. 1497–1507 (cit. on p. 57).

[100] Christophe Vieu, F Carcenac, A Pepin, Y Chen, M Mejias, A Lebib, L Manin-Ferlazzo, L Couraud, and H Launois. "Electron beam lithography: resolution limits and applications". In: *Applied surface science* 164.1-4 (2000), pp. 111–117 (cit. on p. 58).

[101] J Linden, Ch Thanner, B Schaaf, S Wolff, B Lägel, and E Oesterschulze. "Spray coating of PMMA for pattern transfer via electron beam lithography on surfaces with high topography". In: *Microelectronic engineering* 88.8 (2011), pp. 2030–2032 (cit. on p. 59).

[102] Anpan Han, Aaron Kuan, Jene Golovchenko, and Daniel Branton. "Nanopatterning on nonplanar and fragile substrates with ice resists". In: *Nano letters* 12.2 (2012), pp. 1018–1021 (cit. on p. 59).

[103] Jian Zhang, Celal Con, and Bo Cui. "Electron beam lithography on irregular surfaces using an evaporated resist". In: *ACS nano* 8.4 (2014), pp. 3483–3489 (cit. on p. 59).

[104] Madeleine Nilsen, Fabian Port, Michael Roos, Kay-Eberhard Gottschalk, and Steffen Strehle. “Facile modification of freestanding silicon nitride microcantilever beams by dry film photoresist lithography”. In: *Journal of Micromechanics and Microengineering* 29.2 (2019), p. 025014 (cit. on p. 59).

[105] Jiyoung Chang, Qin Zhou, and Alex Zettl. “Facile electron-beam lithography technique for irregular and fragile substrates”. In: *Applied Physics Letters* 105.17 (2014) (cit. on p. 59).

[106] H Zhou, BK Chong, P Stopford, G Mills, A Midha, L Donaldson, and JMR Weaver. “Lithographically defined nano and micro sensors using “float coating” of resist and electron beam lithography”. In: *Journal of Vacuum Science & Technology B: Microelectronics and Nanometer Structures Processing, Measurement, and Phenomena* 18.6 (2000), pp. 3594–3599 (cit. on p. 59).

[107] Miriam Jaafar et al. “Customized MFM probes based on magnetic nanorods”. In: *Nanoscale* 12.18 (2020), pp. 10090–10097 (cit. on p. 59).

[108] Nadine Martine Leisgang. “Electrical control of excitons in a gated two-dimensional semiconductor”. PhD thesis. Philosophisch-Naturwissenschaftliche Fakultät der Universität Basel, 2022 (cit. on p. 59).

[109] Hongbing Cai, Kun Zhang, Xinxin Yu, Nan Pan, Yangchao Tian, Yi Luo, and Xiaoping Wang. “Highly efficient and controllable method to fabricate ultrafine metallic nanostructures”. In: *AIP Advances* 5.11 (2015) (cit. on pp. 61, 65).

[110] Moritz Haberthür. “Scanning Multi-Gate Microscopy”. Department of Physics, Poggio Lab. Master’s thesis. Basel, Switzerland: University of Basel, 2025 (cit. on p. 61).

[111] MT Björk, BJ Ohlsson, T Sass, AI Persson, Claes Thelander, MH Magnusson, Knut Deppert, LR Wallenberg, and Lars Samuelson. “One-dimensional heterostructures in semiconductor nanowhiskers”. In: *Applied Physics Letters* 80.6 (2002), pp. 1058–1060 (cit. on p. 67).

[112] Yann-Michel Niquet and Dulce Camacho Mojica. “Quantum dots and tunnel barriers in In As/ In P nanowire heterostructures: Electronic and optical properties”. In: *Physical Review B—Condensed Matter and Materials Physics* 77.11 (2008), p. 115316 (cit. on p. 67).

[113] Valentina Zannier, Francesca Rossi, Daniele Ercolani, and Lucia Sorba. “Growth dynamics of InAs/InP nanowire heterostructures by Au-assisted chemical beam epitaxy”. In: *Nanotechnology* 30.9 (2019), p. 094003 (cit. on p. 67).

[114] Mikael T Björk, Claes Thelander, Adam E Hansen, Linus E Jensen, Magnus W Larsson, L Reine Wallenberg, and Lars Samuelson. "Few-electron quantum dots in nanowires". In: *Nano Letters* 4.9 (2004), pp. 1621–1625 (cit. on p. 67).

[115] Lorenzo Romeo, Stefano Roddaro, Alessandro Pitanti, Daniele Ercolani, Lucia Sorba, and Fabio Beltram. "Electrostatic spin control in InAs/InP nanowire quantum dots". In: *Nano letters* 12.9 (2012), pp. 4490–4494 (cit. on p. 67).

[116] Samuele Cornia, Francesco Rossella, Valeria Demontis, Valentina Zannier, Fabio Beltram, Lucia Sorba, Marco Affronte, and Alberto Ghirri. "Microwave-assisted tunneling in hard-wall InAs/InP nanowire quantum dots". In: *Scientific Reports* 9.1 (2019), p. 19523 (cit. on p. 67).

[117] Francesco Rossella, Andrea Bertoni, Daniele Ercolani, Massimo Rontani, Lucia Sorba, Fabio Beltram, and Stefano Roddaro. "Nanoscale spin rectifiers controlled by the Stark effect". In: *Nature nanotechnology* 9.12 (2014), pp. 997–1001 (cit. on p. 67).

[118] Andreas Fuhrer, Linus E Fröberg, Jonas Nyvold Pedersen, Magnus W Larsson, Andreas Wacker, Mats-Erik Pistol, and Lars Samuelson. "Few electron double quantum dots in InAs/InP nanowire heterostructures". In: *Nano letters* 7.2 (2007), pp. 243–246 (cit. on p. 67).

[119] Peter Walke, Yasuhiko Fujita, Wannes Peeters, Shuichi Toyouchi, Wout Frederickx, Steven De Feyter, and Hiroshi Uji-i. "Silver nanowires for highly reproducible cantilever based AFM-TERS microscopy: towards a universal TERS probe". In: *Nanoscale* 10.16 (2018), pp. 7556–7565 (cit. on p. 67).

[120] Hui Xie, Juan Camilo Acosta, Dogan Sinan Haliyo, and Stéphane Régnier. "Pick-and-place nanomanipulation with three-dimensional manipulation force microscopy". In: *2009 IEEE/RSJ International Conference on Intelligent Robots and Systems*. IEEE. 2009, pp. 1333–1338 (cit. on p. 67).

[121] DB Suyatin, Claes Thelander, MT Björk, Ivan Maximov, and Lars Samuelson. "Sulfur passivation for ohmic contact formation to InAs nanowires". In: *Nanotechnology* 18.10 (2007), p. 105307 (cit. on p. 69).

[122] M Galván-Arellano, J Díaz-Reyes, and R Peña-Sierra. "Ohmic contacts with palladium diffusion barrier on III–V semiconductors". In: *Vacuum* 84.10 (2010), pp. 1195–1198 (cit. on p. 70).

[123] Ching-Ting Lee, Kou-Liang Jaw, and Chang-Da Tsai. "Thermal stability of Ti/Pt/Au ohmic contacts on InAs/graded InGaAs layers". In: *Solid-State Electronics* 42.5 (1998), pp. 871–875 (cit. on p. 70).

[124] Yiming Yang et al. “Hot carrier trapping induced negative photoconductance in InAs nanowires toward novel nonvolatile memory”. In: *Nano letters* 15.9 (2015), pp. 5875–5882 (cit. on p. 78).

[125] Joe Salfi, Nicola Paradiso, Stefano Roddaro, Stefan Heun, Selvakumar V Nair, Igor G Savelyev, Marina Blumin, Fabio Beltram, and Harry E Ruda. “Probing the gate- voltage-dependent surface potential of individual InAs nanowires using random telegraph signals”. In: *ACS nano* 5.3 (2011), pp. 2191–2199 (cit. on p. 78).

[126] Shadi A Dayeh, Cesare Soci, Paul KL Yu, Edward T Yu, and Deli Wang. “Influence of surface states on the extraction of transport parameters from InAs nanowire field effect transistors”. In: *Applied Physics Letters* 90.16 (2007) (cit. on p. 78).

[127] U Celano et al. “Harnessing charge injection in Kelvin probe force microscopy for the evaluation of oxides”. In: *Solid-State Electronics* 185 (2021), p. 108136 (cit. on p. 78).

[128] Elizabeth A Boer, Mark L Brongersma, Harry A Atwater, Richard C Flagan, and LD Bell. “Localized charge injection in SiO 2 films containing silicon nanocrystals”. In: *Applied Physics Letters* 79.6 (2001), pp. 791–793 (cit. on p. 78).

[129] A Pioda et al. “Spatially resolved manipulation of single electrons in quantum dots using a scanned probe”. In: *Physical review letters* 93.21 (2004), p. 216801 (cit. on p. 80).

[130] Erin E Boyd, Kristian Storm, Lars Samuelson, and Robert M Westervelt. “Scanning gate imaging of quantum dots in 1D ultra-thin InAs/InP nanowires”. In: *Nanotechnology* 22.18 (2011), p. 185201 (cit. on p. 80).

[131] Dingkun Ren, Zixuan Rong, Hyunseok Kim, Deniz Turan, and Diana L Huffaker. “High-efficiency ultrafast optical-to-electrical converters based on InAs nanowire-plasmonic arrays”. In: *Optics Letters* 44.19 (2019), pp. 4666–4669 (cit. on p. 86).

[132] Ziyuan Li, Jeffery Allen, Monica Allen, Hark Hoe Tan, Chennupati Jagadish, and Lan Fu. “Review on III-V semiconductor single nanowire-based room temperature infrared photodetectors”. In: *Materials* 13.6 (2020), p. 1400 (cit. on p. 86).

[133] Michele B Rota et al. “Bandgap energy of wurtzite InAs nanowires”. In: *Nano Letters* 16.8 (2016), pp. 5197–5203 (cit. on p. 86).

[134] Wilfred G Van der Wiel, Silvano De Franceschi, Jeroen M Elzerman, Toshimasa Fujisawa, Seigo Tarucha, and Leo P Kouwenhoven. "Electron transport through double quantum dots". In: *Reviews of modern physics* 75.1 (2002), p. 1 (cit. on p. 91).

[135] F Simmel, David Abusch-Magder, DA Wharam, MA Kastner, and JP Kotthaus. "Statistics of the Coulomb-blockade peak spacings of a silicon quantum dot". In: *Physical Review B* 59.16 (1999), R10441 (cit. on p. 91).

Appendix A

Fabrication Recipes

This appendix summarizes the fabrication recipes used for the preparation of substrates, nanowire devices, AFM levers, and SiN_x membrane-based structures. Each subsection lists the procedures step by step in a protocol-style format.

A.1 NW Devices

A.1.1 Substrate Preparation

Bonding Pad Fabrication

1. Spin coat S1805 resist at 4500 rpm for 40 s.
2. Bake at 125 °C for 2 min.
3. Define bonding pads by laser lithography (uPG 101, Heidelberg Instruments).
4. Develop in MF-319 developer (Microposit), rinse DI water, N_2 dry.
5. Plasma descum: ATTO Plasmacleaner (Diener), 20 s, O_2 8.3 sccm, 30 W.
6. Evaporate Ti/Au (5 nm/50 nm), MEB550S (Plassys Besteck).
7. Lift-off in ACE at 50 °C for 15 min, pipette agitation.
8. Rinse IPA 1 min, N_2 dry.

Cleaving

1. Spin coat PMMA (AR-P 672.045 950k).
2. Cleave wafer into 1 cm × 1 cm chips.

3. Clean: ACE 5 min, IPA 5 min.
4. N_2 dry.

Alignment Markers

1. Spin coat PMMA (AR-P 672.045 950k) at 4000 rpm, 40 s.
2. Bake at 150 °C, 2 min.
3. Disperse Au nanoparticles (100 nm OD 1, Sigma-Aldrich) on corners.
4. EBL: dose 225 µC/cm^2, 10 µm aperture.
5. Develop AR 600-55 1 min (RT), rinse IPA 1 min, N_2 dry.
6. Plasma descum: ATTO, 20 s, O_2 8.3 sccm, 30 W.
7. Evaporate Ti/Au (5 nm/25 nm), rotating stage, MEB550S.
8. Lift-off ACE @ 50 °C, ≥15 min, pipette agitation.
9. Rinse IPA 1 min, N_2 dry.

A.1.2 Bare InAs NW

- Material: Undoped InAs NW, diameter 75 nm, length 6 µm, grown by chemical beam epitaxy (Valentina Zannier & Lucia Sorba, NEST Pisa).

1. Pick up NW with glass needle and micromanipulator.
2. Disperse on prepared bonding pad sample in marker area.
3. Acquire SEM image (low kV, short exposure) for alignment.
4. Spin coat PMMA (AR-P 672.045 950k) @ 4000 rpm, 40 s; bake 150 °C/2 min.
5. EBL: dose 225 µC/cm^2, 10 µm aperture.
6. Develop AR 600-55 1 min (RT), rinse IPA 1 min, N_2 dry.
7. Plasma descum: ATTO, 20 s, O_2 8.3 sccm, 30 W.
8. In-situ Ar IBE: 35 s, 250 V/50 V, 8 mA, rotating stage.
9. Evaporate Ti/Au (5 nm/120 nm), rotating stage.
10. **Note (process used here):** Devices in this work employed Ti/Au (5/120 nm) contacts and were annealed per App. A.1.4. For future devices, use Ti/Pd/Au

(5/20/100 nm) after the same in-situ Ar IBE clean and use optimized annealing step A.1.5.

11. Lift-off: ACE @ 50 °C, 15 min, pipette agitation; rinse IPA 1 min; N_2 dry.
12. Mount on PCB with silver epoxy (EPO-TEK E4110).
13. Wire bond with Al-wire.
14. Store in vacuum.
15. Right before measuring do annealing.

A.1.3 InAs/InP NWQD

- Material: InAs/InP NW heterostructure (NW6801), grown by CBE (Valentina Zannier & Lucia Sorba, NEST Pisa).
- Diameter: 50±5 nm.
- Dot: InAs ∼19 nm between InP barriers ∼5 nm.
- QD located ∼450 nm from Au-seed end.

1. Process as Bare InAs NW.
2. Evaporate Ti/Au (5 nm/65 nm), rotating stage.
3. **Note (process used here):** Devices in this work employed Ti/Au (5/65 nm) contacts and were annealed per App. A.1.4. For future devices, use Ti/Pd/Au (5/20/50 nm) after the same in-situ Ar IBE clean and use optimized annealing step A.1.5.
4. Lift-off: ACE @ 50 °C, 15 min, pipette agitation; rinse IPA 1 min; N_2 dry.
5. Mount on PCB with silver epoxy (EPO-TEK E4110).
6. Wire bond with Al-wire.
7. Store in vacuum.
8. Right before measuring do annealing.

A.1.4 Contact Anneal (Legacy Vacuum / Ar Flush)

1. Load device lever into vacuum annealing chamber.
2. Purge with Ar and evacuate; repeat minimum three times.
3. Ramp to 200 °C

4. Dwell 10 min at 200 °C.
5. Cool to room temperature under vacuum without opening the chamber.

Note: This protocol can reduce contact resistance but may increase current noise after repeated cycles (risk of over-anneal).

A.1.5 Contact Anneal (Optimized Forming Gas)

1. Load device lever into annealing chamber.
2. Purge chamber with FG and set chamber pressure to 30 mbar.
3. Program temperature ramp ~ 10 °C/min to 190 °C.
4. Ramp to 190 °C under FG (30 mbar).
5. Dwell 20 min at 190 °C.
6. Cool down under FG with controlled ramp to room temperature.

Outcome: Preserves low contact resistance while avoiding noise increases observed after vacuum anneal.
Recovery use case: For devices stored in air (~ 1 week) with low conductance/no Coulomb peaks, this protocol restores Coulomb oscillations and stable transport.

A.2 SiN_x Membrane Devices

A.2.1 Membrane Fabrication

1. Substrate: Si wafer, double-side polished, dia. 50.8 mm, thickness 280 µm, orientation ⟨100⟩, undoped.
2. PECVD SiN_x: 300 nm backside, 50 nm frontside.
3. Lithography backside: S1805 @ 4500 rpm/45 s, bake 125 °C/2 min; expose (uPG 101); develop MF-319 1 min; rinse DI water; N_2 dry.
4. RIE backside SiN_x: $CHF_3/O_2 = 50/5$ sccm, 150 W, 16 min.
5. Resist removal: O_2 plasma 10 min, 20 sccm, 60 W.
6. KOH etch Si: 33% KOH @ 87 °C, $\sim$3 h.
7. Obtain suspended SiN_x membranes (50 nm thick, $\sim 50 \times 50$ µm^2).

A.2.2 Membrane Device Fabrication

1. Define markers and contacts by EBL, descum, and evaporate Ti/Au (5 nm/25 nm or 5 nm/65 nm) as described in A.1.1.
2. Place NWs using glass needle and SEM map for alignment.
3. Final metallization and lift-off as nanowire devices.

A.2.3 Triangular Membrane Release

1. Spin coat PMMA (AR-P 672.045 950k), 3 layers @ 4000 rpm, 40 s.
2. Bake 150 °C/2 min.
3. EBL exposure: dose 375 µC/cm^2, 10 µm aperture.
4. Develop AR 600-55 1 min (RT), rinse 1 min IPA, N_2 dry.
5. Etch SiN_x by RIE: CHF_3/O_2, 50/5 sccm, 150 W, 3 min.
6. Keep PMMA for easier transfer.

A.3 AFM Lever Fabrication

A.3.1 Cantilever Preparation

1. Start from ATEC cantilever.
2. Define plateau by FIB milling; adjust slope if needed.
3. Fix lever on Al plate with Kapton tape.
4. CO_2 snow cleaning: on hot plate 150 °C, N_2 flow.
5. ALD Al_2O_3 insulation: 66 nm, 600 cycles TMA/H_2O, 200 °C.
6. Mount in custom holder with Si masks (fabrication of Si masks in A.4).
7. Evaporate Ti/Au/Ti (5/120/5 nm).
8. Check leakage with probe station.

A.3.2 Multi-Gate Lever Fabrication

1. Start from prefabricated lever; clamp with metal rod (no Kapton). (Sec. 4.1)
2. Evaporate Au (20 nm) on front side using mask, MEB550S.

3. Prepare floating-PMMA transfer:
   (a) Spin coat dextran 15% @ 2000 rpm, 40 s, bake 150 °C/3 min.
   (b) Spin coat PMMA (AR-P 672.04 200k) @ 4000 rpm, 40 s, bake 150 °C/2 min.
   (c) Float film in DI water, transfer onto lever.
4. Bake lever 150 °C/2 min.
5. EBL exposure: dose as Sec. 4.3.3
6. Develop: ACE 3 min, rinse IPA 1 min, N_2 dry.
7. Ar IBE: 3 min, 500 V/100 V, 20 mA, Ar 8 sccm.
8. Remove PMMA: RIE O_2, 6 min, 20 sccm, 60 W.
9. Evaporate backside Au (20 nm), MEB550S.
10. Mount lever and wire bond.

A.3.3 NWQD Lever Fabrication

1. Start from prefabricated lever; clamp with metal rod (no Kapton).
2. Break triangular membranes from substrate using glass needle under optical microscope; pick up with glass needle.
3. Place triangle on tip plateau; align (asymmetric shape aids orientation).
4. Remove protective PMMA: RIE O_2 4 min, 20 sccm, 60 W.
5. SEM imaging for location of NWs
6. Prepare floating-PMMA transfer:
   (a) Spin coat dextran 15% at 2000 rpm, 40 s, bake 150 °C, 3 min.
   (b) Spin coat PMMA (AR-P 672.045 950k) at 4000 rpm, 40 s; bake 150 °C, 2 min.
   (c) Float film in DI water, transfer onto lever.
7. dry in vacuum $\geq$ 1 h; bake 150 °C/2 min.
8. EBL: open vias to membrane electrodes and define interconnects to lever pads. Dose 225 $\mu C/cm^2$.
9. Develop: AR 600-55 1 min (RT), rinse IPA 1 min, N_2 dry.
10. Descum: O_2 30 s, 20 sccm, 30 W.

11. Evaporate Ti/Au 5/75 nm (rotating stage).
12. Lift-off: ACE @ 50 °C (gentle pipette agitation), IPA rinse, N_2 dry.
13. Backside Au for reflectance: evaporate 20 nm Au on lever backside.
14. Mount lever and wire bond.
15. Annealing.

A.4 Silicon Hard Mask for Shadow Evaporation

Process executed by Fabio Bersano (EPFL).

1. Substrate: Si 100°, 100 mm diameter, 380 µm thick, single-side polished, p-type 0.1 Ω cm to 0.5 Ω cm, with 2 µm wet SiO_2 on top. Target features down to 50 µm.
2. Photoresist coat (front side): Coat AZ1512 (∼1.5 µm) on Si/SiO_2.
3. Front-side lithography (openings pattern):Expose with MLA (laser direct write) using GDS layout; develop.
4. Open oxide hard mask: Dry etch SiO_2 2 µm.
5. Deep Si etch (through-wafer): DRIE through Si to ∼300 µm depth (openings).
6. Polymer removal (post-DRIE): O_2 ashing, Tepla 5 min and solvent clean in ACE / Remover 1165.
7. Back-etch oxide (release mask edges): BHF (oxide bench) to remove 2 µm SiO_2.
8. Backside grinding to final thickness.
9. Dice into chips.
10. *Note:* Alternatively, design break-lines and release chips during grinding (include etched lines in layout).

Appendix B

Data Processing

B.1 Processing: Multi-Gate Lever on bare InAs NW

This script generates Figure 5.1. It ingests five Nanonis `.sxm` scans and performs presentation of data (zero-by-ROI).

B.1.1 Inputs

- Data folders: `.sxm` files

B.1.2 Zero-by-ROI

1. Define a rectangular ROI in physical units, ROI $= [x_0, x_1] \times [y_0, y_1]$ in μm (here $(0, 1) \times (6, 7)\,\mu$m).
2. For each gated image $I^{(k)}_{\mathrm{nA}}$, subtract the mean within the ROI:

$$I^{(k)}_{\mathrm{nA,zero}}(x, y) \;=\; I^{(k)}_{\mathrm{nA}}(x, y) \;-\; \langle I^{(k)}_{\mathrm{nA}} \rangle_{\mathrm{ROI}}\,.$$

3. Compute a global $[v^{\mathrm{zero}}_{\mathrm{min}}, v^{\mathrm{zero}}_{\mathrm{max}}]$ across $\{I^{(k)}_{\mathrm{nA,zero}}\}$ and render with a common scale.

B.1.3 Note

- Zero-by-ROI removes a constant offset local to a specified region.

B.2 Processing: Multi-Gate Lever above NWQD

This script generates Figure 5.2.

This script ingests a batch of Nanonis `.sxm` scans taken with different gates and tip–sample heights, extracts the raw DC current channel and applies a simple offset. The color scale is globally normalized across all panels to facilitate visual comparison.

B.2.1 Inputs

- Data folders: `.sxm` files listed in a dictionary, each tagged by `gate` $\in$ {Z,V,W,X,a,no} and `height_nm` $\in \{0, 50, 100, 150, 160\}$ nm.

B.2.2 Preprocessing

For each file:

1. Load pixels I_{raw} from the DC channel.
2. Offset and unit conversion:

$$I_{\mathrm{pA}}(x, y) \;=\; \Big(I_{\mathrm{raw}}(x, y) - \min_{x,y} I_{\mathrm{raw}}\Big) \times 10^{12}$$

   i.e. the current map is zero-referenced to the image minimum and expressed in pA. This yields a relative current contrast per panel.

B.2.3 Global Normalization

Let $\mathcal{D} = \{I_{\mathrm{pA}}^{(k)}\}$ be the set of all panels. A single global range is used and all images are displayed with a common linear normalization $[v_{\min}, v_{\max}]$.

B.2.4 Note

- The offset-to-minimum step produces relative current maps (minimum set to 0 pA) to emphasize spatial contrast; absolute offsets are not shown.
- Only the pA conversion and global clipping are used.

B.3 Background Detrending for Topography Scans

This routine loads Nanonis `.sxm` images, removes large-scale background by planar detrending, rescales to physical units.

B.3.1 Inputs

- Data: `.sxm` files

B.3.2 Planar Detrending

Given a height map $Z(x, y)$ sampled on a regular grid over a field of view $X_{\mu\mathrm{m}} \times Y_{\mu\mathrm{m}}$, we fit and remove a best-fit plane

$$Z_{\mathrm{fit}}(x, y) \;=\; a\,x + b\,y + c,$$

by solving the least-squares problem:

$$\min_{a,b,c} \left\| \mathbf{G}\,[a\ b\ c]^{\top} - \mathbf{z} \right\|_2^2, \quad \mathbf{G} = \begin{bmatrix} x_1 & y_1 & 1 \\ \vdots & \vdots & \vdots \\ x_N & y_N & 1 \end{bmatrix}, \quad \mathbf{z} = \begin{bmatrix} Z_1 \\ \vdots \\ Z_N \end{bmatrix},$$

The detrended image is

$$Z_{\mathrm{detrend}}(x, y) \;=\; Z(x, y) - Z_{\mathrm{fit}}(x, y).$$

B.3.3 Scaling and Display transformation

1. Detrend: Z_{detrend} = result of the plane removal above.
2. Z height rescale $Z_{\mathrm{scaled}} = Z_{\mathrm{detrend}} \times 2.73$ from z piezo calibration.
3. Zero-shift for plotting: $Z_{\mathrm{disp}} = Z_{\mathrm{scaled}} - \min(Z_{\mathrm{scaled}})$ so the displayed map is ≥ 0.

B.3.4 Note

- Detrending removes tilts and scanner bow to first order; higher-order artifacts (e.g. creep) are not modeled.

B.4 Conversion of Current Maps to Equivalent Plunger-Gate Voltage

This procedure converts measured NWQD lever current (from scanning images) into an equivalent plunger-gate voltage shift ΔV_g^{eq} using a calibrated Coulomb-peak model. The conversion is performed pixel-wise on AFM/Nanonis images and produces maps of $\Delta V_g^{eq}(x, y)$.

B.4.1 Inputs

- Data: `.sxm` files and `.cvs` of reference Coulomb peak.

B.4.2 Model Calibration from a Coulomb Peak

1. Load the calibration Coulomb peak. Extract the plunger gate voltage V and the corresponding current I.
2. Select a fitting window. Restrict to a gate interval that spans one thermal Coulomb peak: here $V \in (5.10,\, 5.23)\,\mathrm{V}$.
3. Fit "thermal + linear background" model. The model is

$$I(V) \;=\; \frac{A}{\cosh^2\!\Big(\dfrac{V - V_0}{2k_B T_e}\Big)} \;+\; mV + b,$$

   with k_B in eV/K. Nonlinear least-squares returns the parameters A, V_0, T_e, m, b.

B.4.3 Numerical Inversion: Current → equivalent Gate Voltage

1. Define the inverse on the left flank. For a target current I_*, solve for $V < V_0$ the root of

$$f(V) \equiv \frac{A}{\cosh^2\!\Big(\dfrac{V - V_0}{2k_B T_e}\Big)} + mV + b - I_* \;=\; 0,$$

   using a robust bracketing method (Brent) on the interval $[V_0 - 0.1,\, V_0]$.
2. The solution is denoted $V_g^{eq}(I)$ and represents the plunger voltage that would produce the measured current on the calibrated left flank.

B.4.4 Per-image Conversion and Background Removal

1. Load image data. For each scan height (e.g., `-440\,nm`, `-415\,nm`, ...), load:
   - a gate-excited current image (`single` or `double` gate set), and
   - the corresponding background image (no gate excitation)

   from Nanonis `.sxm` files.

2. Pixel-wise conversion (current $\to V_g^{eq}$). Apply the calibrated inverse map to each pixel of the gate-excited image:

$$I(x,y) \;\longmapsto\; V_g^{eq}(x,y) \quad \text{using} \quad A, V_0, T_e, m, b.$$

   Apply the same conversion to the paired background image to obtain $V_{g,\mathrm{bg}}^{eq}(x,y)$.

3. Background subtraction. Form the differential map

$$\Delta V_g^{eq}(x,y) \;=\; V_g^{eq}(x,y) \;-\; V_{g,\mathrm{bg}}^{eq}(x,y),$$

   which removes slow drifts/offsets not due to the local gate coupling.

4. Zero reference (ROI). Choose a reference region of interest (ROI) in real space (here $x \in [0, 0.5]\,\mu$m, $y \in [2.75, 3.25]\,\mu$m). Subtract its mean value to define the zero of ΔV_g^{eq}:

$$\Delta V_{g,\mathrm{zeroed}}^{eq}(x,y) \;=\; \Delta V_g^{eq}(x,y) \;-\; \left\langle \Delta V_g^{eq} \right\rangle_{\mathrm{ROI}}.$$

B.4.5 Note

- The inverse map is restricted to the calibrated *left* flank of the single Coulomb peak.
- Validity requires pixel currents to lie within the model's range $\Big(mV + b,\; A + mV_0 + b\Big)$.

B.5 Coulomb–Diamond Picker

This workflow interactively picks one Coulomb diamond, extracts robust slopes and center, builds a small-bias linecut, and computes the per-diamond parameters used throughout the thesis.

B.5.1 Inputs

- One 2D current map $I(V_{\mathrm{SD}}, V_g)$ from a `.csv`.

B.5.2 Interactive Picking

1. Display $I(V_{\mathrm{SD}}, V_g)$ and $|\partial I/\partial V_{\mathrm{SD}}|$ side-by-side.
2. The user clicks two "+" edges and two "−" edges (each as 2 points) and one center point.
3. For each pair, fit a line $V_{\mathrm{SD}} = s\,V_g + b$. Keep median slopes $\tilde{s}_+ > 0$ and $\tilde{s}_- < 0$ and median intercepts $\tilde{b}_\pm$.
4. Gate-intercepts ($V_{\mathrm{SD}} = 0$) give ΔV_g between the two edges; the center provides V_g^*, V_{SD}^*.

B.5.3 Derived Quantities

1. Lever arm from diamond slopes:

$$\alpha_0 \;=\; \frac{1}{1 + 1/\tilde{s}_+ + 1/|\tilde{s}_-|}\,.$$

2. Capacitances:

$$C_g = \frac{e}{\Delta V_g}, \quad C_s = \frac{C_g}{\tilde{s}_+}, \quad C_d = \frac{C_g}{|\tilde{s}_-|}, \quad C_\Sigma = C_g + C_s + C_d.$$

B.5.4 Small-bias Linecut and Temperature

1. Build a near-zero-bias linecut $I(V_g)$ by selecting a small finite V_{SD} column.
2. Determine the peak FWHM of $I(V_g)$ (robust, baseline-aware). Convert to temperature via the thermal-broadened relation

$$T_e \;\approx\; \frac{e\,\alpha_0}{3.52\,k_B}\,\mathrm{FWHM}.$$

B.5.5 Local Conductance Fit and Response

1. From $I(V_g)$ and finite $V_{\mathrm{SD,eff}}$, compute $G(V_g) = I/V_{\mathrm{SD,eff}}$.
2. Fit a sech^2 peak plus offset around the maximum:

$$G(V_g) \;\approx\; G_0\,\mathrm{sech}^2\!\left(\tfrac{e\alpha_0(V_g-V_0)}{2k_BT_e}\right) + G_{\mathrm{bg}}.$$

3. Charge response (per gate-voltage fluctuation) on the flank:

$$R_{q0}(V_g) \;=\; \frac{G_0}{C_\Sigma}\,\frac{e\,V_{\mathrm{SD,eff}}}{k_BT_e}\,\frac{\sinh u}{\cosh^3 u}, \quad u = \frac{e\alpha_0(V_g-V_0)}{2k_BT_e}.$$

B.5.6 Outputs

- Per-diamond metrics $\{\tilde{s}_\pm, \alpha_0, T_e, C_g, C_s, C_d, C_\Sigma, V_{\mathrm{SD,eff}}\}$.

B.6 Noise Extractions

B.6.1 Noise-equivalent Charge from Transport White Noise

This step uses the per-diamond response R_{q0} and the $I(V_g)$ linecut to compute white (frequency-independent) ΔQ from thermal and shot noise.

Inputs

- Per-diamond metrics from B.5 (α_0, T_e, C_Σ, $V_{\mathrm{SD,eff}}$), and the $I(V_g)$ linecut.

White noise terms

1. Thermal (Johnson) current ASD:

$$S_I^{\mathrm{th}}(V_g) = \sqrt{4k_BT_e\,G(V_g)}.$$

2. Shot current ASD (Fano $F \in [1]$):

$$S_I^{\mathrm{shot}}(V_g) = \sqrt{2e\,|I(V_g)|\,F}.$$

3. White floor (quadrature sum), and charge ASD:

$$S_I^{\mathrm{white}} = \sqrt{\left(S_I^{\mathrm{th}}\right)^2 + \left(S_I^{\mathrm{shot}}\right)^2}, \qquad \delta Q_{Noise}^{white}(V_G) = \frac{S_I^{\mathrm{white}}(V_g)}{e\,|R_{q0}(V_g)|}.$$

4. Report the setpoint value.

Note

- This pass intentionally excludes $1/f$ noise; it is treated separately in §B.6.2.

B.6.2 ROI-based $1/f$ Current-Noise

This routine estimates the low-frequency current noise from background `.sxm` scans by converting a fixed real-space ROI to a current–time trace in acquisition order and fitting the PSD.

Inputs

- `.sxm` background, no gate excitation.
- ROI in μm: $[x_0, x_1] \times [y_0, y_1]$.
- Pixel dwell time T_{dwell} (or line time + pixels/line).

Method

1. Load raw channel, map ROI $\rightarrow$ pixel indices; traverse lines in acquisition direction to build $I(t)$.
2. Detrend $I(t)$ and compute PSD via Welch; correct for boxcar averaging using

$$|H(f)|^2 = \mathrm{sinc}^2(\pi f T_{\mathrm{dwell}}),$$

   i.e. $S_I^{\mathrm{true}} = S_I^{\mathrm{meas}}/|H|^2$ away from zeros.
3. Exclude bands around $\{n/T_{\mathrm{dwell}}\}$ and known scan rates; fit

$$S_I(f) = \frac{A_I^2}{f} + S_0 \qquad (f_{\min} \le f \le f_{\max}).$$

Outputs

- A_I [A/$\sqrt{\mathrm{Hz}}$ @ 1 Hz] and S_0 [A^2/Hz], the detrended $I(t)$, and PSD figures.

Note

- The sinc correction is essential to remove the low-pass of pixel integration.

B.6.3 Combining Calibrated Response with ROI Noise

This step converts the ROI current-noise model to charge noise using the Coulomb-peak response and reports NEQ at selected frequencies.

Inputs

- R_{q0} at a chosen setpoint from the Coulomb peak (§B.5).
- ROI noise fit parameters A_I, S_0 (§B.6.2).

Conversion and reporting

1. Current ASD at frequency f:

$$S_I(f) = \sqrt{A_I^2/f + S_0}.$$

2. $\delta Q_{1/f}(f, V_G)$ (measured total):

$$\delta Q_{1/f}(f, V_G) = \frac{S_I(f)}{e\,|R_{q0}|}.$$

3. Transport δQ_{Noise}^{white} from §B.6.1 can be combined in quadrature with the pure $1/f$ term:

$$\delta Q_{tot}(V_G) = \sqrt{\delta Q_{Noise}^{white\,2} + \left(A_I/(e|R_{q0}|\sqrt{f})\right)^2}.$$

Appendix C

Scientific Output

In the following all the scientific output is presented, which was produced within the time frame of this thesis.

C.1 Published Papers

1. L. Forrer, A. Kamber, A. Knoll, M. Poggio, F.R. Braakman, "Electron-beam lithography of nanostructures at the tips of scanning probe cantilevers". In: *AIP Advances* (2023), 13, 035208. `https://doi.org/10.1063/5.0127665`

C.2 Conference Presentations

1. L. Forrer, A. Kamber, M. Poggio, F.R. Braakman, "Scanning Nanowire Quantum Dot". In: *Annual FIBsuperProbes meeting* (2022), Tübingen (Germany)
2. L. Forrer, A. Kamber, M. Poggio, F.R. Braakman, "Scanning Nanowire Quantum Dot". In: *NCCR SPIN Annual meeting* (2021), Pontresina (Switzerland)
3. L. Forrer, A. Kamber, M. Poggio, F.R. Braakman, "Scanning Nanowire Quantum Dot". In: *INASCON 2023* (2023), Basel (Switzerland)
4. L. Forrer, A. Kamber, M. Poggio, F.R. Braakman, "Scanning Nanowire Quantum Dot". In: *SNI Annual Event* (2023), Meisterschwanden (Switzerland)
5. L. Forrer, A. Kamber, M. Poggio, F.R. Braakman, "Scanning multi-gate and Quantum Dot Microscopy". In: *NCCR SPIN Annual meeting* (2024), Pontresina (Switzerland)

C.3 Presented Posters

1. L. Forrer, A. Kamber, M. Poggio, F.R. Braakman, "Scanning Nanowire Quantum Dot". In: *NCCR SPIN Site Visit* (2021), Basel (Switzerland)
2. L. Forrer, A. Kamber, M. Poggio, F.R. Braakman, "Scanning Nanowire Quantum Dot". In: *SNI Annual Event* (2021), Lenzerheide (Switzerland)
3. L. Forrer, A. Kamber, M. Poggio, F.R. Braakman, "Scanning Nanowire Quantum Dot". In: *SNI Winterschool* (2022), Zermatt (Switzerland)
4. L. Forrer, A. Kamber, M. Poggio, F.R. Braakman, "Scanning Nanowire Quantum Dot". In: *SNI Annual Event* (2022), Lenzerheide (Switzerland)
5. L. Forrer, A. Kamber, M. Poggio, F.R. Braakman, "Scanning Nanowire Quantum Dot". In: *SNI Winterschool* (2023), Unterwasser (Switzerland)
6. L. Forrer, A. Kamber, M. Poggio, F.R. Braakman, "Scanning multi-gate and Quantum Dot Microscopy". In: *SNI Winterschool* (2024), Crans Montana (Switzerland)

7. L. Forrer, A. Kamber, M. Poggio, F.R. Braakman, "Scanning multi-gate and Quantum Dot Microscopy". In: *SNI Annual Event* (2024), Meisterschwanden (Switzerland)
8. L. Forrer, A. Kamber, M. Poggio, F.R. Braakman, "Scanning multi-gate and Quantum Dot Microscopy". In: *SNI Winterschool* (2025), Adelboden (Switzerland)
9. L. Forrer, A. Kamber, M. Poggio, F.R. Braakman, "Scanning multi-gate and Quantum Dot Microscopy". In: *SNI Annual Event* (2025), Meisterschwanden (Switzerland)
10. L. Forrer, A. Kamber, M. Poggio, F.R. Braakman, "Scanning Nanowire Quantum Dot". In: *INASCON 2025* (2025), Prag (Czech Republic)

Acknowledgments

I am deeply grateful to Prof. Martino Poggio for giving me the opportunity to pursue my PhD in the Poggio Lab, for his guidance in pushing this project forward, and for creating an excellent work environment. I also thank Dr. Floris Braakman for supervising the project and for many insightful discussions. I am grateful to Prof. Dominik Zumbühl for serving as my second supervisor and to Prof. Peter H. Grütter for completing my doctoral committee as an external expert.

My sincere thanks go to the entire Poggio Lab team for their help and support throughout this period. In particular, I thank Aurèle, a fellow PhD student on the project, for his tremendous contributions in bringing the experiment to its current state but also for the out-of-work activities as ping-pong and billiard matches. I also thank Moritz, a Master's student who developed the automated SEM process we rely on, which has saved us from countless user-made errors, Marcus for his help with the FIB and for the consistently positive atmosphere in the nano-imaging lab, Mathias for showing us the fabrication of membranes, Boris for helping me with COMSOL, Francesco for tracking down noise sources, and Taras for helping resolve ground loops and optimize the setup noise.

I would also like to acknowledge the contributions of the former members of the Poggio Lab, namely Estefani, Kousik, David, Hinrich, Giulio, Simon, Thibaud as well as the current team: Parithosh, Damien, Liza, Andriani, Lorena, Rounak, Lukas, Daniel, Aris, Antonella, Patrick, Loris, Katharina, and Mirco.

Many thanks to Fabio Bersano for fabricating the silicon masks used in this work and I gratefully acknowledge the group of Lucia Sorba for growing the InAs nanowires that form the basis of our experiments.

I am indebted to the infrastructure teams whose expertise made this work possible: the mechanical workshop for machining the probe components and producing countless custom parts for our setup and fabrication process, the electronics workshop for PCB design, soldering, and ground-decoupler support, the Nanofabrication Team for maintaining the cleanroom facilities, and Claudia Wirth for her administrative

support. I also thank the entire SNI team for their assistance and the canton Aargau for financing my PhD position.

Throughout this journey, I have been fortunate to meet many wonderful people, to whom I am very grateful. Outside the university, I thank my icehockey teams Bebbi Yysbääre and the Hawaiians for helping me relieve stress and offering a different perspective on things. I am thankful to all my friends in Basel and back home for their steady support over the past years, and to the cycling sessions that helped me regain focus and perspective during stressful times.

Finally, I owe my deepest gratitude to my parents and my brother for their unwavering encouragement, going with me through the ups and downs, and their love. And to Rahel, thank you for your love, patience, and constant support.

I would like to acknowledge the use of OpenAI's ChatGPT as an assistant during the preparation of this thesis. Specifically, I utilized ChatGPT to review and help refine the text to enhance readability and clarity. Additionally, ChatGPT was used to assist with coding tasks in Python. I also used Consensus AI for conducting literature research. All intellectual content, analysis, and conclusions remain my own.

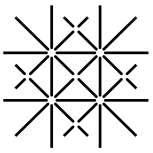

Universität
Basel

Präsentiert von:

Luca Forrer